U.S. DEPARTMENT OF THE INTERIOR

GEOLOGICAL SURVEY

Integrated model of the shallow and deep hydrothermal systems in the East Mesa area, Imperial Valley, California

By T. D. Riney, J. W. Pritchett, and L. F. Rice

Systems, Science and Software (now S CUBED)
P.O. Box 1620, La Jolla, California 92038

Open-File Report 82-980

This report was prepared under Contract No. 14-08-0001-16321 from the U.S. Geological Survey's Geothermal Research Program and has not been reviewed for conformity with USGS editorial standards. Opinions and conclusions expressed herein do not necessarily represent those of the USGS.

1982

x x x x x x x x x x x x x x x x x x x x x x x x x x x x x x x x x x x x x x x x x x x x x x x x x x x x x x

Projection Information

This report presents the results of U.S. Geological Survey Geothermal Research Program Contract No. 14-08-0001-16321 with Systems, Science and Software. Principal Investigator was Dr. T. David Riney, and the period of the study was from September 1, 1978, to February 29, 1980. Its objective was to develop a conceptual and computer model of the hydrothermal system at East Mesa, California.

TABLE OF CONTENTS

ABSTRACT

Geological, geophysical, thermal, petrophysical and hydrological data available for the East Mesa hydrothermal system that are pertinent to the construction of a computer model of the natural flow of heat and fluid mass within the system are assembled and correlated. A conceptual model of the full system is developed and a subregion selected for quantitative modeling. By invoking the Boussinesq approximation, valid for describing the natural flow of heat and mass in a liquid hydrothermal system, it is found practical to carry computer simulations far enough in time to ensure that steady-state conditions are obtained. Initial calculations for an axisymmetric model approximating the system demonstrate that the vertical formation permeability of the deep East Mesa system must be very low (k_v ~ 0.25 to 0.5 md). Since subsurface temperature and surface heat flow data exhibit major deviations from the axisymmetric approximation, exploratory three-dimensional calculations are performed to assess the effects of various mechanisms which might operate to produce such observed asymmetries. A three-dimensional model evolves from this iterative data synthesis and computer analysis which includes a hot fluid convective source distributed along a leaky fault radiating northward from the center of the hot spot and realistic variations in the reservoir formation properties.

I. INTRODUCTION

The Imperial Valley occupies a broad lowland in the southern part of the Salton Trough which is a landward extension of the depression filled by the Gulf of California (Figure 1). Much of the land surface is below sea level, and the shallow groundwater flow in the valley flows generally northwestward towards the Salton Sea, which lies over 200 feet below sea level [Loeltz, et al. (1975)]. The Imperial Valley is bordered by the Chocolate Mountains on the northeast, the Peninsular Range of Baja California and southern California on the southwest, and the Salton Sea on the northwest; it is contiguous with the Mexicali Valley in Mexico on the southeast.

The Salton Trough is a structural as well as topographic depression in which the surface of the basement-complex lies thousands of feet below the basement-complex surface in the bordering mountains. The basement-complex of the trough is overlain by a thick sequence of marine and (predominantly) nonmarine sedimentary rock. In this study we will be concerned principally with the heterogeneous sequence of nonmarine interbedded sandstone/shale deposits in the upper ten thousand feet of the sequence. The Colorado River drainage basin has been the predominant source of these sediments.

Half a million acres within the Imperial Valley have been transformed into one of the Nation's most productive agriculture areas by the importation of Colorado River water for irrigation. In 1950, the U. S. Geological Survey undertook a comprehensive study of the water resources of the upper Colorado River region, and in 1960, of the lower Colorado River region. As part of this latter study, Loeltz, et al. [1975] presented the results of a reconnaissance of the geology, hydrology, and chemical quality of the groundwater in

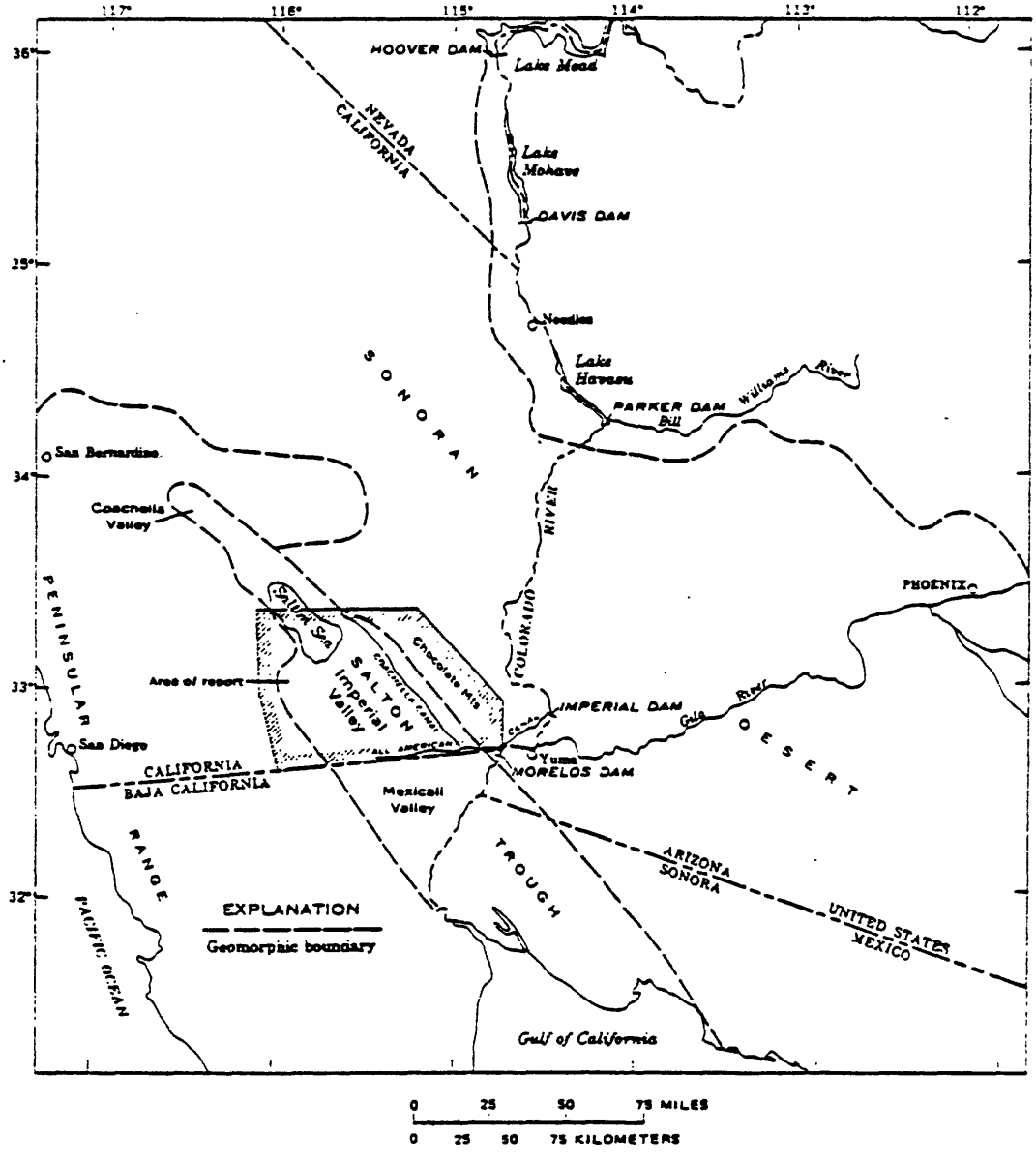

Figure 1. Area of geohydrologic study by Loeltz, et al. [1975].

the upper thousand feet of the Imperial Valley. Recharge to the groundwater reservoir from precipitation and discharge from wells within the region are both negligible compared to the recharge to the aquifer from the unlined irrigation canals that traverse the area. At depths greater than about a thousand feet, the groundwater is generally too saline for irrigation and most other uses, and the hydraulic connection between the water in the deeper deposits and the water in the upper part of the groundwater reservoir is poor.

Recently, the Imperial Valley has also become a major focal point for geothermal development in the U. S. The hot geothermal fluids usable for generation of electrical power lie within the deeper deposits. The Imperial Valley contains six Known Geothermal Resource Areas (KGRA's) comprising about a quarter million acres. These areas, depicted in Figure 2, were delineated by the U. S. Geological Survey in the Federal Register in 1971. Hardt and French [1976] have systematically collected, collated and published pertinent data from water wells, geothermal wells, and oil test wells, including water-quality records, isotope analyses, pressure and temperature information and driller's logs. This information extends the hydrology phase of the report by Loeltz, et al. to the deeper reservoirs of geothermal energy. The U. S. Geological Survey (Miller [1977]) subsequently used the collected information and other data as a basis to develop a computer model simulating the steady-state transport of fluid mass and heat in a shallow confined aquifer within the East Mesa area shown in Figure 3. The vertical section in Figure 4 shows Miller's conceptual model of the shallow hydrothermal system studied. Vertical mass leakage and heat conduction from above, across the confining zone, were included in the model. Heat conduction from below, across the geothermal reservoir cap, was included but mass leakage from below was assumed to be zero. Miller [1977] points out, however, that the assumption of complete hydrologic isolation between the shallow aquifer and the deeper geothermal reservoir should be relaxed in any modeling effort

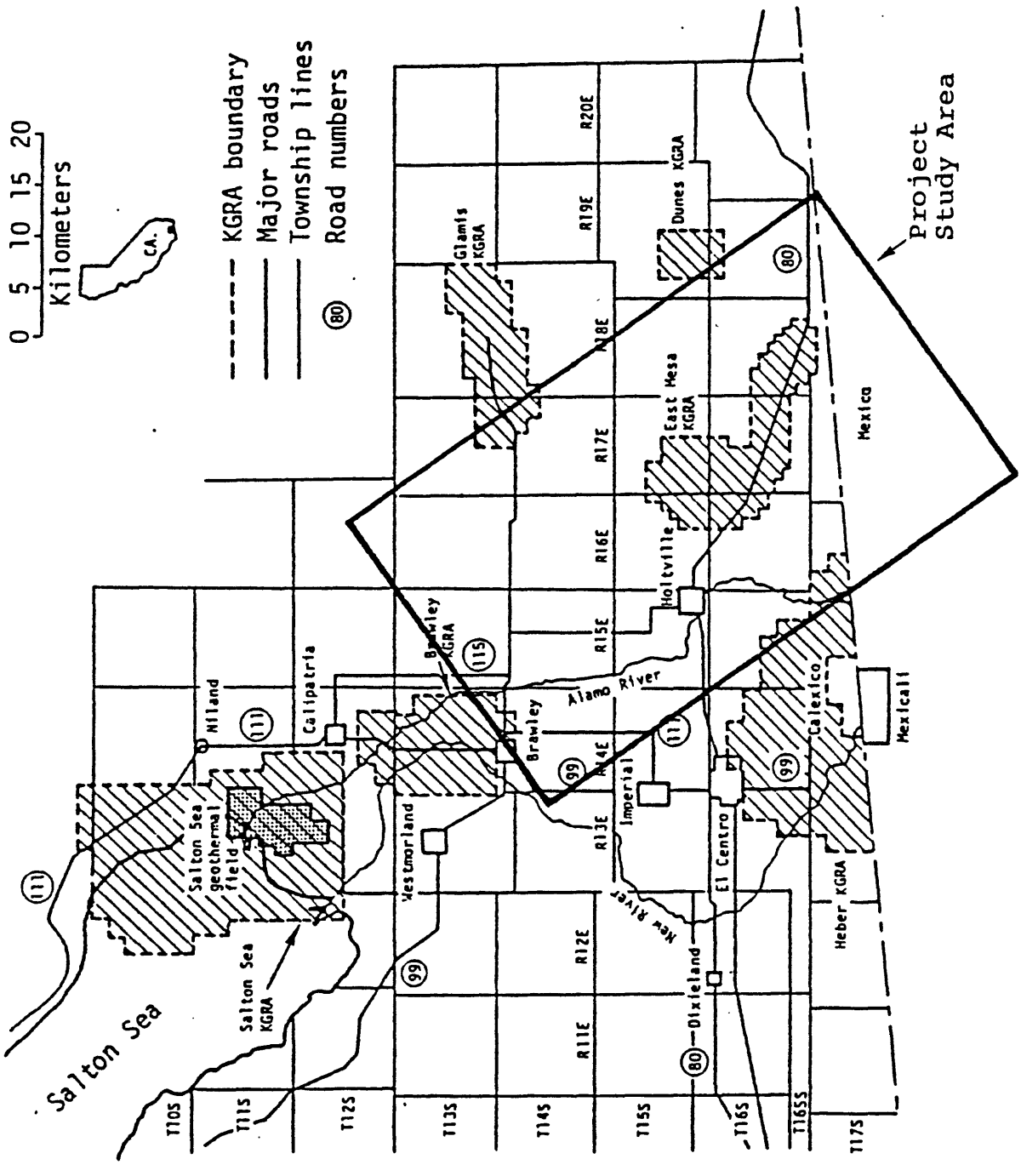

Figure 2. Map of the Imperial Valley showing the KGRA's and the area studied in this project.

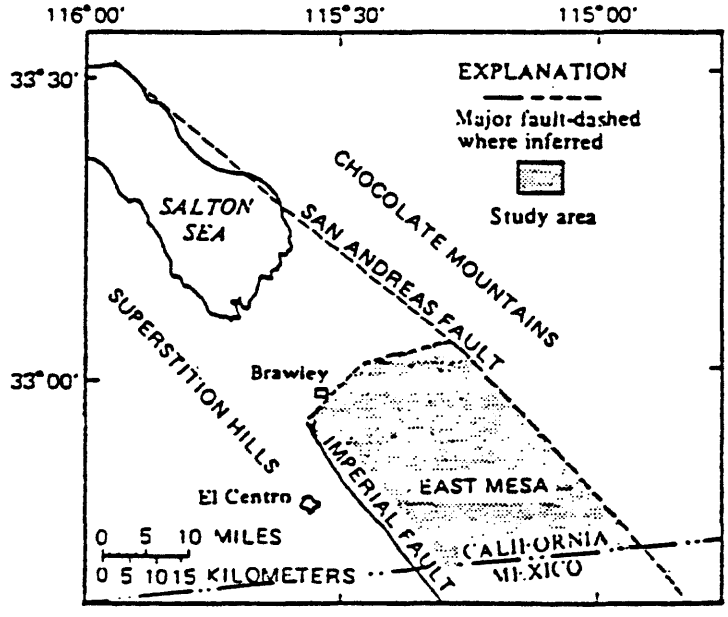

Figure 3. Imperial Valley, California, showing location of major faults and area studied by Miller. (From Miller [1977, Figure 1]).

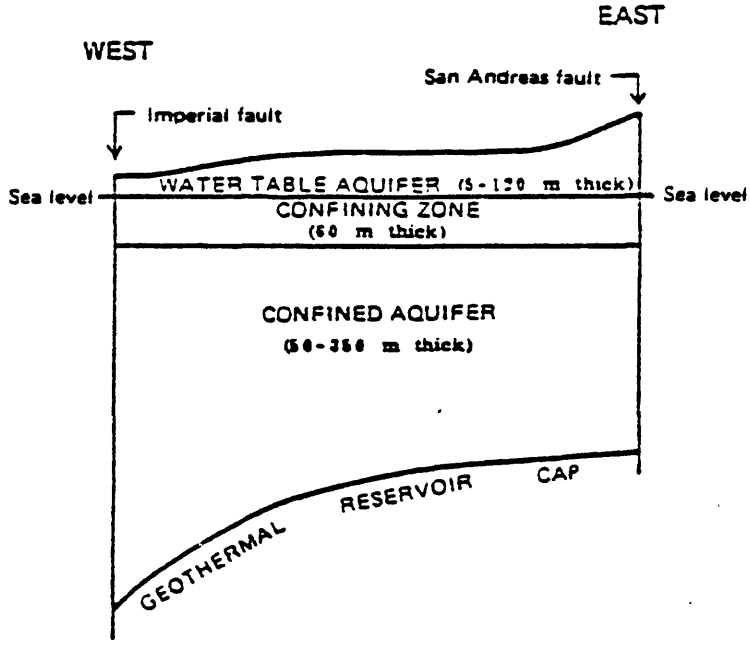

Figure 4. Conceptual model of shallow hydrothermal system, southeastern Imperial Valley. (From Miller [1977, Figure 5]).

which attempts to predict the transient esponse of the reservoir system to development of the geothermal re urce.

On September 1, 1978 the present r earch project to develop an integrated computer model of the sha ow and deep hydrothermal system in the East Mesa area was initi ed by S^3 under the U.S. Geological Survey's Geothermal Research P gram. The specific long range objectives are to develop a model o the natural flow of fluid and heat in the integrated systems and to pply the model to assess changes in the shallower system that wou result from large scale movement of fluid mass and heat transpor in the deeper geothermal system. Like the majority of geotherm fields, the East Mesa geothermal system contains liquid brine th geologic faults that serve as channels for heated fluid t rise from depth. The objectives of this project have, ther ore, been broadened to include exploratory calculations that al the modeling results to be more generally applicable to fault trolled liquid-dominated geothermal systems other than the East Mes system.

Unlike petroleum reservoirs (and geopressured geothermal reservoirs), virgin hydrothermal fields re not static. Natural convective and conductive heat transfer, companied by substantial fluid flow, takes place continuously in t se systems. Accordingly, if we wish to assess changes in the shall er East Mesa hydrothermal system that will result from large scale vement of fluid mass and heat in the deeper geothermal system, we ust first find a set of initial conditions that are consist t with a steady or pseudo-steady solution of the governing equations which describe mass, momentum and energy conservation, a are also consistent with measured data. Such a natural flow solu on may be obtained by an iterative "history-matching" process. Indeed, such numerical experiments may be expected to provide v uable insights into such

questions as the distribution of hot fluid sources, cold water recharge, formation porosity and permeability of the system.

The present research project has followed such an approach. A computer based simulator of the fluid mass and heat flow processes operative in a single-phase hydrothermal system is used as a tool for synthesizing the available geological, geophysical, thermal, petrophysical and hydrologic data sets for the East Mesa shallow and deep subsystems into an integrated geohydrological model.

II. CONCEPTUAL MODEL

Figure 5 presents a schematic of our conceptual model of the hydrological characteristics of the integrated East Mesa hydrothermal system. It is an attempt to relate the basic elements listed by Dutcher, et al. [1972] to the information available for this system and is similar to schematics presented by White [1968]. It constitutes the framework within which the data synthesis and computer modeling of the system have been conducted. Seepage from the Colorado River and the unlined irrigation canal system is the principal source of recharge water. Part of this recharge, (A) , will flow into the shallow confined zone studied by Miller [1977]; part will flow down permeable faults, (B) , since the recharge water is cooler (and denser) than the deeper fluid. The upper mantle within this crustal spreading region is believed to be about 700°C (Elders, et al. [1972]). The downward flowing water will be heated within some "heating volume" as it approaches the mantle surface. Some of the heated fluid mass will then convect upward along permeable faults, (C) . Most of this upwelling fluid will likely either leak off laterally into the geothermal reservoir or be forced laterally by the relatively impermeable geothermal reservoir cap, (D) , but some will leak across the cap into the shallow confined aquifer, (E) . Part of the fluid leaving the heating volume will also be pushed laterally, (F) .

The parameters required to develop a computer simulation of the full hydrothermal system would include the three-dimensional distributions of temperature, water quality, rock thermal conductivity, porosity, permeability, etc. throughout the system. Knowledge of the natural flux of fluid mass and heat would also be required. Although East Mesa is one of the most extensively explored hydrothermal systems in the United States, sufficient data will probably never be available to model the complete system

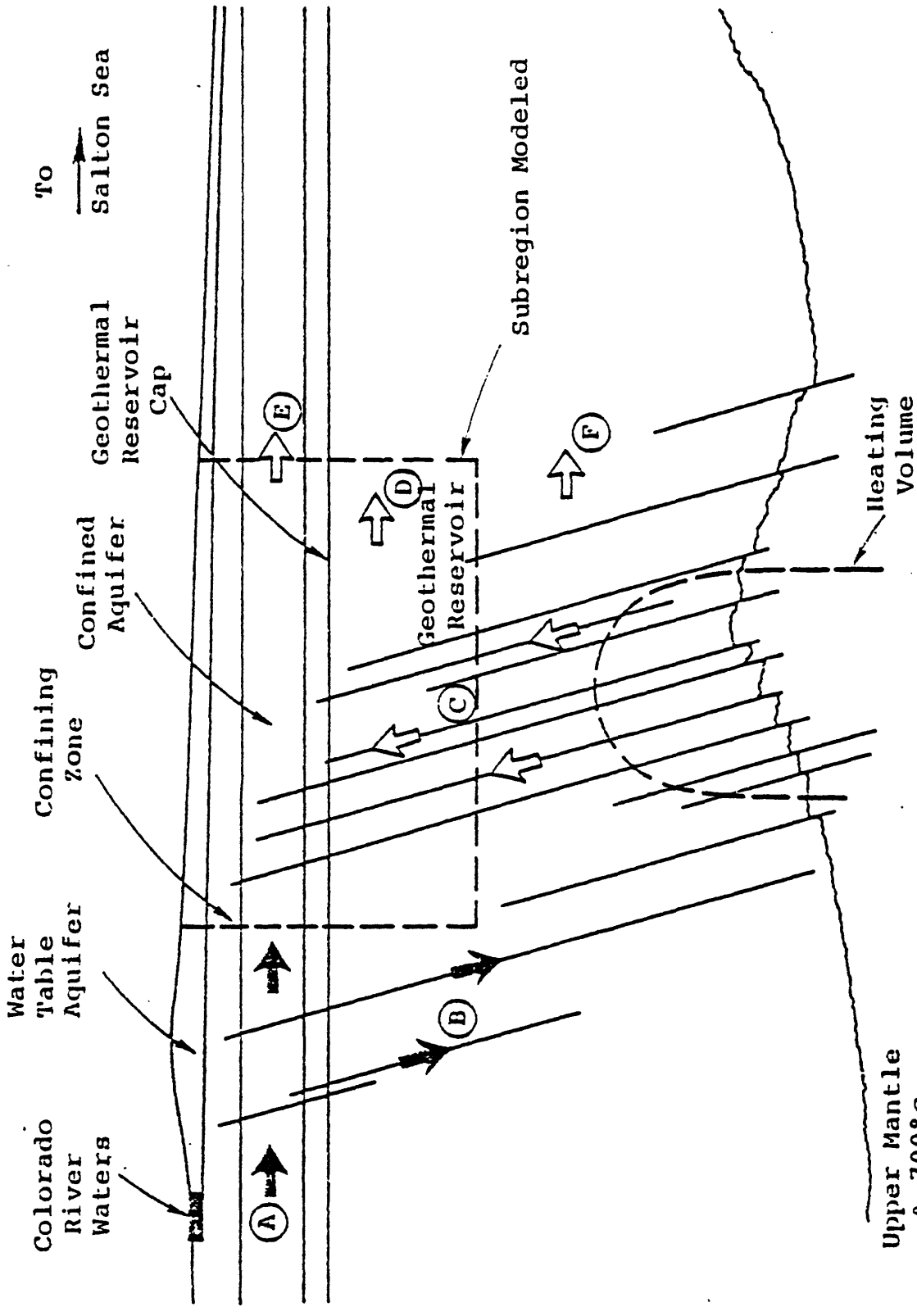

Figure 5. Schematic of preliminary conceptual model of full East Mesa hydrothermal system and the subregion modeled in this project.

represented schematically in Figure 5. In this project our effort to model the shallow and deep systems is restricted to a subregion as depicted in the schematic. The subregion is centered on the geothermal anomaly, covers the surface area shown in Figure 2, and extends to a depth which includes the geothermal reservoir of interest for electrical power generation. It, therefore, encompasses the region for which the bulk of the available geohydrologic data have been generated.

Once we have developed a computer simulation of the natural flow of fluid and heat in the subregion modeled (Figure 5), we intend to apply the model to examine the response of the integrated system to large scale flow of geothermal fluid and associated heat transport. In these model applications it will be necessary to specify the fluid recharge, (A) , and discharge, (E) , fluxes along the periphery of the modeled subregion as well as the convective source, (C) , at its bottom. The mass flux at the boundary points in these transient studies can be approximated by scaling the flux magnitude according to the change in pressure from its steady-state value as calculated by the natural flow model. Specifically, consider a point on the bottom boundary of the subregion for which the steady-state natural mass flux is approximated by

$$\dot{m}_o = \beta(\rho_{cold} - \rho_{hot})gh \qquad (1)$$

where h is the depth of the modeled subregion, $\rho_{cold}\, gh$ is the external cold water hydrostat which drives the circulation in the full hydrothermal system, and $\rho_{hot} gh$ is the internal hot water hydrostatic pressure at the point in question. This relation assumes that fluid flow outside the subregion is Darcian. The natural flow model may be used to define the constant β as follows:

$$\beta = \frac{\dot{m}_o}{(\rho_{cold} - \rho_{hot})gh}$$

Accordingly, the convective flux which will accompany transient flow within the modeled subregion may be approximated by

$$\dot{m} = \dot{m} + \beta \Delta p \qquad (2)$$

where Δp is the change in pressure at the bottom of the modeled subregion at the point in question.

There are no direct experimental data available for the vertical permeability of the geothermal cap which separates the shallow confined aquifer from the geothermal reservoir in the East Mesa system. It will be necessary to examine the response of the integrated shallow and deep hydrothermal systems through a series of parametric calculations in which the obviously low vertical permeability (e.g., 10^{-3} to 10^{-1} md) is varied. The leakage of fluid across the cap will likely be small enough that its effect on large scale transport processes within the geothermal reservoir may be neglected and the response of the deep system modeled in a decoupled analysis. The result of the decoupled analysis can then be employed to assess the effect of the large scale geothermal fluid transport on the shallow system. For example, suppose the decoupled analysis shows that the pressure at a point at the top of the geothermal reservoir (i.e., bottom of geothermal cap) is changed from its initial steady-state value p_o to $p(t)$. The transient mass flux across the cap thickness H at that point can then be estimated by Darcy's law,

$$\dot{m} = \phi \rho v = \frac{k_v \rho}{H} \Delta p \quad (\Delta p = p(t) - p_o) \qquad (3)$$

III. PERTINENT DATA BASE

3.1 GEOLOGY AND GEOPHYSICS

The structure of the Imperial Valley is controlled by numerous strike-slip faults of the San Andreas and San Jacinto fault system. The project study area has been selected such that its two sides approximate the surface traces of two major faults in this system, the Imperial Fault and the San Andreas Fault (Figure 6). Electrical resistivity measurements by the University of California, Riverside group show clear differences in resistivity of the rocks on the two sides of each of these faults (Rex, et al. [1971]). The U. C. Riverside researchers interpreted this as indicating discontinuities in the salinity of the ground water on the two sides and suggest that both faults act as impermeable barriers retarding westward flow of the groundwater from the Colorado River. The two faults were assumed to be sealing faults in Miller's study of horizontal flow in the shallow confined aquifer (Figure 3).

Figure 6 also shows the altitude in 1965 of the groundwater level in feet above (+) or below (-) mean sea level for the Imperial Valley of California. Near the center of the East Mesa geothermal anomaly, denoted by an asterisk, the groundwater flow in the shallow hydrothermal system is essentially west-north-west along the direction DD' depicted in Figure 6. Because of the poor connection between the shallow and deep systems, however, the pressure gradient and flow direction in the deep hydrothermal system cannot be inferred from the level of the groundwater table.

As indicated in the conceptual model shown in Figure 5, faults can act not only as flow barriers, but also as conduits for rising geothermal fluids or descending cold groundwater. At an early stage of the geophysical explorations at the East Mesa anomaly, three

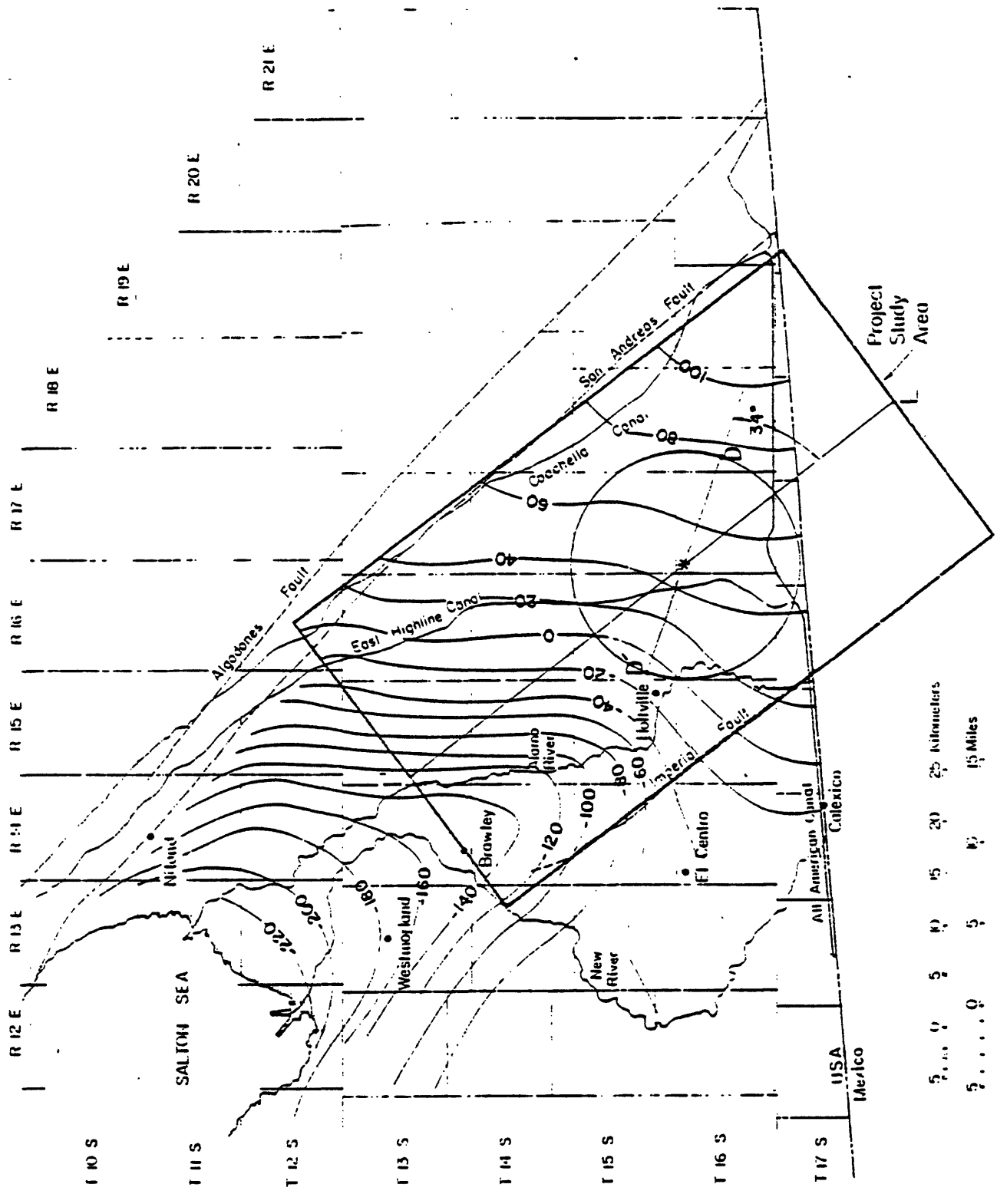
R 12 E
R 13 E
R 14 E
R 15 E
R 16 E
R 17 E
R 18 E
R 19 E
R 20 E
R 21 E
T 10 S
T 11 S
T 12 S
T 13 S
T 14 S
T 15 S
T 16 S
T 17 S
SALTON SEA
Niland
Westmorland
Brawley
El Centro
Calexico
Holtville
Imperial
Algodones Fault
San Andreas Fault
East Highline Canal
Coachella Canal
Alamo River
New River
All American Canal
Project Study Area
USA
Mexico
-20
-40
0
20
40
60
80
100
120
140
160
180
200
220
240
260
280
300
320
340
360
380
400
420
440
460
480
500
520
540
560
580
600
620
640
660
680
700
720
740
760
780

faults with no surface expression (Rex Fault, Babcock Fault and Combs-Hadley Fault) were inferred by indirect means such as resistivity survey, microseismic activity and oblique areal infrared photography. The inferred results intersect near the center of the high heat flow region and Combs and Hadley [1977] hypothesized that the convective upwelling of hot fluid in an associated deep vertically fractured region is the cause of the measured abnormal surface heat flow. Figure 7 shows the surface traces of the three inferred faults superposed on the surface heat flow contours at East Mesa that have been presented by TRW.

Recently, the Lawrence Berkeley Laboratory has mapped the structure in the East Mesa area using seismic reflection data (Howard, et al. [1978]). Numerous faults were located and the center of the geothermal anomaly was found to be on a complex geologic structure. The blue (Figure 8), orange (Figure 9) and yellow (Figure 10) seismic markers show a major anticline to the north trending southwest with a flanking syncline to the south. Both folds plunge into the southwest, toward the center of the Salton Trough. Another seismic structure map (Figure 11) was made on top of a poorly reflective zone. The LBL group believes the rock within this zone to be highly fractured and to represent potential zones for geothermal fluid production.

Two prominent faults trending northwest, with displacements of 100 to 200 feet or more down to the west and dipping to the southwest, are evident in Figures 8 through 11. These are in general alignment with the inferred Combs-Hadley Fault in Figure 7. The numerous north-trending faults have displacements of about 50 to 100 feet, generally sloping to the west. These are in general alignment with the inferred Babcock Fault in Figure 7. It is of interest to note that the intersection of these two faults sets at a depth below the top of the poorly reflective zone lies further south than the intersection of their surface traces.

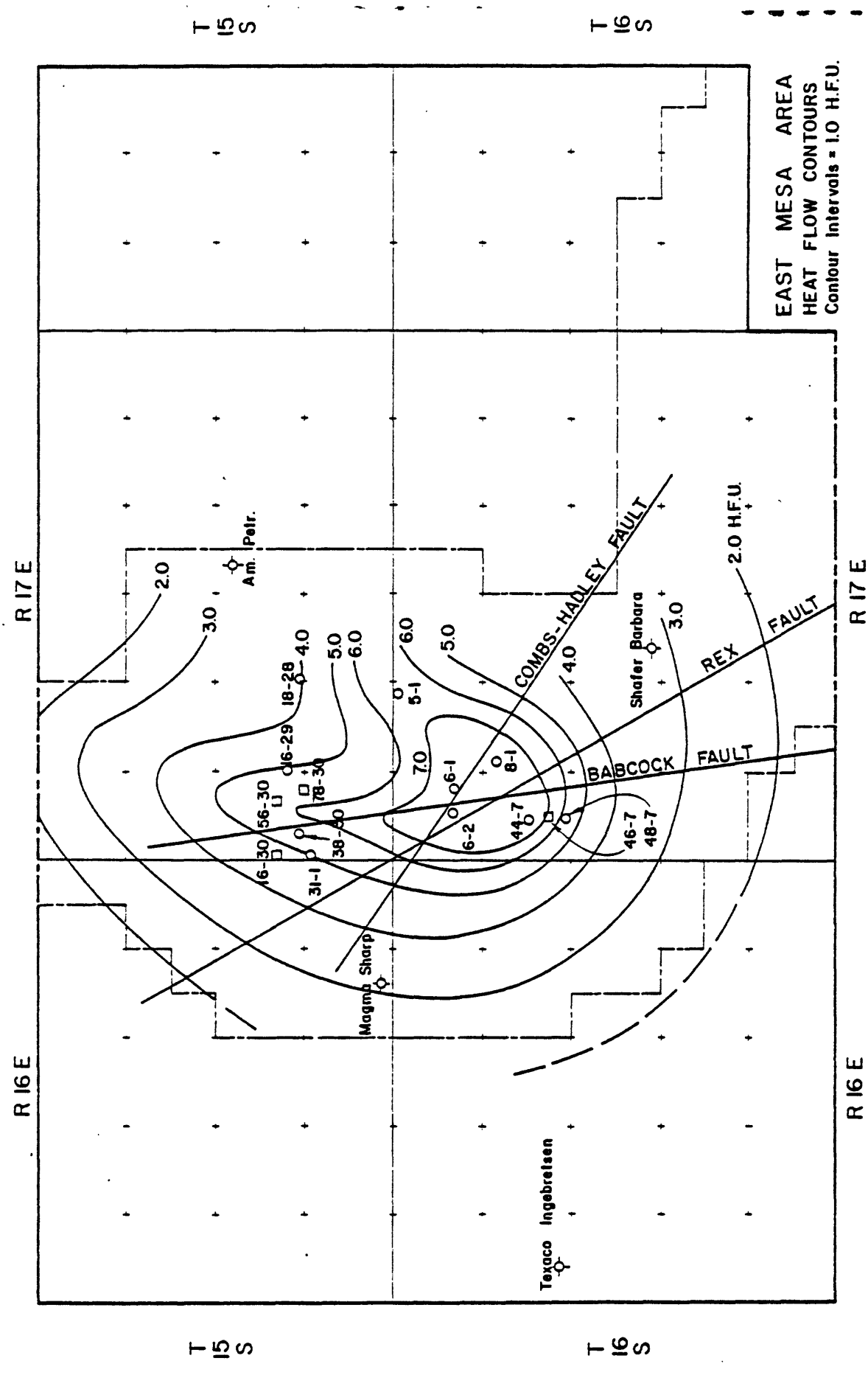

Figure 7. Surface heat flow contours taken from TRW results (Pearson [1976]). Locations of the four geothermal wells drilled subsequent to TRW analysis are denoted by □.

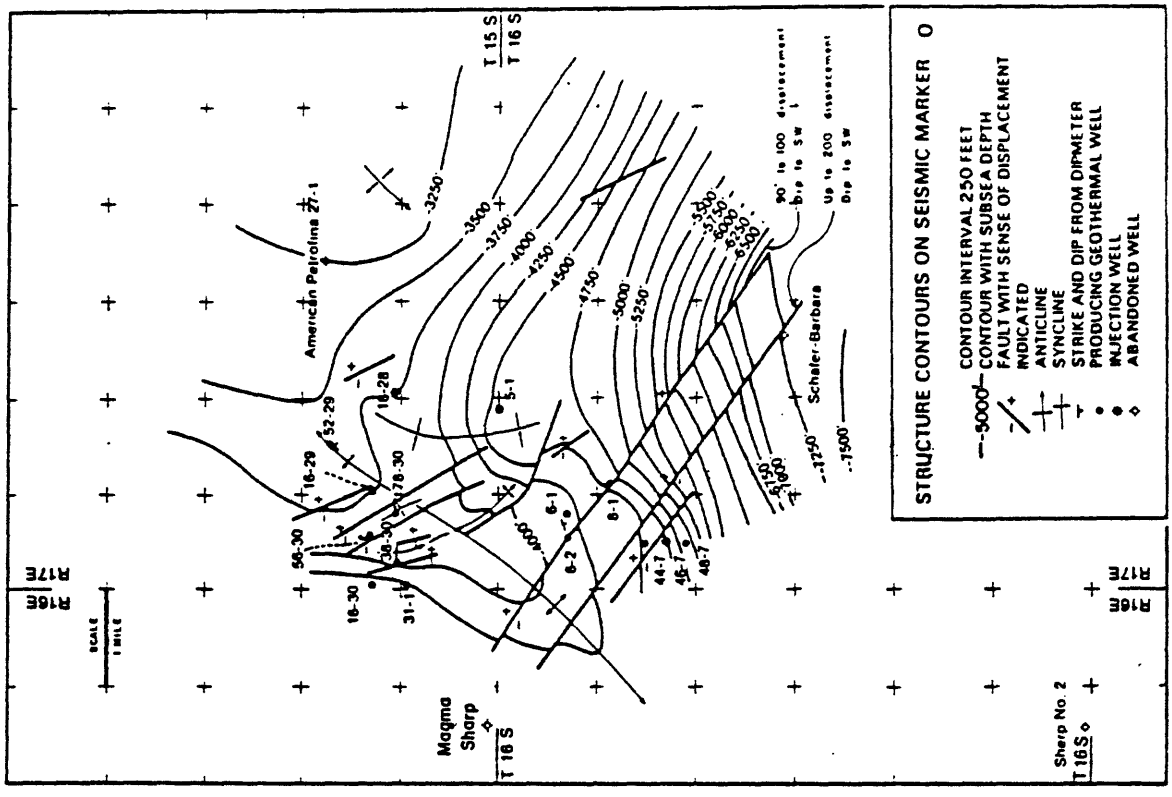

Figure 9. Structure contours on seismic marker O (Howard, et al. [1978]).

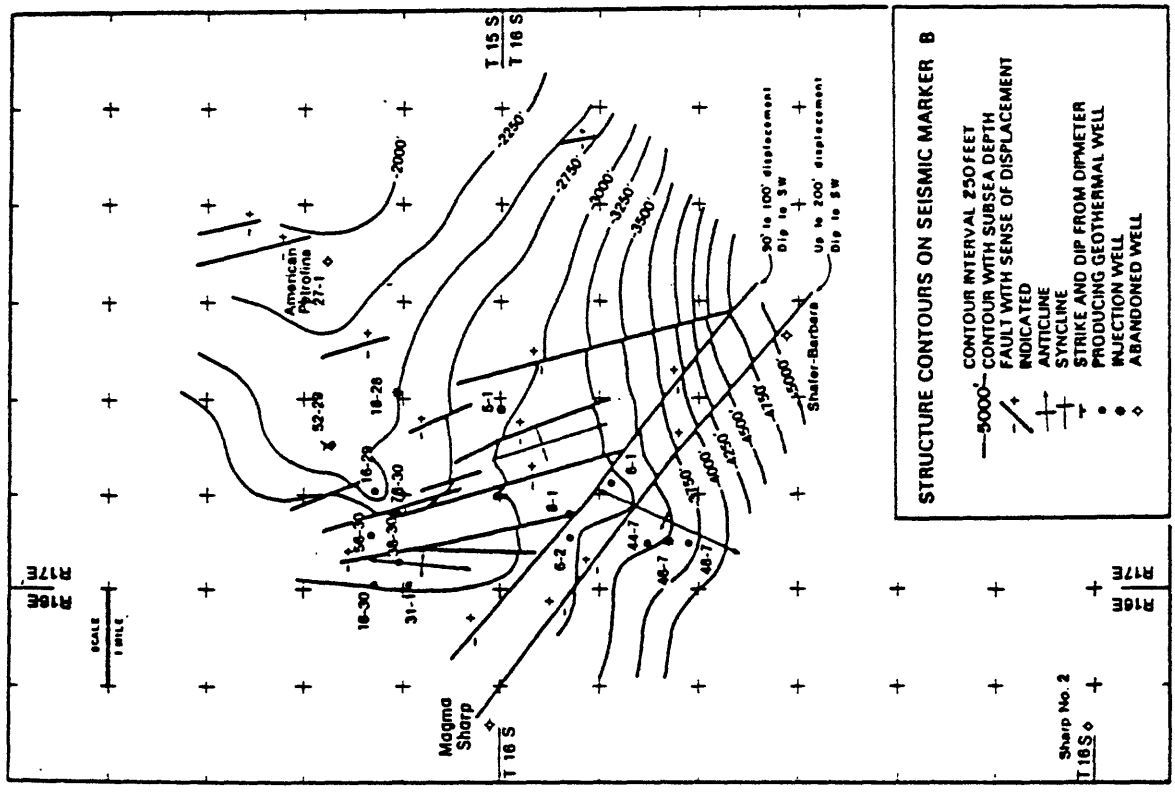

Figure 8. Structure contours on seismic marker B (Howard, et al. [1978]).

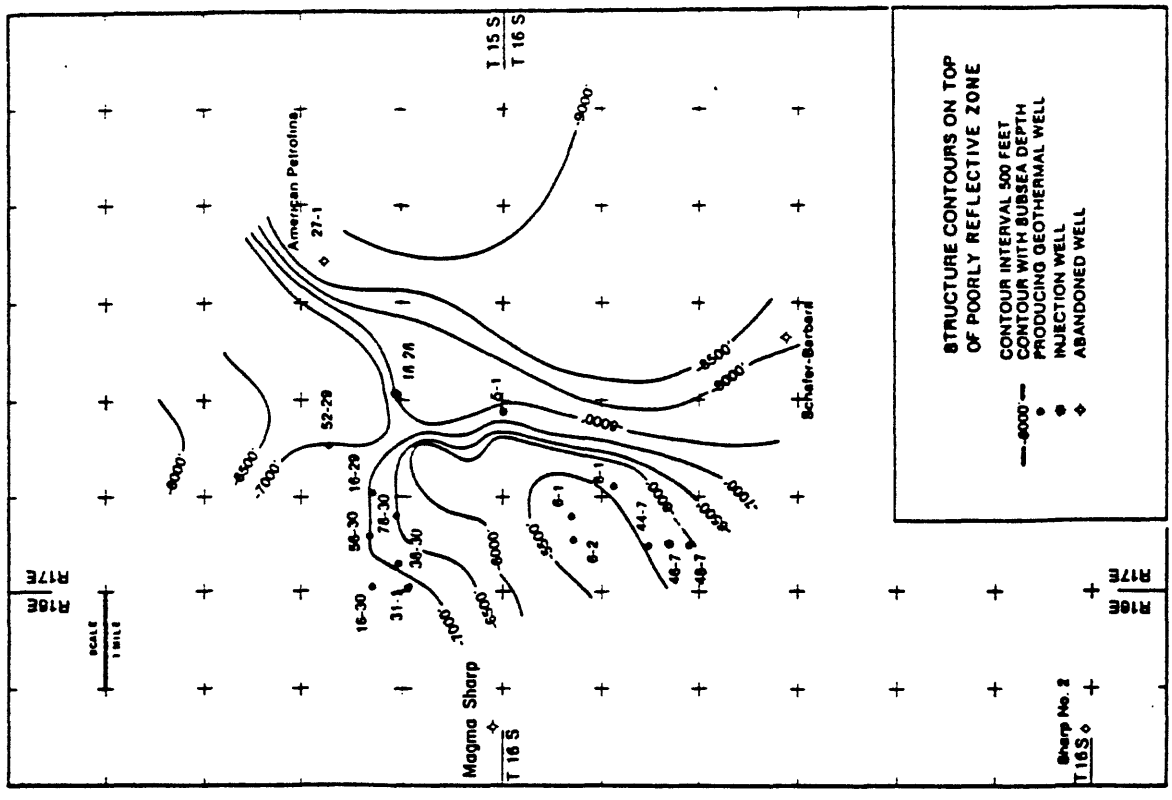

Figure 11. Structure contours on top of poorly reflective zone (TPRZ) (Howard, et al. [1978]).

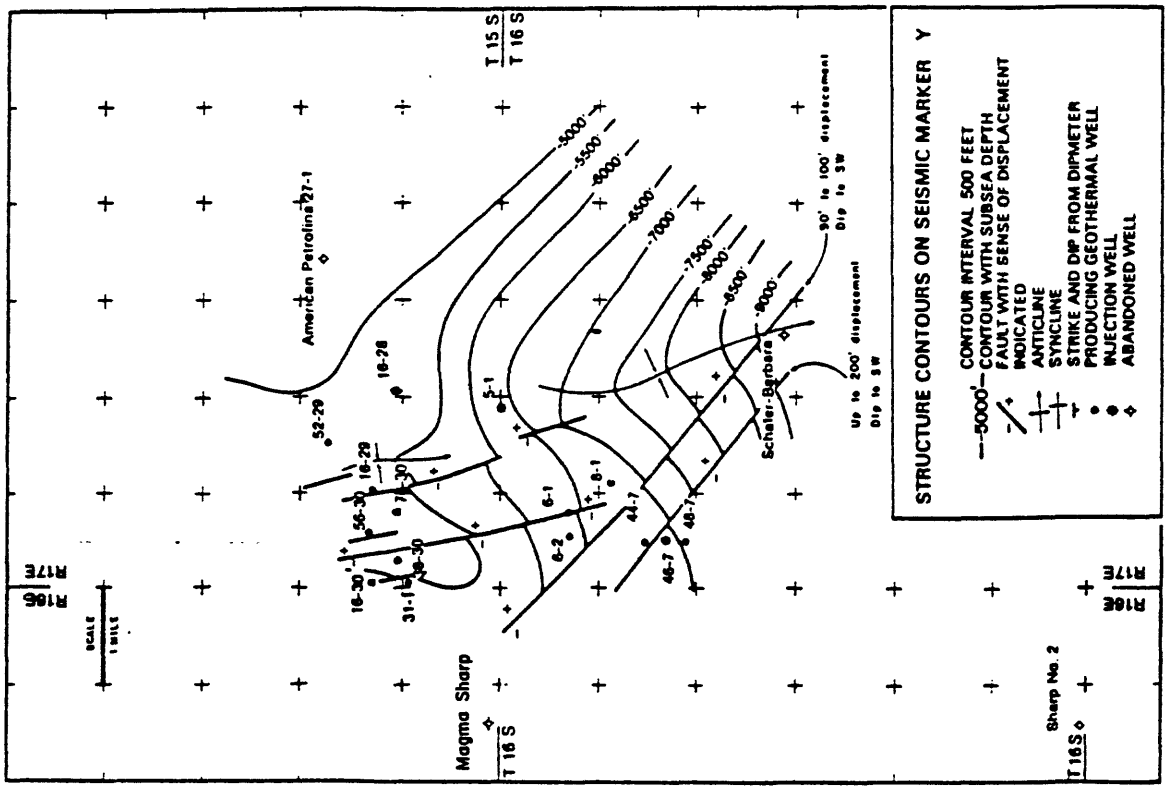

Figure 10. Structure contours on seismic marker Y (Howard, et al. [1978]).

The heat flow contours in Figure 7 are based on heat flow measurements made in shallow drill holes in the area. The raw data were reanalyzed in a TRW staff report [1976] and summarized by Pearson [1976]. The heat flow measurements extrapolate to surface temperatures between 80° and 90°F, rather than to the mean annual temperature of 73°F, probably due to poor thermal conductivity of the layer of unsaturated sandy soil above the water table. The water table is rising in some places in the East Mesa area due to influx of water from the irrigation canals. The TRW analysis accounts for such disturbances and provides consistent results by using different values for the effective thermal conductivity above and below the Z = 325 foot horizon:

$$\kappa_{eff} = 1.30 \times 10^5 \text{ ergs/sec-cm-°C} \quad Z < 325 \text{ feet} \qquad (4)$$

$$= 1.76 \times 10^5 \text{ ergs/sec-cm-°C} \quad Z > 325 \text{ feet}$$

The surface heat flow contours presented by TRW (Figure 7) represent curve fits to their interpretations of shallow hole heat flow measurements. The two distinct lobes to the north and northeast are the most apparent features of the contours. They imply unexpectedly sharp variations in the surface heat flow since heat conduction through the geothermal cap is a diffusive process and there are no known surface manifestations of geologic or hydrologic discontinuities along these two directions. Since the details of the contours may be associated with data scatter due to local inhomogeneities and curve fitting, we have reproduced the basic heat flow data points as interpreted by TRW in Figure 12. It is apparent that the two lobes lie within areas of higher heat flow, but the data do not justify the detail exhibited by the contours.

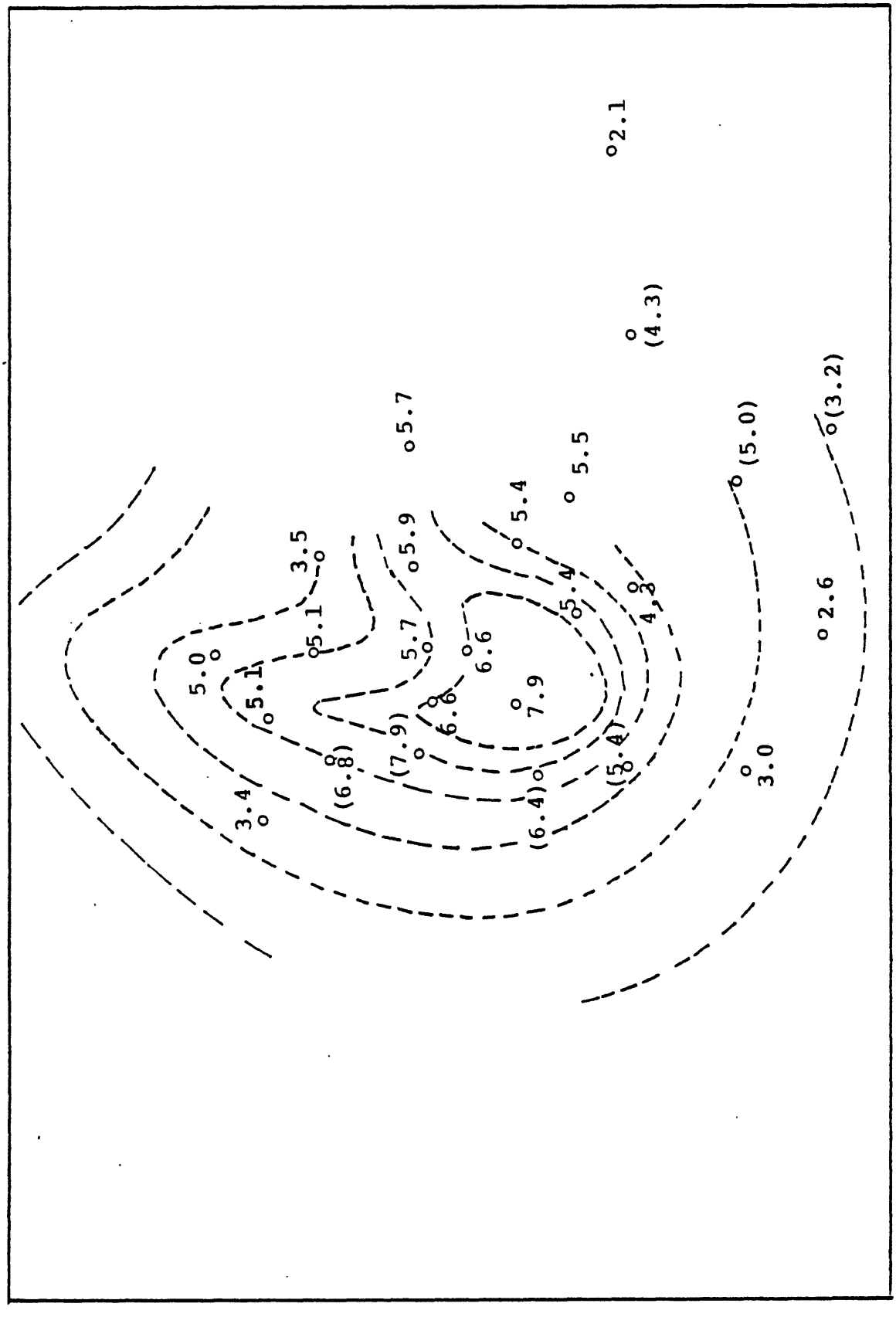

Figure 12. Surface heat flow at indicated shallow hole locations as interpreted by TRW (Pearson [1976]). Values in parentheses are at holes where data interpretation is considered by TRW to be possibly misleading.

3.2 SUBSURFACE DATA

Through 1976, ten producing geothermal wells had been drilled at East Mesa, including three by Republic Geothermal, Inc. (38-30, 16-29, 18-28) in the northern portion of the reservoir, five by the U. S. Bureau of Reclamation (6-1, 6-2, 5-1, 8-1, 31-1) in the central area, and two by Magma Power Company (44-7, 48-7) to the south. Four older abandoned deep oil test holes (Shafer Barbara, Texaco Ingebretsen, Magma Sharp, American Petrofina) are also in the general area. During 1977, Republic drilled three more wells (56-30, 78-30, 16-30) and Magma drilled a third well (46-7). The locations of all eighteen of these wells are shown in Figure 7. The TRW staff report [1976] analyzed data from the original fourteen wells and their report is a major source of information for this study. Analyses by University of Colorado researchers (Black [1975]; Bailey [1977]; Kassoy and Zebib [1978]; Goyal [1978]) have provided information on the newer wells as well as additional data analyses and concepts on the natural flow of heat and fluid mass within the geothermal reservoir.

Figure 13 shows the equilibrium temperature versus depth profile measured in the BuRec Mesa 6-2 well located at the center of the high heat flow region. Similar plots available from geothermal and oil test wells were used by TRW to graphically construct the approximate subsurface temperature contours at 1000 feet depths in the geothermal reservoir. This approximation assumes that the equilibrium temperature of the fluid in the well casing represents the predrilling temperature of the formation and thus ignores convection within the well. The TRW construction method interpolated between well data and surface heat flow information (Figure 7) by assuming that heat flow at depths above 2000 feet is purely by conduction but that fluid convection dominates below that level. Figure 14 illustrates the TRW results at a depth of 6000 feet.

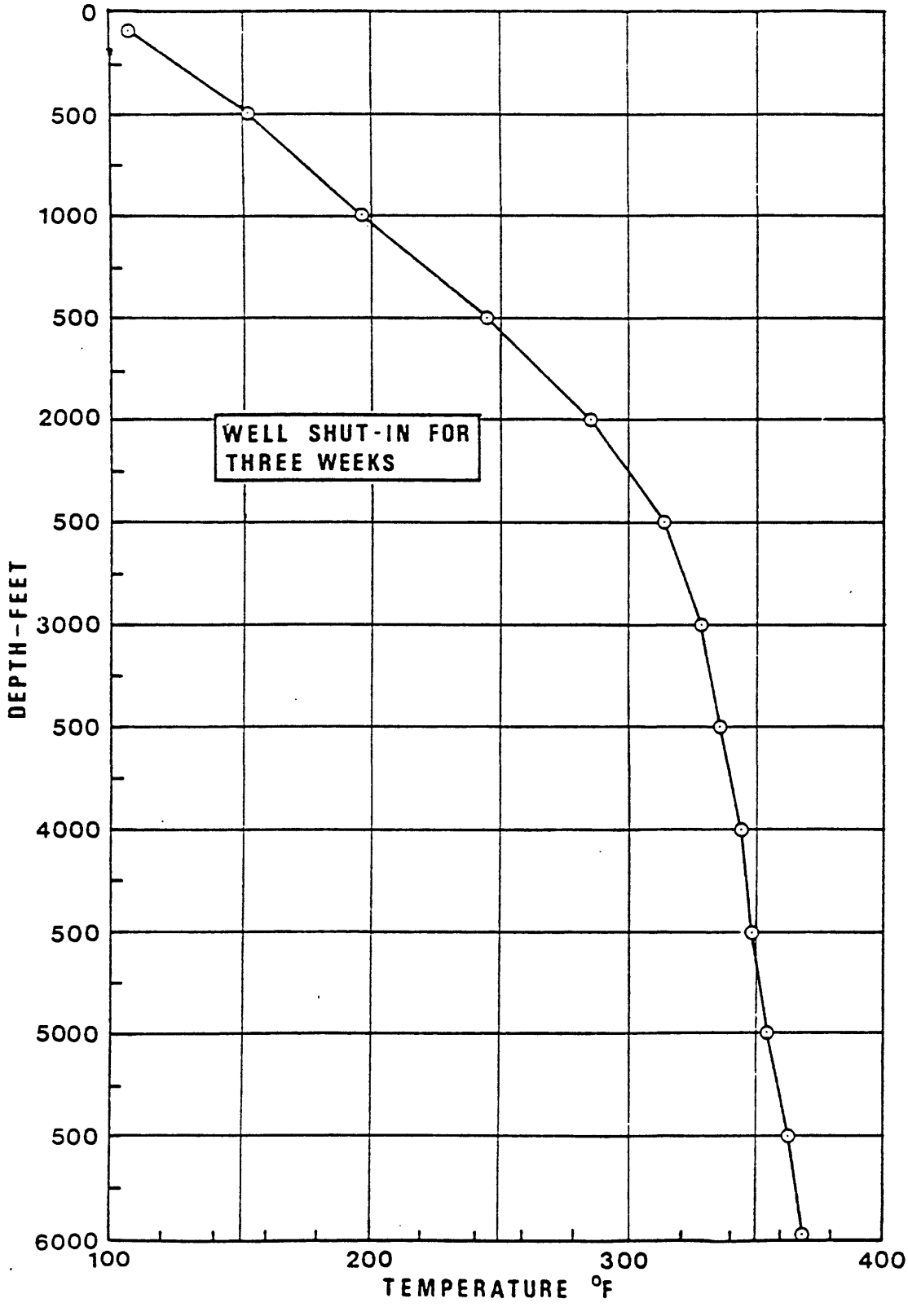

Figure 13. Temperature profile for Mesa 6-2 well measured October 15, 1973 after three-week shut-in (U. S. Bureau of Reclamation [1974]).

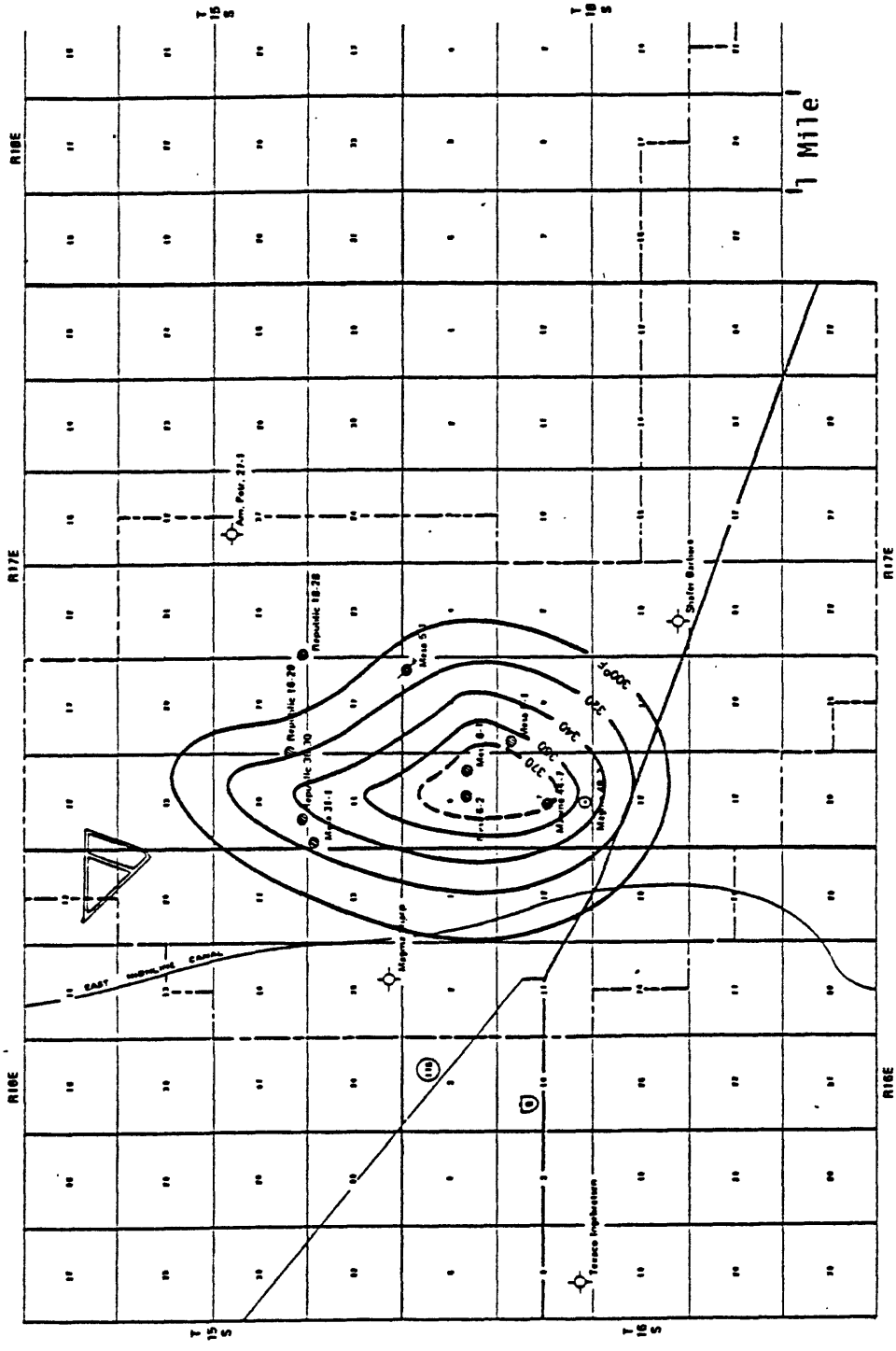

Figure 14. East Mesa temperature contours at 6,000 feet depth (Pearson [1976]).

The average porosity of the sandstone in 50-feet intervals and the average formation porosity of each 50-feet interval are plotted as a function of depth for the Mesa 6-1 well in Figure 15. The interbedded sandstone/shale formation porosity (ϕ) shown there is calculated by ignoring any shale porosity:

$$\phi = \frac{\text{Sand Porosity x Net Sand Thickness}}{\text{Interval Thickness}} \qquad (5)$$

Sands in the upper 700-850 meters have the highest porosities but the sandstone/shale formation porosities are quite low because of the presence of a large percentage of interbedded shales.

TRW used a sand/shale discriminator to compute the net sand available in 250-feet intervals of the East Mesa formations penetrated by the fourteen geothermal and oil test wells for which logs were then available (Pearson [1976]). The interval summaries of the net sand thicknesses and sand porosities are illustrated by the results for the BuRec wells presented in Table 1. TRW also derived porosity and permeability transforms for sandstone core data from wells in the East Mesa area. The transforms relate horizontal permeability (K_h) and vertical permeability (K_v) of the sandstone to sandstone porosity (Φ) according to

$$\log K_h = 13.614\Phi - 1.8126$$

$$\log K_v = 0.940 \log K_h - 0.0436 \qquad (6)$$

(A word about notation; hereafter upper case K will be used to denote permeability of the sand component alone; lower case k denotes the effective formation permeability of the sand/shale system as a whole)

Porosity and permeability, both horizontal and vertical, were then computed by the above relations on a foot-by-foot basis within each net sand interval. The interval summaries for the sand permeabilities derived in this manner are also illustrated by the results for the BuRec Wells shown in Table 1.

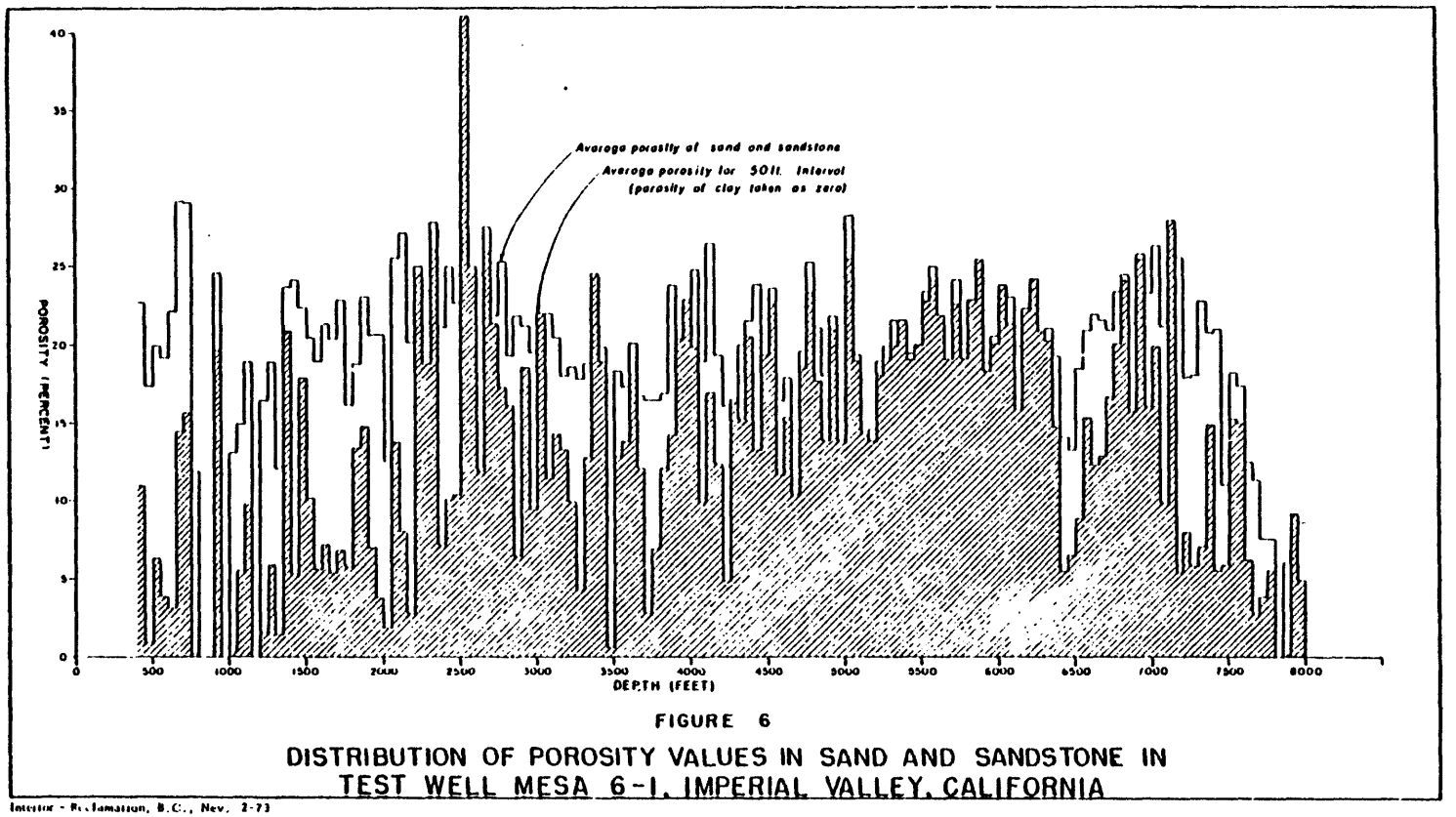

FIGURE 6

DISTRIBUTION OF POROSITY VALUES IN SAND AND SANDSTONE IN TEST WELL MESA 6-1, IMPERIAL VALLEY, CALIFORNIA

Interior - Reclamation, B.C., Nov. 2-73

Figure 15. Distribution of porosity values in sand and sandstone in formation penetrated by Mesa 6-1 well (U. S. Bureau of Reclamation [1973]).

TABLE 1

Interval Summaries Prepared by TRW from Core and Log Data for the BuRec Wells (Pearson [1976])

	MESA 6-1				MESA 6-2				MESA 8-1				MESA 5-1				MESA 31-1			
Interval (feet)	H	ϕ	K_h	K_v	H	ϕ	K_h	K_v	H	ϕ	K_h	K_v	H	ϕ	K_h	K_v	H	ϕ	K_h	K_v
1001 - 1250	-	-	-	-	15	36	1469	785												
1251 - 1500	-	-	-	-	29	35	1582	602					124	34	927	429	88	32	493	230
1501 - 1750	-	-	-	-	91	35	1073	519	25	32	676	207	114	33	631	292	137	32	471	206
1751 - 2000	-	-	-	-	121	34	997	438	106	31	493	187	124	35	1379	552	81	33	805	357
2001 - 2250	-	-	-	-	114	33	608	266	94	32	871	247	179	34	877	412	146	31	431	185
2251 - 2500	-	-	-	-	138	32	642	261	188	30	437	135	161	32	470	232	112	32	880	226
2501 - 2750	173	30	326	112	139	32	461	208	169	29	250	95	204	31	383	183	118	32	699	233
2751 - 3000	136	26	154	43	196	31	400	183	170	29	363	100	164	30	227	122	191	31	403	163
3001 - 3250	146	24	62	25	129	28	182	79	168	24	69	24	156	29	165	84	149	29	178	90
3251 - 3500	130	23	65	18	165	29	275	98	157	23	71	15	140	25	62	33	158	28	142	62
3501 - 3750	123	19	20	6	138	25	148	29	133	16	3	2	162	26	88	37	130	28	171	80
3751 - 4000	166	28	282	69	85	22	37	11	143	17	9	3	202	25	63	26	55	29	215	85
4001 - 4250	155	24	177	23	148	28	249	64	203	21	35	9	167	25	74	28	192	28	148	65
4251 - 4500	184	26	321	35	172	26	96	34	152	13	22	4	199	22	30	13	184	27	97	51
4501 - 4750	195	25	373	30	184	26	280	35	183	24	57	23	196	25	74	27	133	26	74	38
4751 - 5000	187	29	649	86	170	27	198	54	180	19	18	6	140	26	80	35	175	27	110	52
5001 - 5250	147	22	328	14	144	20	21	7	190	19	11	5	156	24	57	24	151	26	69	34
5251 - 5500	192	24	160	24	172	20	27	6	136	17	8	3	168	23	37	16	175	25	60	29
5501 - 5750	194	24	59	20	142	23	36	14	156	13	14	4	184	24	49	22	155	24	55	20
5751 - 6000	137	24	44	21					198	22	30	13	212	24	53	24	138	25	117	29
6001 - 6250	183	23	42	17																
6251 - 6500	139	20	25	7																
6501 - 6750	82	22	27	11																
6751 - 7000	148	28	197	65																
7001 - 7250	98	26	91	40																
7251 - 7500	-	-	-	-																

H = net sand thickness (feet)

ϕ = average porosity (percent) of sands

K_h = average horizontal permeability (millidarcies) of sands

K_v = average vertical permeability (millidarcies) of sands

3.3 RESERVOIR FORMATION PROPERTIES

By late 1977, a total of fourteen wells had been drilled to explore the East Mesa geothermal reservoir: five by BuRec, six by Republic and three by Magma. Lawrence Berkeley Laboratory (LBL) commenced carrying out well tests in 1976 in order to assess the fluid flow characteristics of the reservoir (Witherspoon et al. [1978]; Narasimhan et al. [1978]). The interference tests conducted on the BuRec wells suggest that the transmissivity kh (horizontal formation permeability x reservoir thickness tested) of the reservoir in the vicinity of wells 6-1 and 6-2 is ~ 20,000 md-feet. Interference data from Republic well 31-1, which is further removed from the center of the geothermal anomaly, indicate a (kh) value of ~ 26,000 md-feet. Interpretation of the observation well data led to estimates of (kh) ranging from 21,000 to 35,000 md-feet and to the presence of a barrier boundary trending north-north-east and passing a little to the east of well 16-30 (see Figure 7). The slotted intervals for the wells range from about 500 to 1,500 feet at the depths tested which range from between 5,000 feet and 8,000 feet. The tests imply that the horizontal formation permeability is k_h ~ 15-20 md near the central lower part of the reservoir and suggest that permeability increases as one moves away from the center of the hot spot.

To provide a reference framework for constructing a model which includes the variations of the thermal and geohydrological characteristics of the region studied, we have divided the East Mesa reservoir system into six horizontal layers. Layer 1 (0 < depth < 700-feet) is intended to roughly correspond to the integrated effect of the water table aquifer, the confining zone, and the confined aquifer (depicted in Figure 4). This three-component shallow system has been analyzed by Miller [1977] and will not be treated explicitly here. Layer 1 has good porosity (average formation porosity ϕ ~ 0.30) and sand content. Layer 2 (700 < depth < 2,500 feet) has high snale content and restricted vertical permeability.

The vertical permeability is low enough that this layer serves as the geothermal reservoir cap. The sand content gradually increases in the lower half of the layer. Layer 3 (2,500 < depth < 5,000 feet) and Layer 4 (5,000 < depth < 7,000 feet) contain the geothermal reservoir; a gradual decrease in percentage of sandstone occurs in the reservoir at approximately 6,200 feet and a more abrupt decrease occurs below 7,000 feet. Layer 5 (7,000 < depth < 8,000 feet) represents the transitional zone between the reservoir and the upper part of the shale-rich sedimentary sequence that extends to the basement complex located at a depth greater than 12,000 feet. Layer 6 (8,000 < depth < 10,000 feet) represents part of the shale-rich sequence.

Vertical sections passing through the center of the high surface heat flow area have been constructed from the available data base for the East Mesa project area. The asterisk in the Figure 6, located midway between the Mesa 6-1 and 6-2 wells, denotes the intersection point for the vertical sections and LL' shown there indicates the vertical (southeast-northwest) section which is parallel to the sides of the project study area. A west-east (WE) section and a south-north (SN) section through the hot spot were also constructed. Figures 16 through 18 show the surface heat flow distributions and the subsurface temperature contours along these sections that were determined from the TRW results. The locations of the projections of the fourteen wells included in the TRW data analysis are shown on the three sections for reference purposes.

The sand porosities for the 250-feet intervals prepared by TRW (e.g., Table 1) for the geothermal and oil tests wells in the East Mesa area were used to estimate average formation porosities in the six horizontal layers. The resulting formation porosity distributions along the three vertical sections are shown in Figures 16-18. The formation porosity, in the vicinity of the wellbore, within a layer penetrated by the well was computed by a formula analogous to Equation (5):

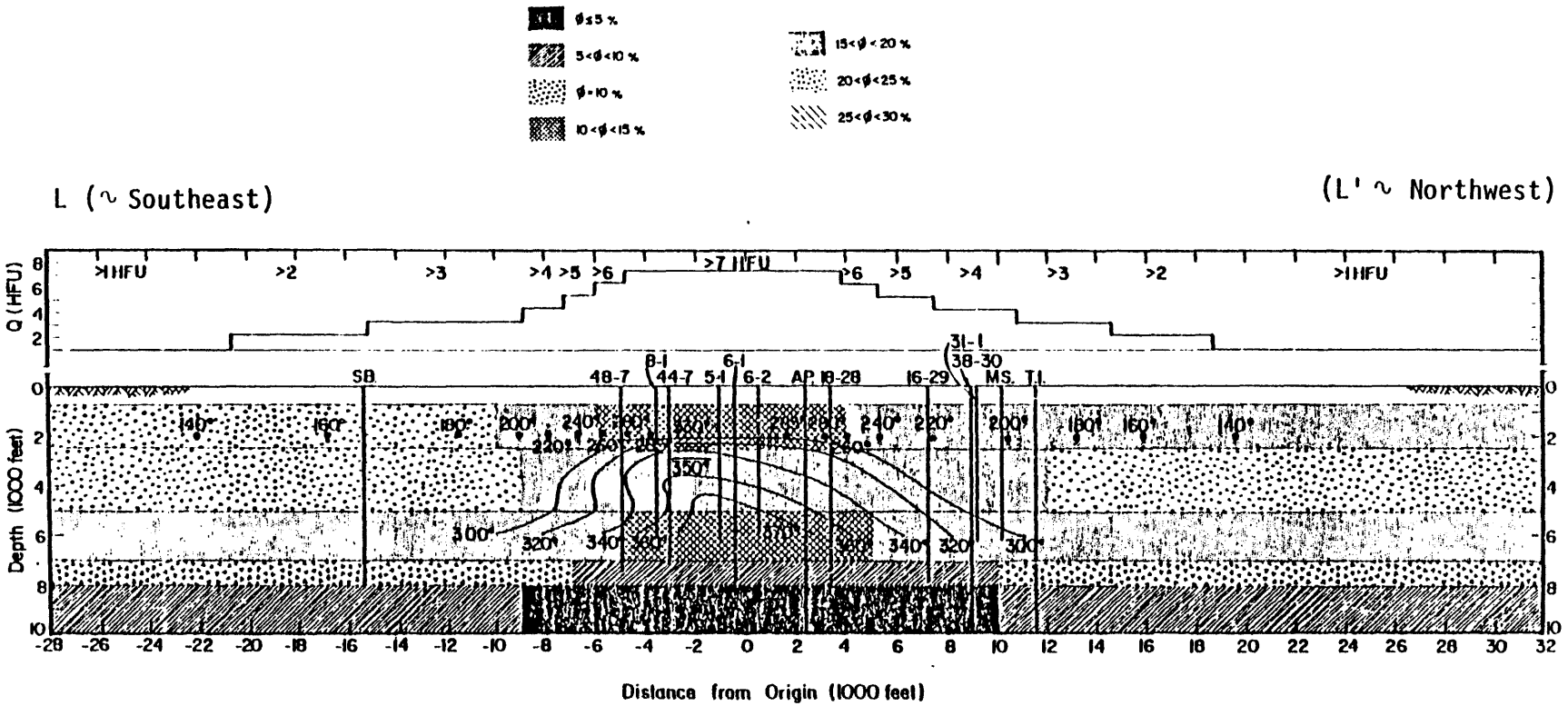

Figure 16. Vertical section LL' which runs lengthwise (southeast to northwest) through origin, asterisk in Figure 6, of project study area. Distributions of subsurface temperature (°F), surface heat flow, and approximate formation porosity are shown along LL'.

SSS-R-80-4362

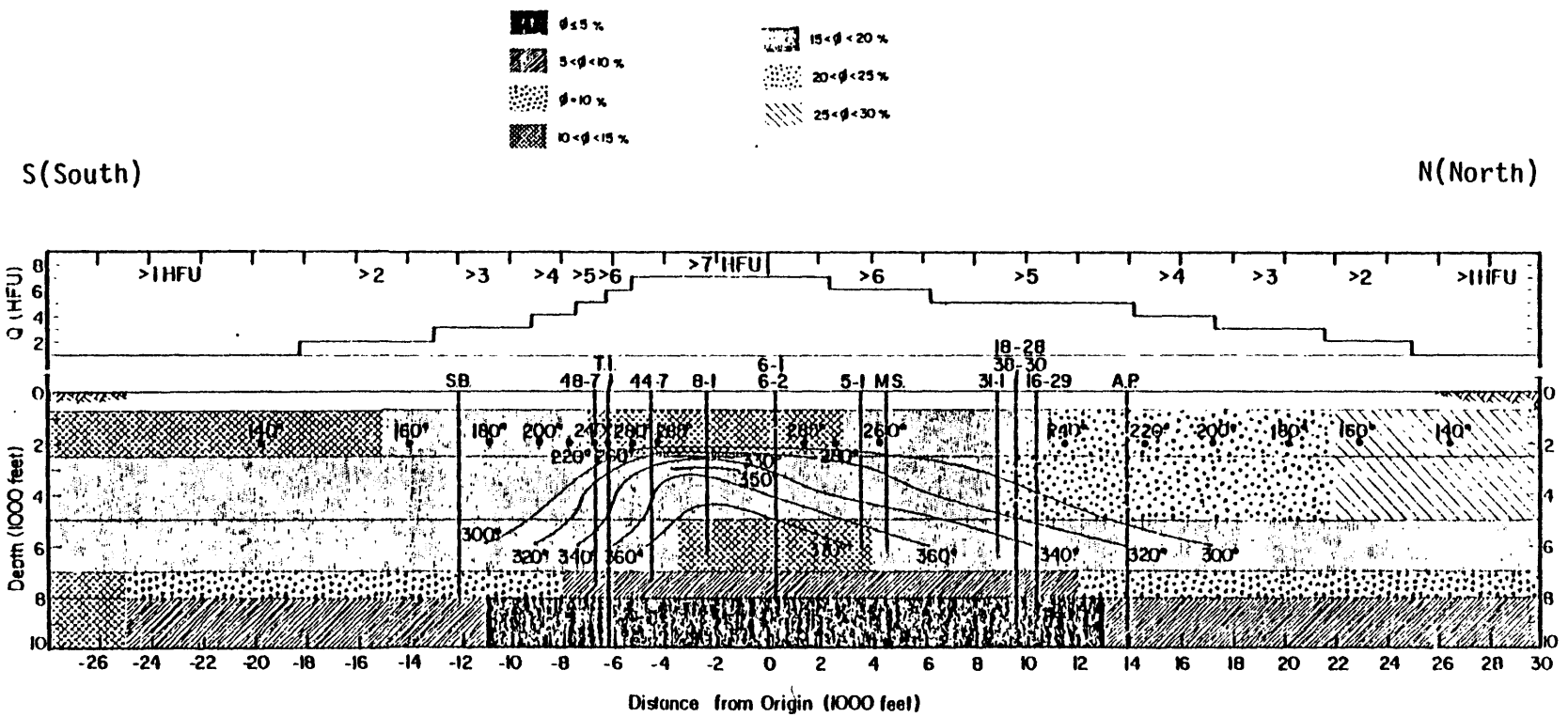

Figure 17. Vertical section SN which runs south to north through origin, asterisk in Figure 6, of project study area. Distributions of subsurface temperature (°F), surface heat flow, and approximate formation porosity are shown along SN.

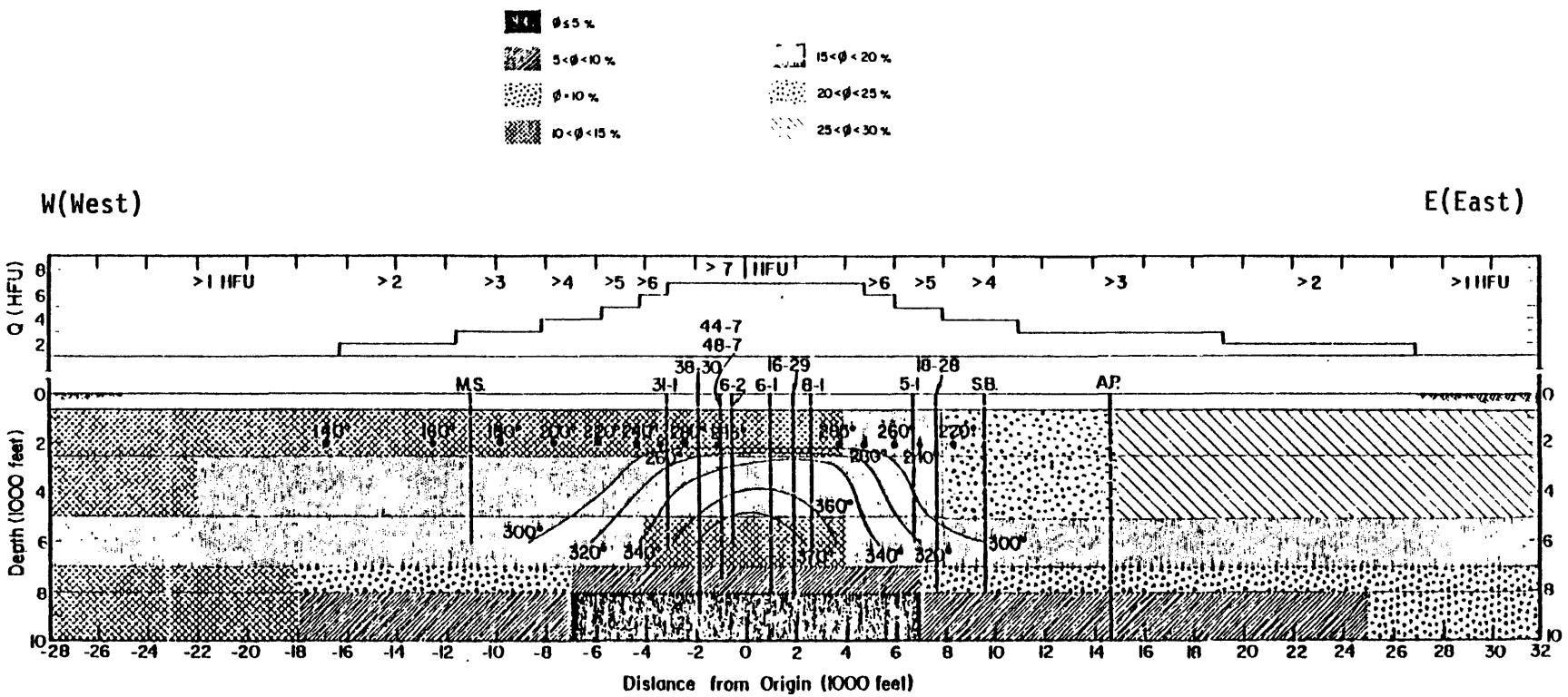

Figure 18. Vertical section WE which runs west to east through origin, asterisk in Figure 6, of project study area. Distributions of subsurface temperature (°F), surface heat flow, and approximate formation porosity are shown along WE.

SSS-R-80-4362

$$\phi = \frac{\sum H_i \Phi_i}{\text{Layer Thickness}} \qquad (7)$$

where H_i and Φ_i are the net sand thickness and average sand porosity in the i-th 250-feet interval and the sum extends over all such intervals in the layer. The extrapolation of the data from the fourteen wells to estimate the three-dimensional formation porosity distribution depicted in Figures 16-18 is necessarily subjective and at best only approximately correct. Nevertheless, it appears to show the general trends which current information implies and appears adequate for the overall model of the system which we wish to develop. Above 7,000 feet the sand content generally decreases from east to west and, consequently, the formation porosity also decreases. Below 7,000 feet, the formation porosity is low throughout the region studied; the porosity generally decreases with depth. There is also a general decrease in the porosity within the geothermal resource region relative to the surrounding region.

The horizontal permeabilities of the sands for the 250-feet intervals prepared by TRW (e.g., K_h in Table 1) can be used to estimate the horizontal formation permeabilities (k_h) within each layer penetrated by the fourteen wells studies by TRW. The interbedded shales and sands within each layer are assumed to be horizontal and flow through the shales is neglected so that

$$k_h = \frac{\sum H_i K_{hi}}{\text{Layer Thickness}} \qquad (8)$$

The computed values of log k_h are plotted against the corresponding values of the formation porosity (ϕ) in Figure 19, analogous to Equation (6). The data are approximated by the two intersecting straight lines shown there. From the LBL well test results we know that in Layer 4 (5,000 < depth < 7,000 feet), the in situ horizontal formation permeability k_h ~ 20 md near the center of the

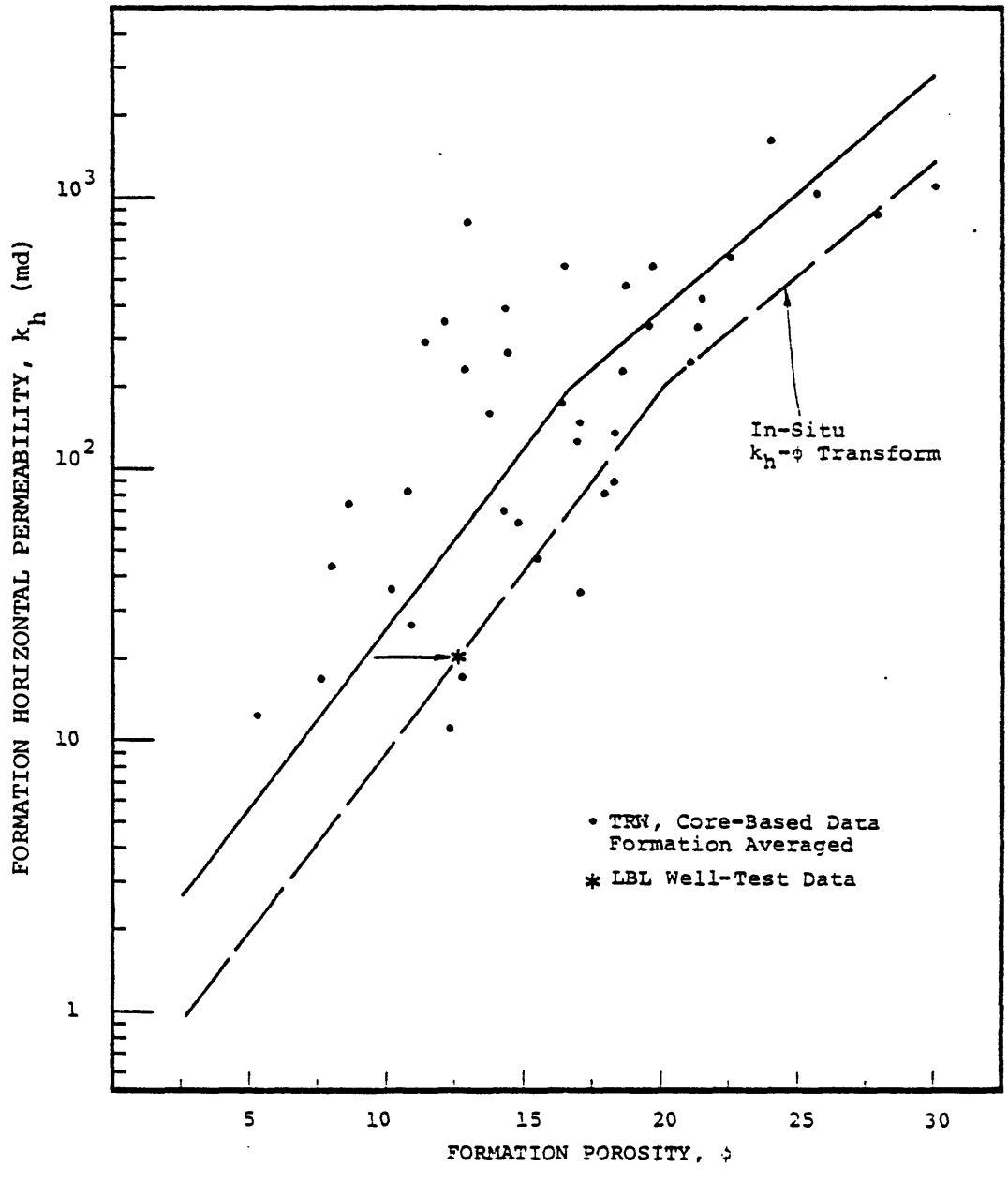

Figure 19. Formation porosity-horizontal permeability transform.

geothermal reservoir where, according to Figures 16-18, $\phi \sim 10$-15 percent. The bi-linear fit, based on core data, is, therefore, translated to pass through the LBL data point in Figure 19.

In the absence of more reliable information, the dashed bi-linear curve in Figure 19 has been used to estimate horizontal formation permeability from the value of the formation porosity. For example, from Figures 16-18 the approximate porosities at the center of the heat flow region are as shown in Table 2. The corresponding approximation for the horizontal formation permeabilities shown there are read from Figure 19.

TABLE 2
Approximate Formation Porosities and Horizontal Permeabilities at Center of Heat Flow Region

Layer	ϕ(%)	k_h (md)
2	10-15	20
3	15-20	90
4	10-15	20
5	5-10	4
6	0-5	1

Since the interbedded shales and sands within each formation layer are predominantly horizontal, the vertical formation permeability (k_v) will be drastically restricted by the nearly impermeable shales. Except for flow within vertical fractures, any net vertical flow will likely follow tortuous paths around the ends of the interbedded shales, if such sand paths are in fact available. In the absence of any direct information, we will need to vary k_v parametrically in our model studies. That k_v is small near the center of the reseroir is implied from the fact that

saline water is produced from the formation below 6,000 feet and much less saline water from shallower depths (Hoagland and Elders [1977]).

The effective vertical thermal heat conductivity of a horizontal interbedded mixture of shales and sands is given by

$$\kappa_{eff} = \frac{\kappa_{Sand}\,\kappa_{Shale}}{H\kappa_{Shale} + (1-H)\kappa_{Sand}} \qquad (9)$$

where H is the sand fraction. In Layer 2 ($700 < Z < 2{,}500$ feet) where conduction clearly dominates the East Mesa anomaly, the formation is approximately 2/3 shales and 1/3 sands. A good approximation for the water saturated conductivity of sand is $\kappa_{Sand} = 4.67 \times 10^5$ ergs/sec-cm-°C (Ramey, et al. [1974]). This value and the value of $\kappa_{eff} = 1.76 \times 10^5$ ergs/sec-cm-°C suggested by TRW, Equation (4), when substituted into the mixture formula yield $\kappa_{Shale} = 1.34 \times 10^5$ ergs/sec-cm-°C. This value is within the range $(0.8 - 2.1) \times 10^5$ ergs/sec-cm-°C considered reasonable for saturated shales (Ramey, et al. [1974]).

IV. GOVERNING EQUATIONS AND SIMULATORS

Subsurface temperatures in the East Mesa geothermal field are far below the boiling point for local hydrostatic pressure everywhere in the system. Hence, we need not be concerned with two-phase flow either in our model of the natural flow conditions or in any subsequent study of the effects of large scale fluid movements within the geothermal reservoir. Moreover, in such single-phase liquid-dominated systems, pressure equilibrium is attained within a few years at most, whereas the time scale of interest in natural flow simulations is tens of thousands of years. Consequently, the natural flow may be just as accurately treated and the calculations greatly simplified by invoking the Boussinesq approximation. This approximation neglects pressure transient effects; the density of the fluid is assumed to be independent of pressure and depends only upon temperature.

4.1 SINGLE-PHASE BALANCE LAWS

The general equations expressing mass, energy and momentum conservation are as follows for single-phase (liquid) flow in a porous medium:

Mass Balance

$$\frac{\partial}{\partial t}(\phi\rho_\ell) + \nabla \cdot (\phi\rho_\ell \vec{u}_\ell) = \dot{m}_{IN} - \dot{m}_{OUT} \qquad (10)$$

Energy Balance

$$\frac{\partial}{\partial t}[(1-\phi)\rho_r E_r + \phi\rho_\ell E_\ell] + \nabla \cdot (\phi\rho_\ell E_\ell \vec{u}_\ell) = \dot{m}_{IN} E_{IN} - \dot{m}_{OUT} E_\ell + \dot{e}_o + \dot{e}'T + \nabla \cdot (\kappa_m \nabla T) \qquad (11)$$

Momentum Balance (Darcy's Law)

$$\phi \rho_\ell \vec{u} = \frac{k}{\nu} (\rho \vec{g}_\ell - \nabla P) \qquad (12)$$

In these expressions,

ϕ = rock formation porosity

k = rock formation permeability

ρ_ℓ = fluid density

ρ_r = rock grain density

E_ℓ = fluid internal energy per unit mass

E_r = rock internal energy per unit mass

ν = fluid kinematic viscosity (μ/ρ)

$\vec{g}$ = gravity acceleration

P = fluid pressure

$\vec{u}$ = fluid velocity

κ_m = bulk effective thermal conductivity

T = temperature (same for fluid and rock)

$\dot{m}_{IN}$ = fluid mass source rate (mass per volume per time)

$\dot{m}_{OUT}$ = fluid mass sink rate (mass per volume per time)

E_{IN} = fluid internal energy associated with $\dot{m}_{IN}$

$\dot{e}_o + \dot{e}'T$ = energy source/sink rate (power per volume); a linear function of temperature

In the energy equation, the effects of pressure-work and viscous dissipation have been ignored; they may be shown to be negligible for single phase liquid flow.

We now assume that the rock is rigid and undeformable, so that ϕ, ρ_r and k are functions of position only. We further assume that the internal energies of both the fluid and the rock are proportional to temperature:

$$E_r = C_r T \tag{13}$$

$$E = C_\ell T \tag{14}$$

where C_ℓ is a simple constant and C_r depends only upon position. Thus, the energy equation may be rewritten as:

$$\left[(1-\phi)\rho_r C_r + \phi\rho_\ell C_\ell\right] \frac{\partial T}{\partial t} + \phi C_\ell T \frac{\partial \rho_\ell}{\partial t}$$

$$+ C_\ell \nabla \cdot (\phi\rho_\ell T \vec{u})$$

$$= C_\ell (\dot{m}_{IN} T_{IN} - \dot{m}_{OUT} T)$$

$$+ \dot{e}_o + \dot{e}' T + \nabla \cdot (\kappa_m \nabla T) \tag{15}$$

4.2 THE BOUSSINESQ APPROXIMATION

Next, we assume that, since liquids are relatively incompressible, the fluid density may be regarded as a function of temperature only:

$$\rho_\ell = \rho_0 - \alpha T - \beta T^2 \tag{16}$$

where ρ_0, α and β are constants. If we substitute this expression into Darcy's law (Eq. 12), we obtain:

$$\phi\rho_\ell \vec{u} = \frac{k}{\nu} (\rho_0 \vec{g} - \alpha T \vec{g} - \beta T^2 \vec{g} - \nabla P) \tag{17}$$

We define the "reduced pressure" by:

$$\nabla\psi = \nabla P - \rho_0 \vec{g} \tag{18}$$

so that (17) becomes:

$$\phi \rho_\ell \vec{u} = - \frac{k}{\nu} (\alpha T \vec{g} + \beta T^2 \vec{g} + \nabla \psi) \qquad (19)$$

Finally, in the remaining equations, we make the approximation $\rho \simeq \rho_0$. Substituting Equation (19) into the resulting equations yields:

Mass Balance

$$\nabla \cdot [\frac{k}{\nu} \nabla \psi] + \nabla \cdot [\frac{k}{\nu} \vec{g} (\alpha T + \beta T^2)] + \dot{m}_{IN} - \dot{m}_{OUT} = 0 \qquad (20)$$

Energy Balance

$$[(1-\phi)\rho_r C_r + \phi \rho_0 C_\ell] \frac{\partial T}{\partial t} + C_\ell \nabla \cdot (T \vec{U})$$

$$= C_\ell \dot{m}_{IN} T_{IN} + \dot{e}_0 + T(\dot{e}' - C_\ell \dot{m}_{OUT})$$

$$+ \nabla \cdot (\kappa_m \nabla T) \qquad (21)$$

where

$$\vec{U} \equiv - \frac{k}{\nu} (\nabla \psi + \vec{g}(\alpha T + \beta T^2)) \qquad (22)$$

These comprise two equations in two unknowns (ψ, T), and can be solved given proper initial and boundary conditions and an adequate constitutive description. The constitutive description amounts to the spatial distributions of the rock properties (ρ_r, C_r, ϕ, k), values for the fluid constants (ρ_0, α, β, C_ℓ) and prescriptions for the quantities ν and κ_m.

The required bulk thermal conductivity (κ_m) is adequately approximated using Budiansky's formula which relates κ_m to the separate rock grain (κ_r) and fluid (κ_ℓ) conductivities by

$$\frac{\phi}{2K_m + K_\ell} + \frac{(1-\phi)}{2K_m + K_r} = \frac{1}{3K_m} \qquad (23)$$

The constitutive description, therefore, amounts to the spatial distributions of the rock properties and temperature dependent prescriptions for the fluid properties.

4.3 MUSHRM AND LIGHTS

The single-phase balance equations in Section 4.1 are a special case of the system of balance equations for multi-phase flow (e.g., transport of mixtures of liquids, gases and solid particles through heterogeneous porous media) that are solved by the S^3 MUSHRM (MUlti-Species Hydrothermal Reservoir Model) computer code. MUSHRM is a sophisticated and flexible three-dimensional reservoir simulator that has been used for diverse applications involving geopressured geothermal brine/methane systems and hydrothermal brine/steam systems. The numerical techniques required for treating the fully compressible multi-phase (water, steam, precipitated salts) fluid and heat flow problems are necessarily very complicated. MUSHRM is, therefore, fairly expensive to use in problems where simulations must be carried out for thousands of years in order to attain steady-state solutions for natural flow of heat and mass in hydrothermal systems.

Natural flow simulations in liquid-dominated single-phase hydrothermal systems may be performed just as accurately and costs may be greatly reduced by using the S^3 LIGHTS (Liquid Incompressible Geothermal Heat Transfer Simulator) computer code which invokes the Boussinesq approximation (Pritchett [1979]) as outlined in Section 4.2. LIGHTS is a fully three-dimensional computer program which employs a finite difference method of solution based upon a three-dimensional Cartesian grid (x, y, z)

with variable zone spacing. The simulator permits all practical choices of boundary conditions and arbitrary assignment of distributed mass and heat sources. The simulator also permits the user to specify the reservoir formation properties as functions of position: porosity (ϕ), rock grain density (ρ_r), directional permeabilities (k_x, k_y, k_z), heat capacity (C_r), and rock grain thermal conductivity (κ_r). The essential fluid properties required are the density (ρ_ℓ), heat capacity (C_ℓ), kinematic viscosity (ν) and the thermal conductivity (κ_ℓ).

The fluid heat capacity is assumed to be a simple constant. The other three required fluid properties are considered functions of temperature. For pure water, within the pressure and temperature range of interest at East Mesa, these properties are adequately fitted by the following functions:

$$\rho = \rho_0 - \beta_1 T - \beta_2 T^2 \qquad (24)$$

$$\rho_0 = 1.0048 \text{ g/cm}^3$$

$$\beta_1 = 1.40667 \times 10^{-4} \text{g/cm}^3\text{-°C}$$

$$\beta_2 = 2.774222 \times 10^{-6} \text{g/cm}^3(\text{°C})^2$$

$$\nu = 1/\lambda \quad (\lambda = \lambda_0 + \lambda_1 T + \lambda_2 T^2 + \lambda_3 T^3) \qquad (25)$$

$$\lambda_0 = 57.5 \text{ sec/cm}^2$$

$$\lambda_1 = 1.98734 \text{ sec/cm}^2\text{-°C}$$

$$\lambda_2 = 1.17599 \times 10^{-2} \text{ sec/cm}^2\text{-(°C)}^2$$

$$\lambda_3 = -3.4133 \times 10^{-5} \text{ sec/cm}^2\text{-(°C)}^3$$

$$\kappa = \kappa_0 + \kappa_1 T + \kappa_2 T^2 \qquad (26)$$

κ_0 = 57,700 erg/sec-cm-°C

κ_1 = 164.533 erg/sec-cm(°C)^2

κ_2 = -0.581333 erg/sec-cm-(°C)^3

V. AXISYMMETRIC MODEL

5.1 MUSHRM CALCULATIONS

From the outset it was planned to use a computer-based simulator to synthesize the pertinent geothermal and geohydrological data base for the East Mesa hydrothermal system into a fully three-dimensional model. Because of the incompleteness of the data, however, a sequence of axisymmetric calculations was first performed to quantitatively investigate various aspects of the conceptual model and the effects of uncertainties in the input data. A basic goal of these calculations was to predict the surface heat flow and to compute subsurface temperature distributions that match the axisymmetric approximations to the data. Obtaining such a solution involves parametric calculations to obtain appropriate initial and boundary conditions for the model that are consistent with the available data (within the axisymmetric constraint).

The surface heat flow and subsurface temperature and porosity distributions constructed for such an axisymmetric approximation are shown on the radial section presented in Figure 20. The axis of the section is considered to penetrate the center of the geothermal anomaly near the Mesa wells 6-1 and 6-2. The region treated is depicted by the circular surface area shown in Figure 6. The axisymmetric approximations to the data are reasonably good near the center of the anomaly. The model is incapable of representing the directional variations in the formation porosity and permeability of the horizontal layers but radial variations are included in Figure 20 so that the general effect of lateral variations could be examined in the axisymmetric calculations.

The axisymmetric model assumes that a cylindrically fractured region (e.g., in the vicinity of intersecting faults such as are shown in Figure 7 and 8 through 10) channels hot geothermal fluid

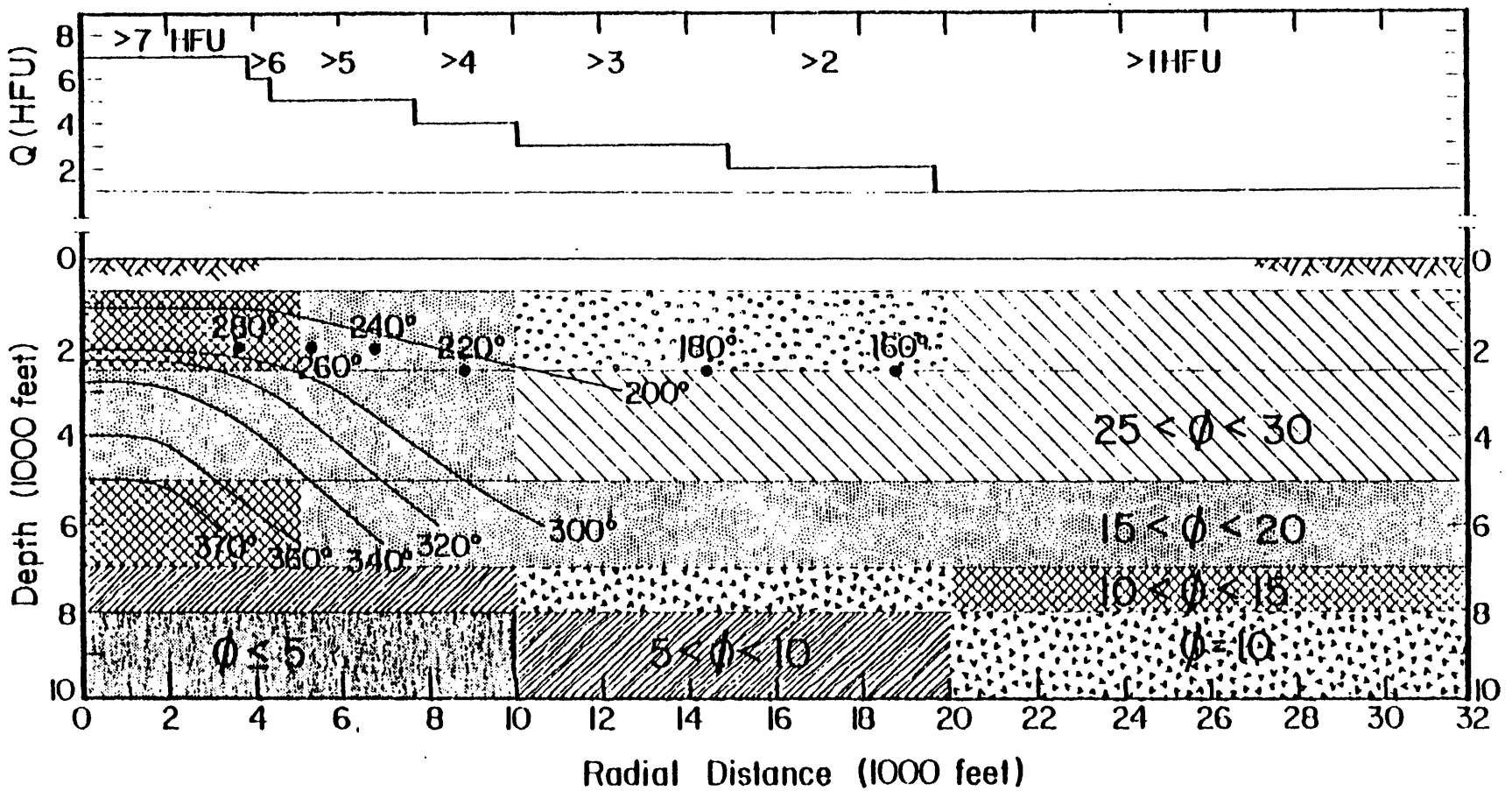

Figure 20. Distributions of subsurface temperature (°F), surface heat flow, and formation porosity in idealized axisymmetric model. Center of radial section is considered to be located at origin, asterisk in Figure 6, of project study area.

from deep within the basement rock, through the nearly impermeable overlying shale-rich sedimentary sequence, and into the higher permeability sand-shale sequence that comprises the reservoir. Much of the hot fluid is shunted radially outward as it rises within the reservoir. The geothermal cap prevents any of the hot fluid from reaching the surface. Other than the hot fluid source, the only other location where fluid may enter or leave the reservoir is at the outer cylindrical boundary where the pressure distribution is assumed to be hydrostatic.

During the initial months of the research, S^3's general purpose MUSHRM geothermal reservoir simulator (Garg, et al., [1977]) was employed in a series of parametric calculations for the axi-symmetric model of the East Mesa hydrothermal system. These results have been summarized in a paper (Riney, et al., [1979]). It was found that a large convective loop is always produced that is driven by two mechanisms:

(1) the rising hot fluid from the convective source which flows radially outward beneath the overlying cap rock, and (2) the recharge by colder (and denser) fluid from the outer boundary which flows radially inward at the bottom of the modeled region. The parametric MUSHRM calculations demonstrated that to control the convective loop and produce the balance between heat conduction and heat convection implied by the approximated East Mesa subsurface temperatures (Figure 20), the vertical formation permeability must be on the order of $k_v \sim 0.3$ to ~ 0.5 md. The model that finally evolved is not unique but, at East Mesa, there is sufficient information available that the range of parameters that give an adequate solution is reasonably limited.

The conclusion that the effective formation vertical permeability in the East Mesa hydrothermal system is small appears to be on firm ground. The University of Colorado researchers have neglected vertical permeability altogether in their analytical studies of the geothermal reservoir (Kassoy and Zebib [1978]).

5.2 LIGHTS CALCULATIONS

The three-dimensional Cartesian LIGHTS program was first used for calculations analogous to the axisymmetric MUSHRM calculations. The horizontal cross-section of the cylindrical region treated earlier was a circle of radius R = 10.47 km (Figure 6), whereas the cross-section of the region treated in the LIGHTS calculations was an equal area square with sides of length $X = \sqrt{\pi R^2} = 18.6$ km. Figure 21 illustrates horizontal (x, y) and vertical (y, z) views of the finite difference grid employed for the half of the corresponding region treated in the three-dimensional LIGHTS calculation.

As with the earlier axisymmetric MUSHRM calculations, the grid extends vertically from a depth of 1,500 feet at the top to a depth of 8,000 feet at the bottom. The surface heat loss is assumed equal to the conductive heat flow through the geothermal cap and other strata above the 2,000 feet horizon which is represented by a distributed heat sink in layer k=5 (1,500 ft < depth < 2,500 feet) given by

$$Q_{ij} = 2.79\ (T_{ij5} - T_S)\ \text{ergs/cm}^2\text{-sec}, \qquad (27)$$

$$T_S = 29.44^{\circ}\text{C}\ (85^{\circ}\text{F})$$

T_S corresponds to the value of the surface temperature extrapolated from shallow-hole heat flow measurements (see Section 3.1). The coefficient 2.79 is calculated to correspond to a temperature Of 142°C measured at 2,000 feet depth in the Mesa 6-2 well where the surface heat flux Q ~ 7.5 HFU (Riney, et al. [1979a]).

The total convective mass influx rate, M_c, is assumed to enter at the center of the bottom layer of the region modeled. In the half of the region treated in the LIGHTS calculation (Figure

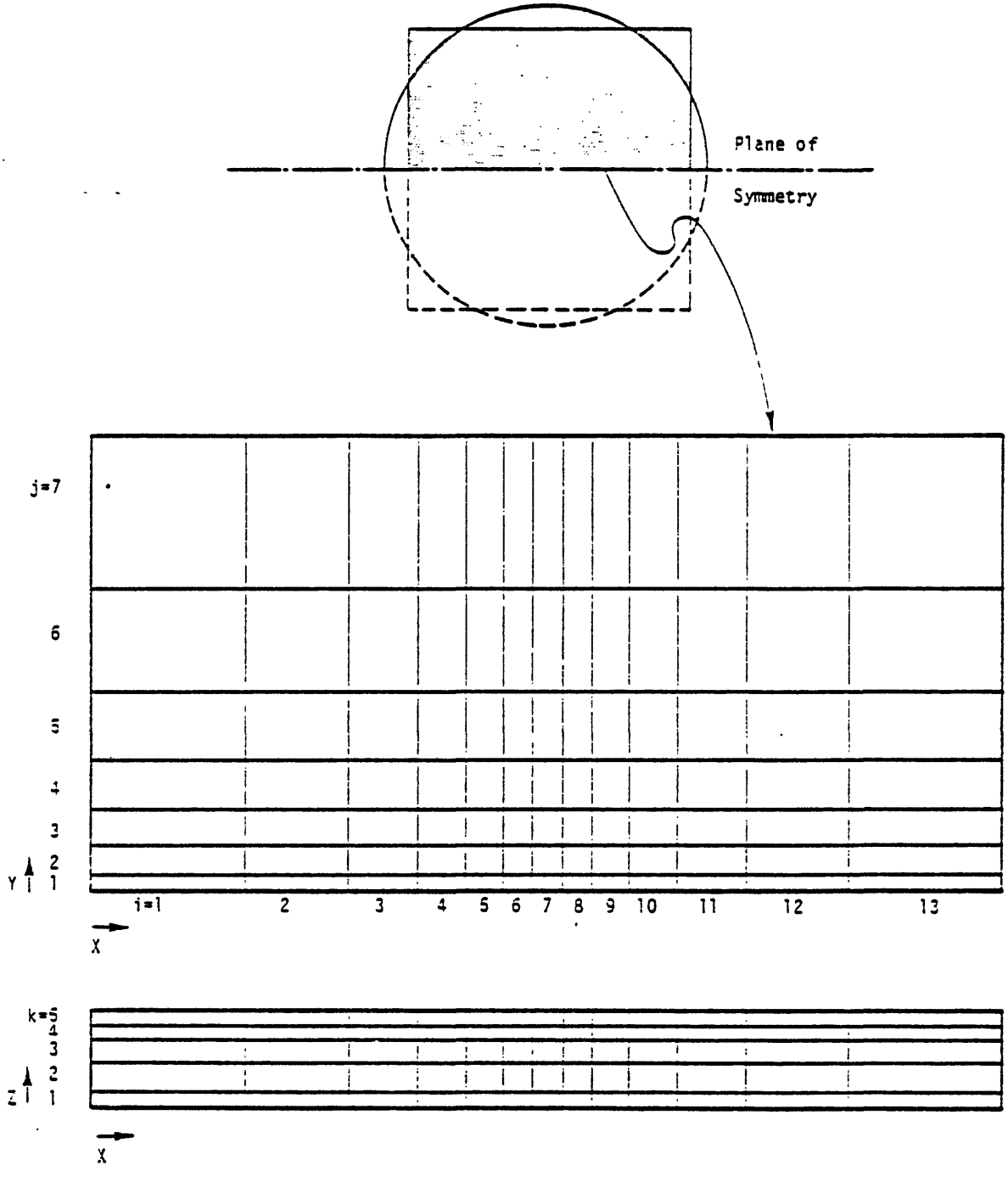

Figure 21. Cartesian grid employed in three-dimensional LIGHTS calculation.

21), this mass flux is represented as an internal source of magnitude $\dot{M}_C/2$ entering zone (i=7, j=1, k=1); the temperature of the fluid as it enters the reservoir is assumed to be T_C = 196.11°C (385°F). There is no other fluid exchange across the bottom surface and the temperature distribution (T_B) at this impermeable boundary is fixed at values estimated from Figure 20. The axisymmetric approximation used for T_B is shown in Figure 22. The outer boundaries are maintained at prescribed hydrostatic pressure (values computed from each zones' depth, with fluid density corrected for a temperature gradient corresponding to Q = 1 H.F.U.) throughout the calculations; the net outward flow at the periphery must, therefore, match the convective mass influx rate.

The assumption that the enthalpy of the fluid entering the bottom of the reservoir less the enthalpy of the fluid leaving at the periphery is balanced by the surface heat flux in excess of the normal geothermal gradient leads to an approximation for the convective source ($\dot{M}_C$ = 16.9 kg/sec). This assumption neglects the additional conductive heat transfer across the bottom boundary due to the elevated temperature distribution (T_B) imposed there and hence it overestimates $\dot{M}_C$ somewhat.

The foregoing input data duplicated that assumed in the earlier MUSHRM calculations to the extent possible with a rectangular rather than a cylindrical grid. The MUSHRM calculations demonstrated that a vertical formation permeability of the order of $k_v \sim 0.3$ to 0.5 md was required for a reasonable match of the axisymmetric approximations to the heat flow and temperature data shown in Figure 20. The MUSHRM calculations also demonstrated that the results were fairly insensitive to variations of the formation porosity (ϕ) and horizontal permeability (k_h) outside the vicinity of the hot spot. Consequently, the LIGHTS calculations employed the following values which are based on data near the hot spot:

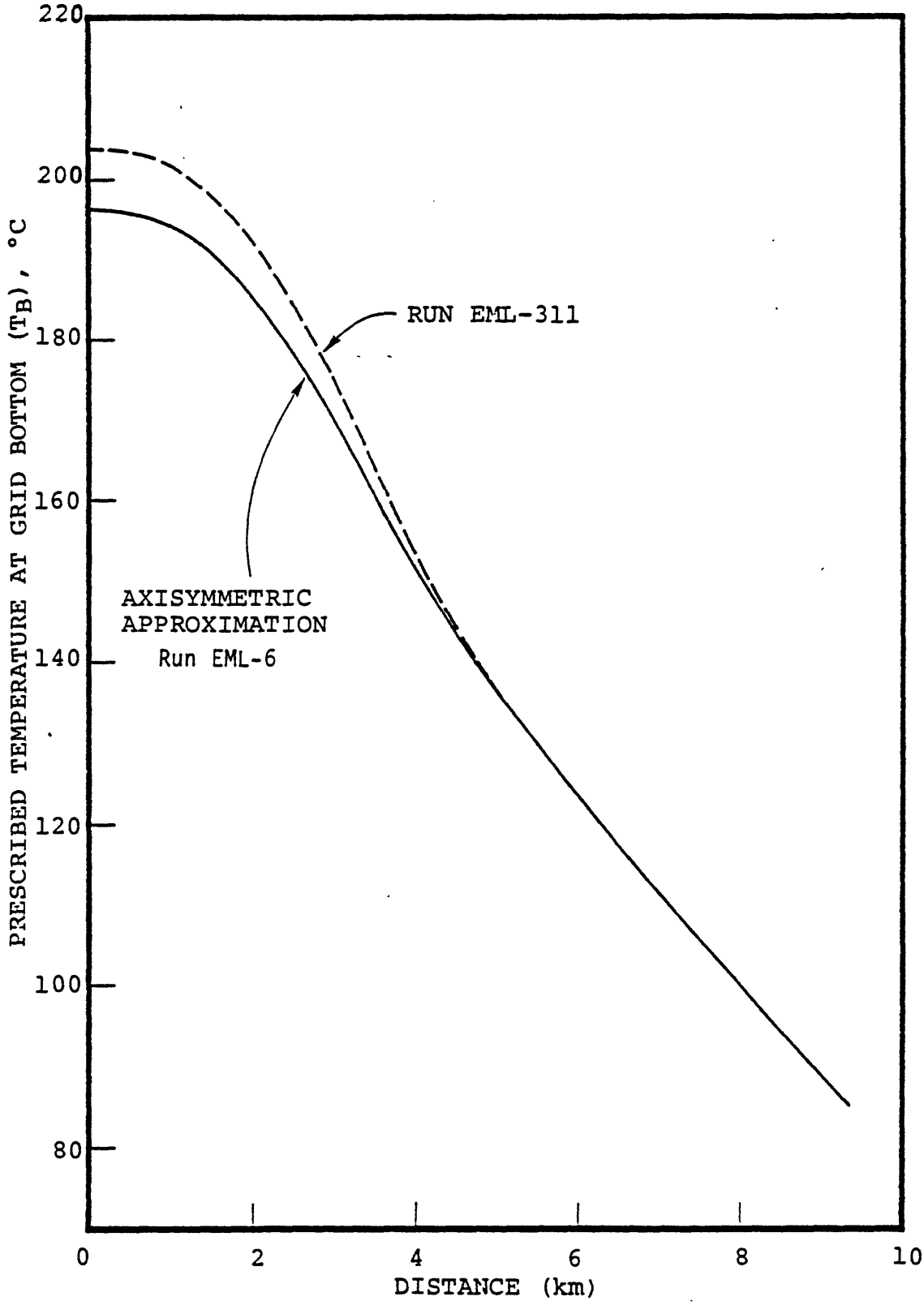

Figure 22. Prescribed temperature distribution at bottom of finite difference grid (depth of 8,000 feet).

Layer; k= ...	Depth (ft)	ϕ	k_h (md)
5	1500-2500	0.125	20
4	2500-3500	0.175	90
3	3500-5000	0.175	90
2	5000-7000	0.125	20
1	7000-8000	0.075	4

The following values for the required formation properties were used throughout the region treated:

Rock grain density, ρ_r = 2.65 gm/cm^3
Rock heat capacity, C_r = 10^7 ergs/cm-°C
Rock grain thermal conductivity, κ_r = 1.97×10^5 ergs/gm-°C

The liquid heat capacity was $C_\ell = 4.2 \times 10^7$ erg/gm-°C and the temperature dependence of the other required liquid properties (ρ_ℓ, ν and κ_ℓ) were computed from Equations (24) through (26).

These input data essentially duplicate those used in the prior MUSHRM calculations. We note that κ_ℓ in the pressure and temperature range of interest is about 0.65×10^5 ergs/sec-cm-°C; when this value and the selected value for κ_r are substituted into Equation (23), the effective bulk (formation) thermal conductivity is calculated to be $\kappa_m = 1.76 \times 10^5$ ergs/sec-cm-°C. This is consistent with the effective formation conductivity used by TRW (Equation (4)).

The first LIGHTS calculation (Run EML-1) assumed k_v = 0.5 md throughout the region and used the convective mass source estimate of M_C = 16.9 kg/sec; the calculation essentially corresponds to the earlier Bx-11 MUSHRM calculation (Riney, et al. [1979a]). Because of the much faster computation speed of LIGHTS, however, it was practical to carry the calculation to 115,200 years whereas the

MUSHRM calculations were typically carried out to the order of 3,000 to 15,000 years in time. The shorter time sufficies for convective equilibrium but is not long enough to allow conductive equilibrium; the MUSHRM calculations do not represent the true steady-state solution (We do not, of course, know if the present natural flow of heat and mass in the East Mesa system is truly in a steady-state situation.) The steady-state surface heat flow calculated in Run EML-1 was too large and the radial distribution too flat to match the axisymmetric approximation to the data.

Several additional LIGHTS calculations were made in which the values of M_C and k_v were varied. A satisfactory match to the axisymmetric approximation to the data was obtained in Run EML-6 by setting

$$\dot{M}_C = 10.0 \text{ kg/sec } (T_C = 196.11^{\circ}C) \qquad (28)$$

and by imposing a radial variation in the value for k_v. The vertical permeability in the reservoir was assumed to vary from 0.5 md at the axis of the hot spot to 0.25 md according to the distribution shown in Figure 23. The physical rationale, of course, was that presumably the convective mass source is associated with vertical fractures, and, therefore, the effective vertical permeability in the vicinity of the mass source should be somewhat higher than elsewhere in the field. The calculation was carried out to 256,000 years to ensure steady-state conditions. The temperature and velocity fields that evolved are shown in Figure 24. The region mimiced by imposition of the heat sink in Equation (27) is shown for reference purposes. The calculated surface heat flow distribution is compared with the axisymmetric approximation to the data in Figure 24a.

Figure 25 presents the temperature-depth profiles calculated with LIGHTS using this axisymmetric model (Run EML-6). The shape of

the contours reflects the balance between the convective and conductive components of the heat transfer at the indicated distance from the axis of the hot spot. Near the axis the steepness of the profile at depth indicates the importance of convection there whereas heat transfer by conduction predominates near the surface. As the distance from the axis of symmetry increases, the importance of convection diminishes even at depth. At large radial distances, heating is primarily due to the hot fluid which is shunted radially outward along the base of the cap rock as shown in Figure 24 by the velocity vectors in the top two layers. The essentially bilinear shape of the profiles at large distance results from the heat transfer by conduction between this hot horizontal stratum and the cooler surfaces at the top and bottom boundaries. This result is in agreement with the interpretation presented by Urban, et al. [1978] for the equilibrium temperature-depth data from East Mesa wells.

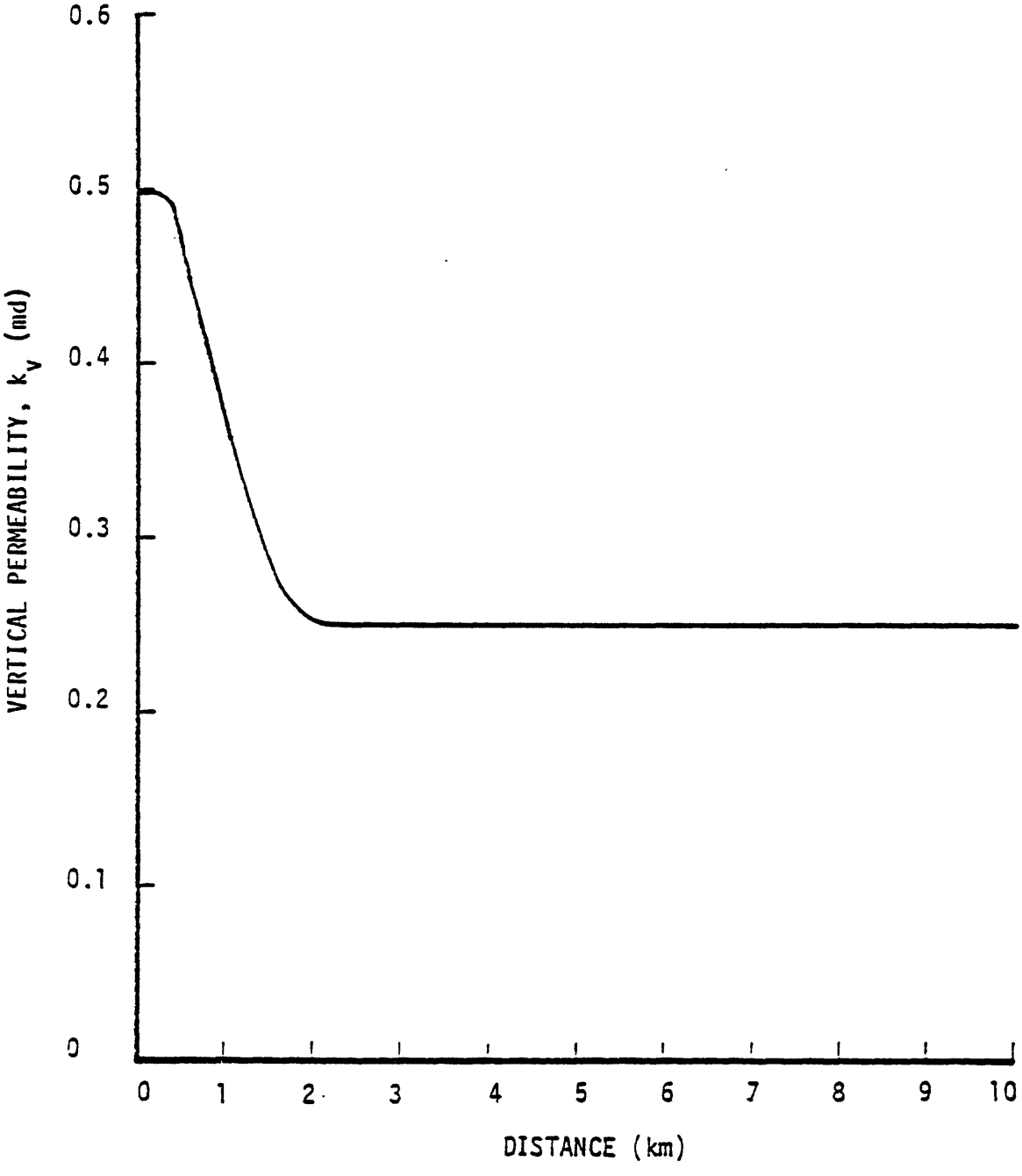

Figure 23. Variation of vertical permeability with distance.

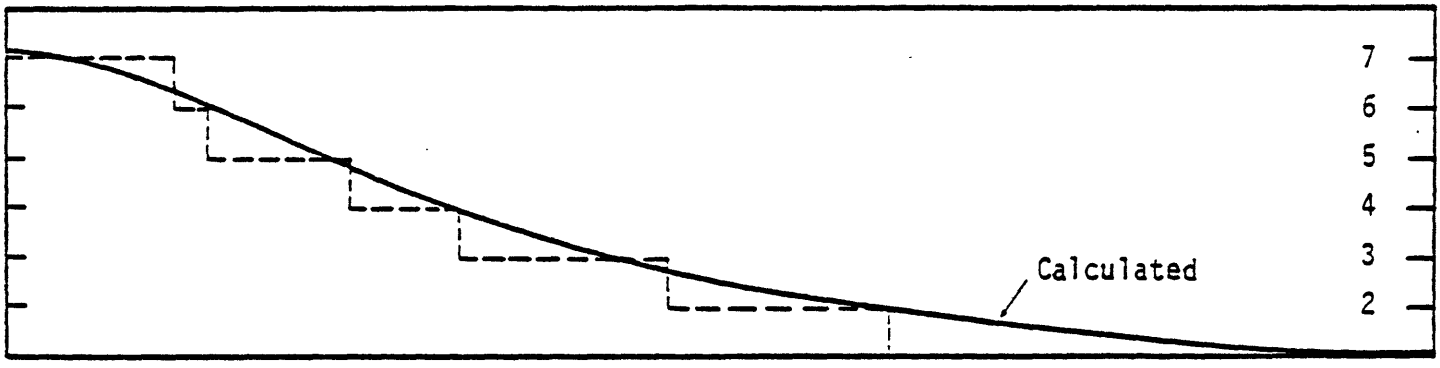

(a) Surface Heat Flow, H.F.U.

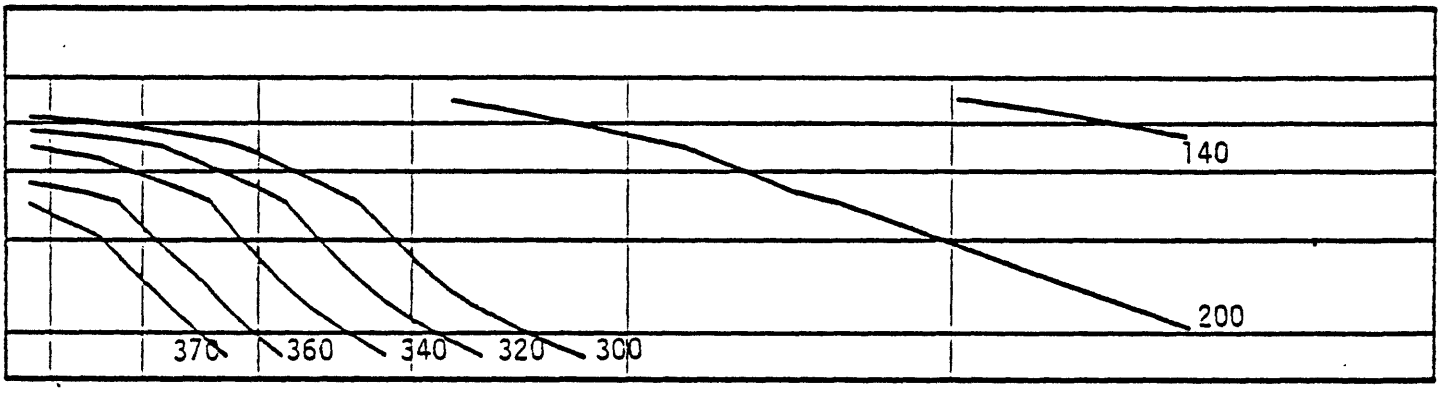

(b) Temperature Field, °F

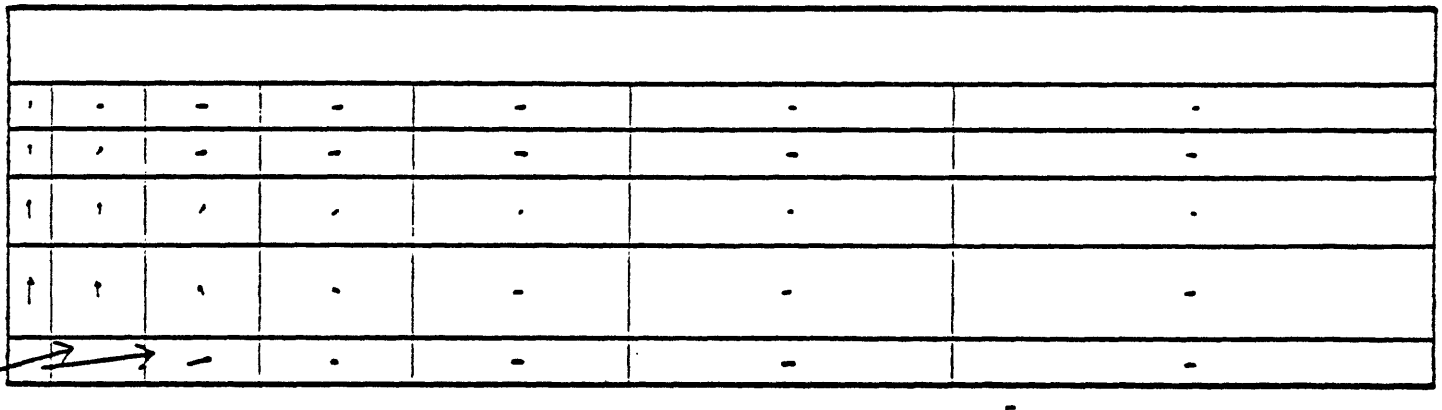

(c) Velocity Field, longest vector corresponds to 1.08×10^{-5} cm/sec.

Figure 24. Steady-state velocity and temperature fields for LIGHTS Run EML-6 (section along yz-plane). Simulated heat flow at surface is compared with axisymmetric approximation to data in (a).

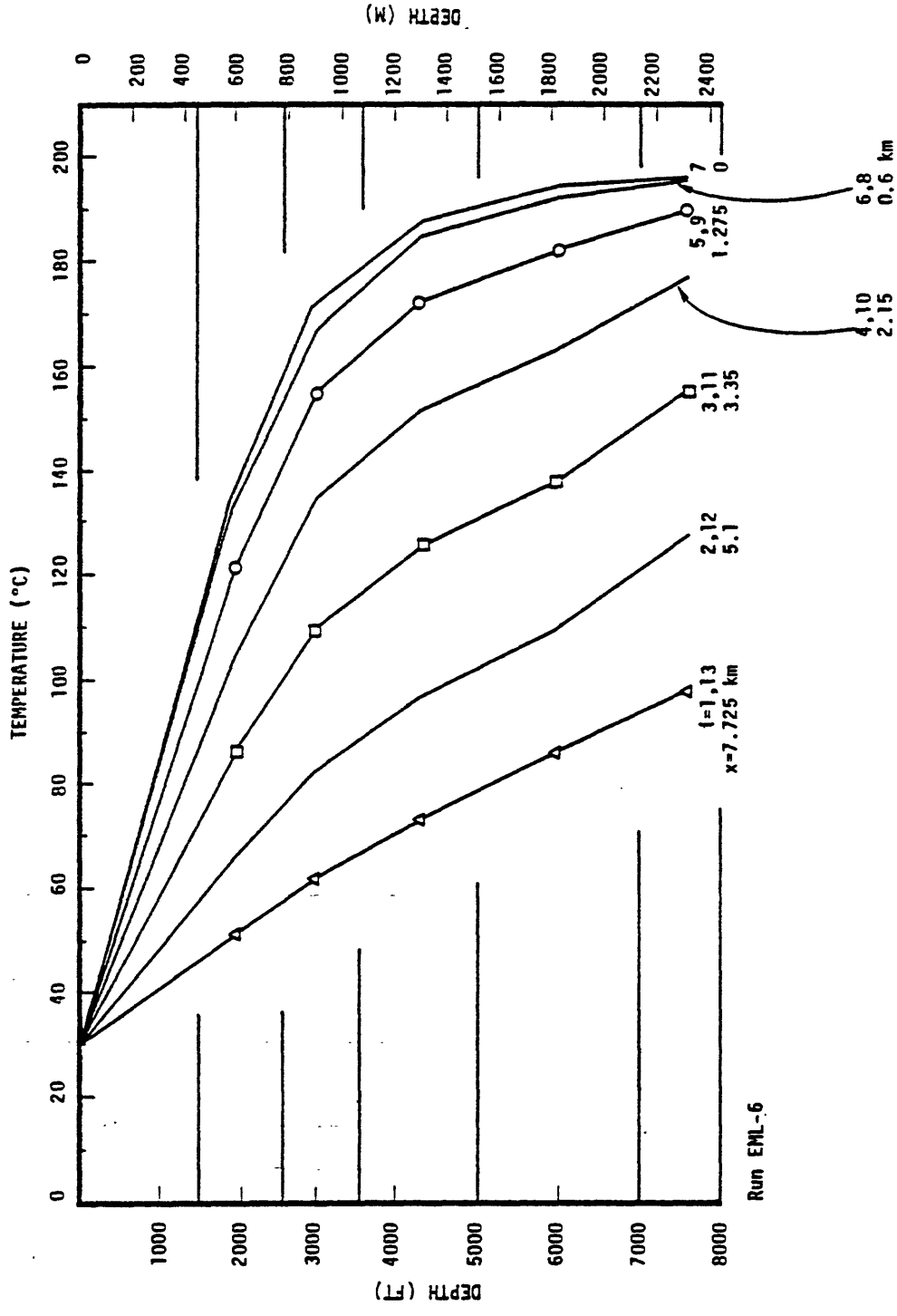

Figure 25. Steady-state temperature-depth profiles at indicated distance from convective source for Run EML-6 (section along xz-plane).

VI. EXPLORATORY THREE-DIMENSIONAL SIMULATIONS

The surface heat flow contours estimated from shallow borehole data (Figure 12) show two distinct lobes which represent major deviations from the axisymmetric approximation to the data. There are various mechanisms which might operate in the deep hydrothermal system to produce distortions of this kind. The pressure of a substantial lateral pressure gradient in the deep system analogous to the regional shallow groundwater pressure gradient shown in Figure 6 could explain deviations from axial symmetry. The lobes may be related to geologic structure. Numerous faults are present in the East Mesa and the center of the geothermal anomaly lies on a complex geological structure (Figures 8 through 11). The LIGHTS computer program has been used to examine the effects of each of these mechanisms; the results are given in this section.

Lateral variations of formation properties are not included in these exploratory calculations so that the effects of each mechanism may be examined individually as a perturbation on the axisymmetric model. The effects of lateral variation in ϕ and k_h are considered in Section VII.

6.1 EFFECT OF REGIONAL LATERAL FLOW

If the shallow and deep hydrothermal systems were in hydrostatic equilibrium with a uniform temperature/depth relation, the water table difference of 72 feet (~ 2.15 bars) across the circular area in Figure 6 would imply a corresponding pressure gradient (dp/dx - 1.156 dynes/cm^3) in the geothermal system. The actual magnitude of the deep lateral pressure gradient is probably much less than this and its direction is unknown. Nevertheless, the first calculation to assess the effect of lateral flow (Run EML-101) was made using this value, oriented along the x-axis of the grid in Figure 21, to perturb the axisymmetric model; the input data were otherwise identical to Run EML-6. A second calculation (Run

EML-102) was then made in which the pressure gradient along the x-axis was reduced to less than half that value (dp/dx = 0.5 dynes/cm^3).

First, the results for Run EML-6 (dp/dx = 0) are shown in Figure 26 in a form more convenient for comparison than Figure 24. The heat flow distribution at the surface for this axisymmetric case is shown in areal view (Figure 26(a)) and the temperature and velocity fields are shown on a vertical section parallel to the direction in which a pressure gradient is to be introduced (the vertical grid layer adjacent to the x-z-plane of symmetry). Figures 27 and 28 show the corresponding steady state solutions obtained in Run EML-102 (dp/dx = 0.5 dynes/cm^3) and Run EML-101 (dp/dx = 1.156 dynes/cm^3). All three runs were for 256,000 years in time.

The results illustrate that the upwelling hot fluid from the convective source at the center of the region is swept downstream to the right by the lateral flow of the cold fluid from the left to right. Comparison of the shape of the temperature contours in Figures 27 and 28 with the shape of those extrapolated from the data (e.g., Figure 17) is instructive. If a lateral pressure gradient plays a major role in causing the observed asymmetry of the temperature in the deeper system, the shape of the isotherms implies that the flow is more likely to be from north-to-south than it is along the direction (DD' in Figure 6) of the shallow groundwater flow. Assuming that the pressure gradient in the deep system is directed north-to-south, its magnitude would certainly appear to be less than dp/dx = 1.156 dynes/cm^3 (Figure 28) since the calculated downstream movement of the contour peaks is much greater than the data extrapolations in Figure 17 would indicate.

Close comparison of Figures 27(b) and 28(b) with Figure 17 revels a qualitative difference between the calculated results and the data fit. The computed isotherms are closer together upstream than they are downstream whereas the observed isotherms are closer together to the south ("downstream") than they are to the north ("up-stream") in Figure 17. This difference is reflected in the

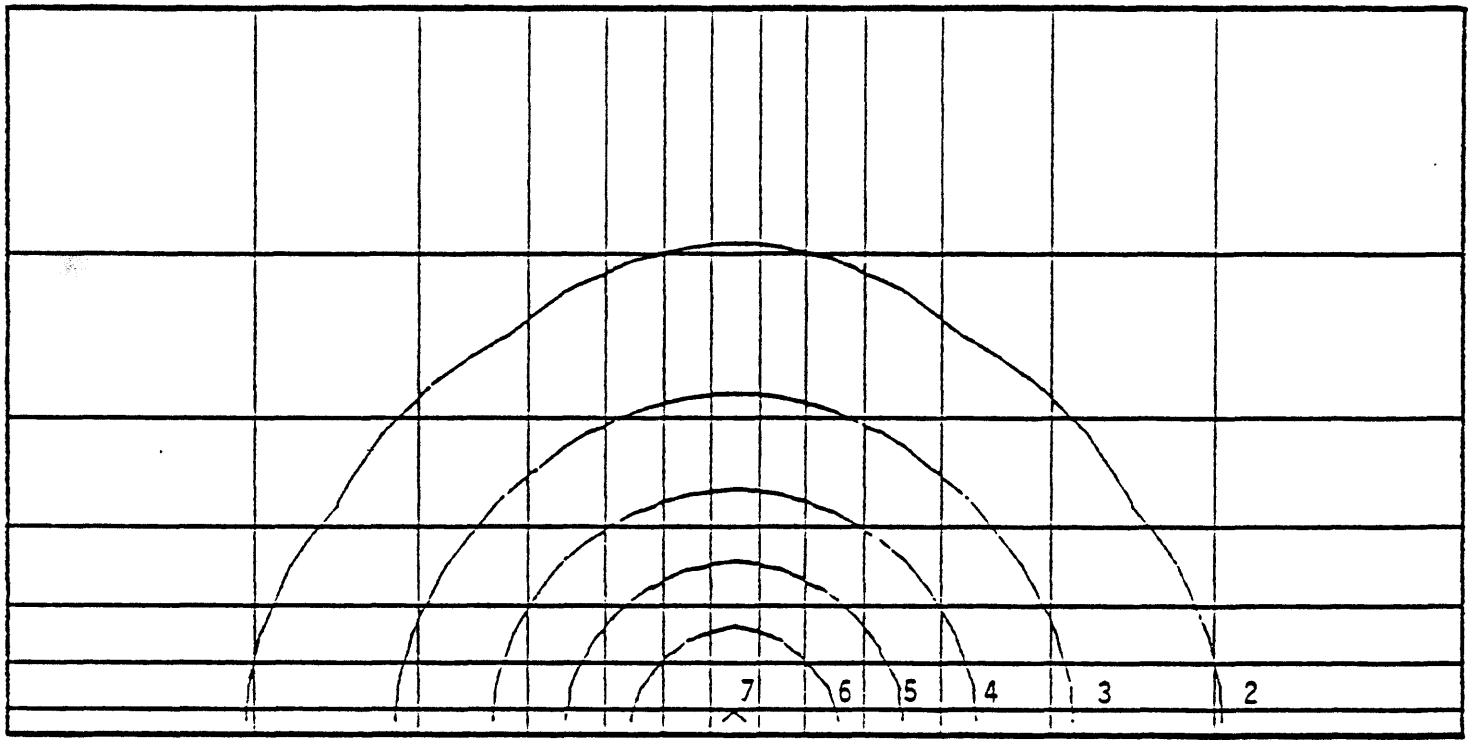

(a) Surface Heat Flow, H.F.U.

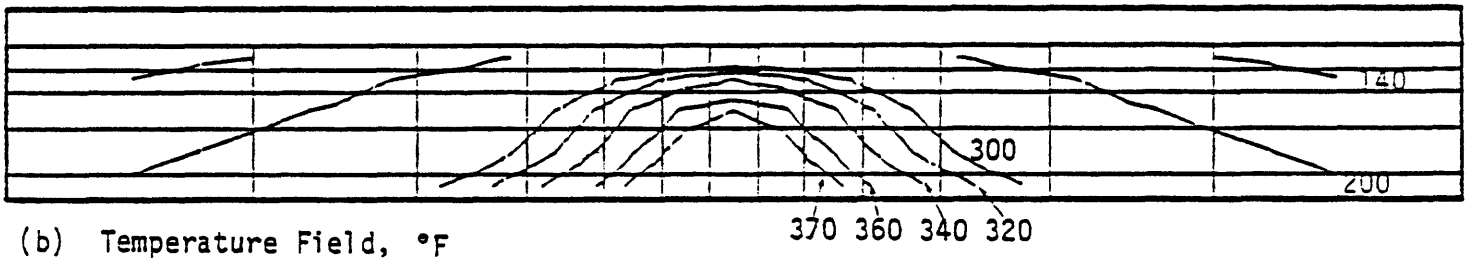

(b) Temperature Field, °F

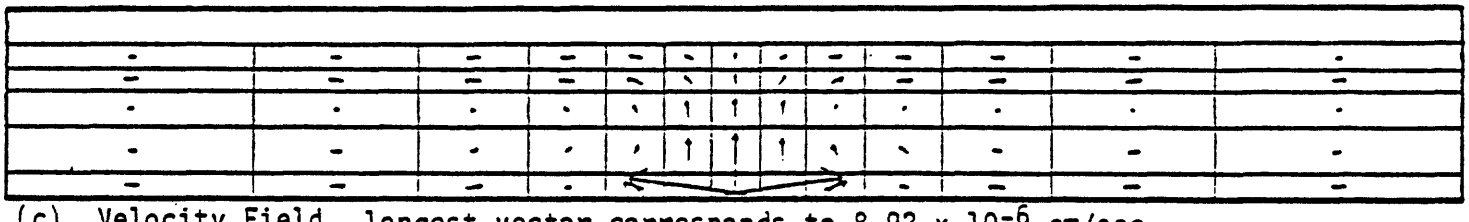

(c) Velocity Field, longest vector corresponds to 8.92×10^{-6} cm/sec

Figure 26. Steady-state conditions for axisymmetric case (Run EML-6; dp/dx = 0).

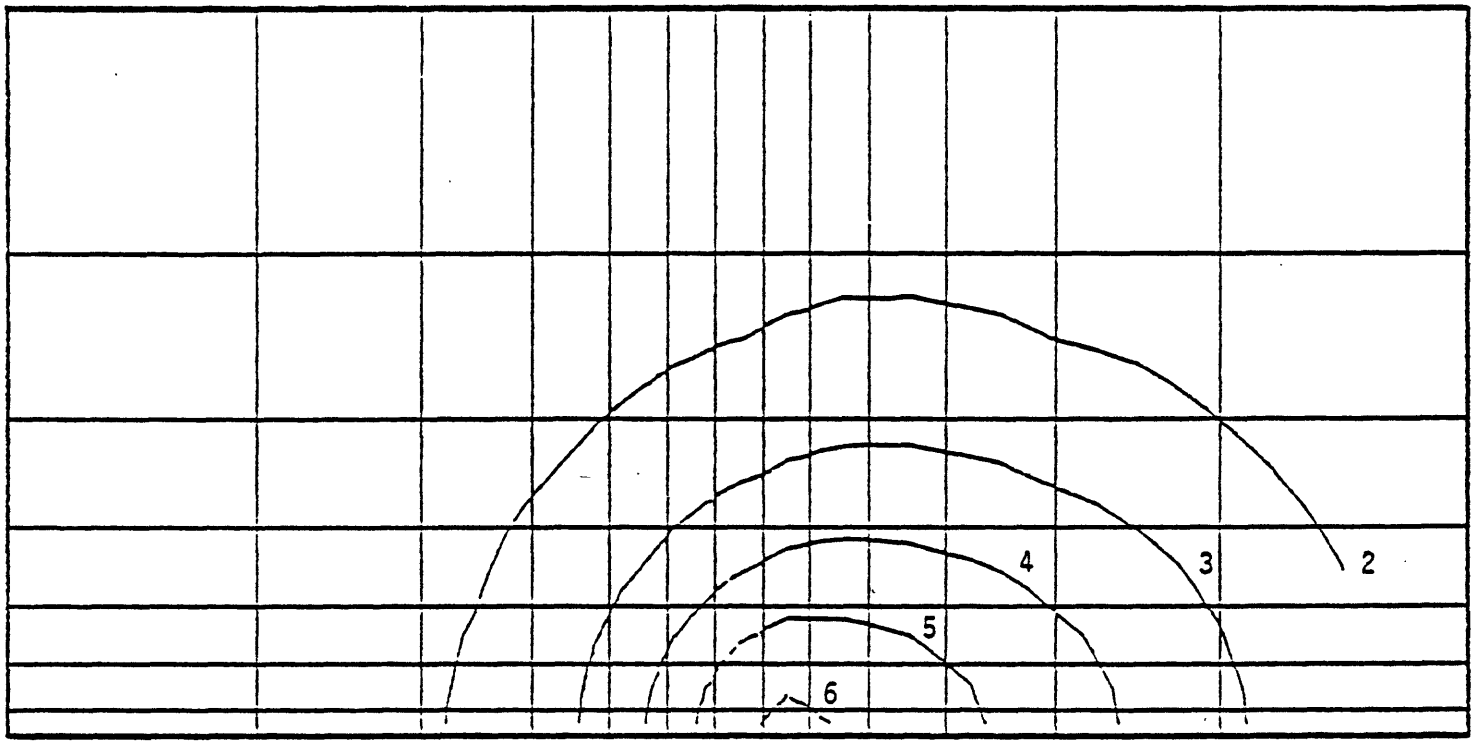

(a) Surface Heat Flow, H.F.U.

(b) Temperature Field, °F

370 360 340 320

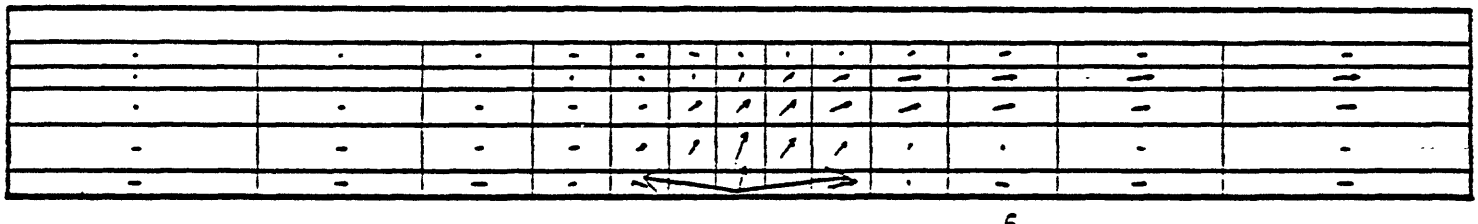

(c) Velocity Field, longest vector corresponds to 9.70×10^{-6} cm/sec

Figure 27. Steady-state conditions for intermediate pressure gradient case (Run EML-102; dp/dx = 0.5 dynes/cm^3).

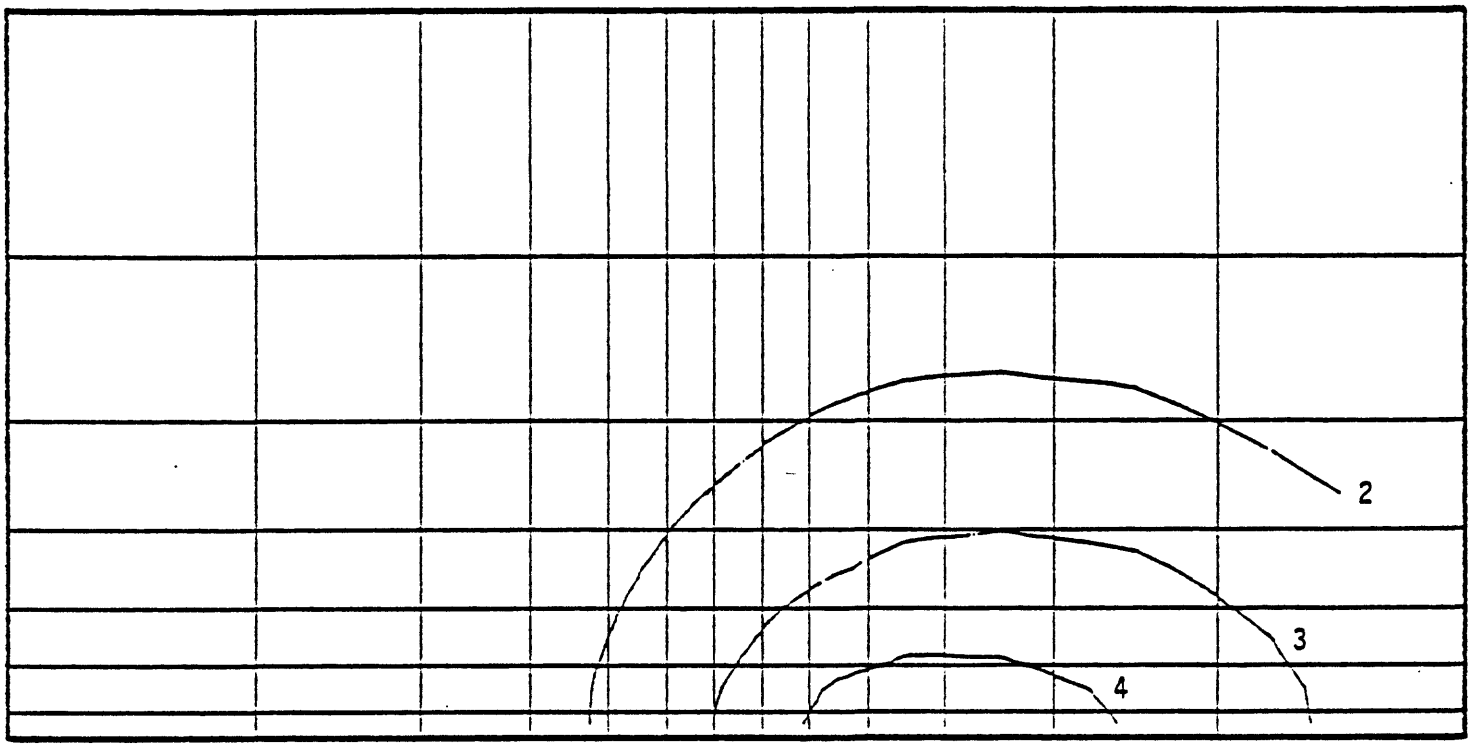

(a) Surface Heat Flow, H.F.U.

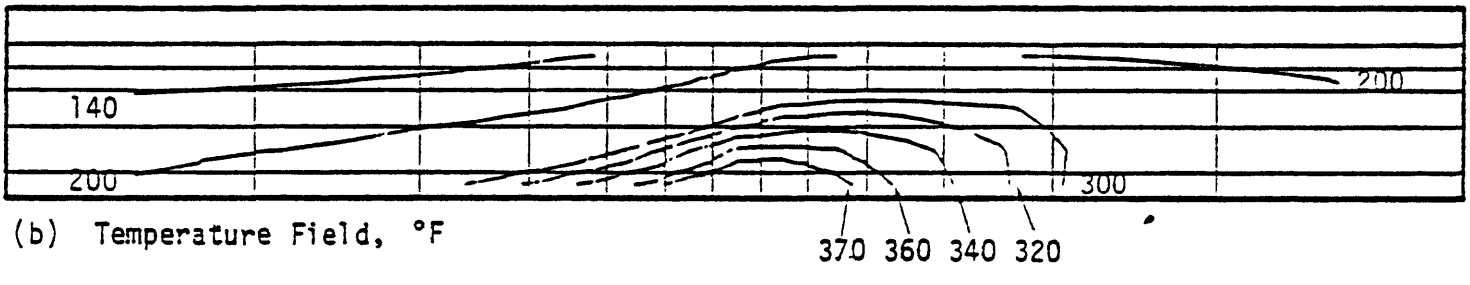

(b) Temperature Field, °F

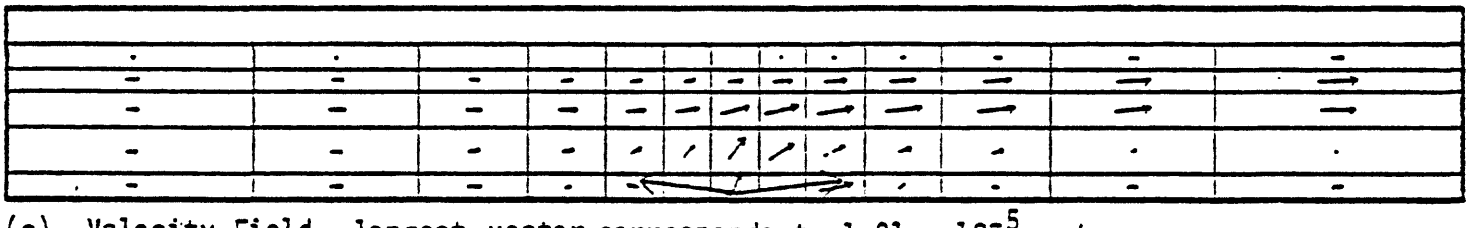

(c) Velocity Field, longest vector corresponds to 1.01×10^{-5} cm/sec

Figure 28. Steady-state conditions for large pressure gradient case (Run EML-101; $dp/dx = 1.156$ dynes/cm^3).

calculated and observed surface heat flow. A regional lateral pressure gradient alone apparently cannot produce the observed directional characteristics of the heat and fluid mass at East Mesa.

6.2 EFFECT OF STRUCTURAL DIP

As discussed in Section 3.1, the intersection of the two mapped fault sets at a depth below the poorly reflective zone occurs south of the Mesa 6-2 and 6-1 wells, towards Magma well 44-7 (see Figures 10 and 11). The upwelling convective fluid is assumed to be channelled upward in the highly fractured intersection zone until it reaches the geothermal cap. The structure contours on the shallowest seismic marker (Figure 8) indicate that the cap is not horizontal; the maximum updip above the presumed center of the convective source is generally to the northeast. Since the axisymmetric calculations were found to be strongly influenced by the hot fluid that was shunted radially outward along the base of the geothermal cap, LIGHTS was employed to examine the effect that structural dip will have on natural flow in a liquid-dominated geothermal system. The first case treated (Run EML-201) represents a constant dip angle α corresponding to the maximum dip of the bottom of the geothermal cap near the center of the East Mesa anomaly as implied by the structural contours ($\alpha = \tan^{-1} 0.038 = 1^{\circ}53'$). The dip is oriented along the x-axis of the grid in Figure 11, thereby perturbing the axisymmetric model; the input data were otherwise identical to Run EML-6 with the exception that the boundary conditions at the bottom and periphery of the grid were adjusted to correspond to the changed depths below the surface.

Figure 29 illustrates the results for Run EML-201. Two additional calculations were made in which the angle of dip was reduced and these results are illustrated in Figure 30 (Run EML-202; $\tan \alpha = 0.0164$; $\alpha = 0^{\circ}56'$) and Figure 31 (Run EML-203; $\tan \alpha = 0.0082$; $\alpha = 0^{\circ}28'$). The upwelling hot fluid from the convective source rises to the base of the cap and then flows

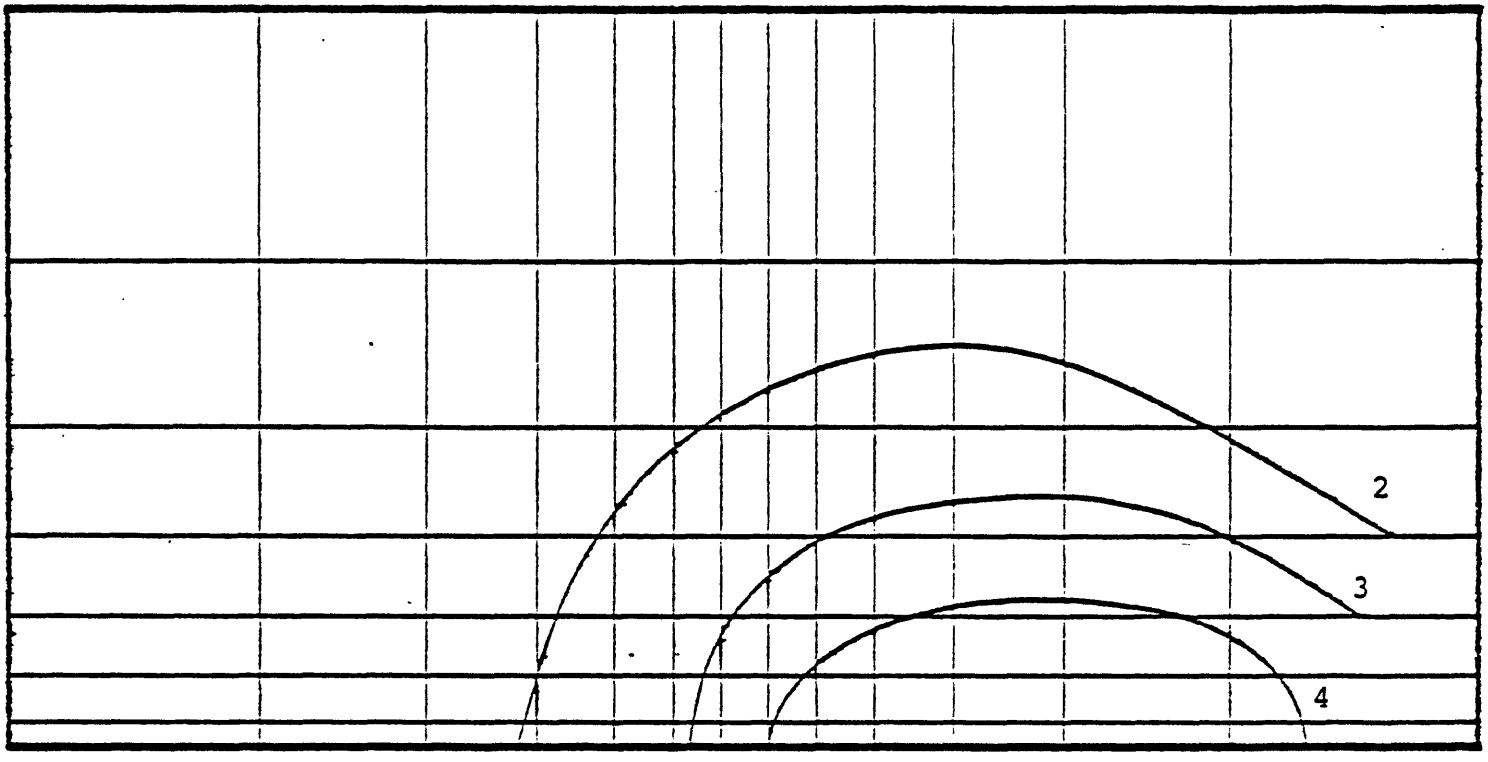

(a) Surface Heat Flow, H.F.U.

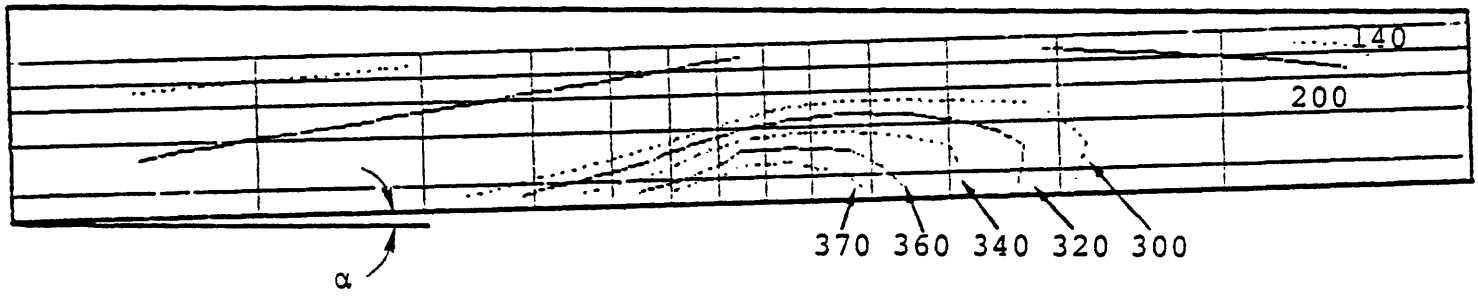

(b) Temperature Field, °F

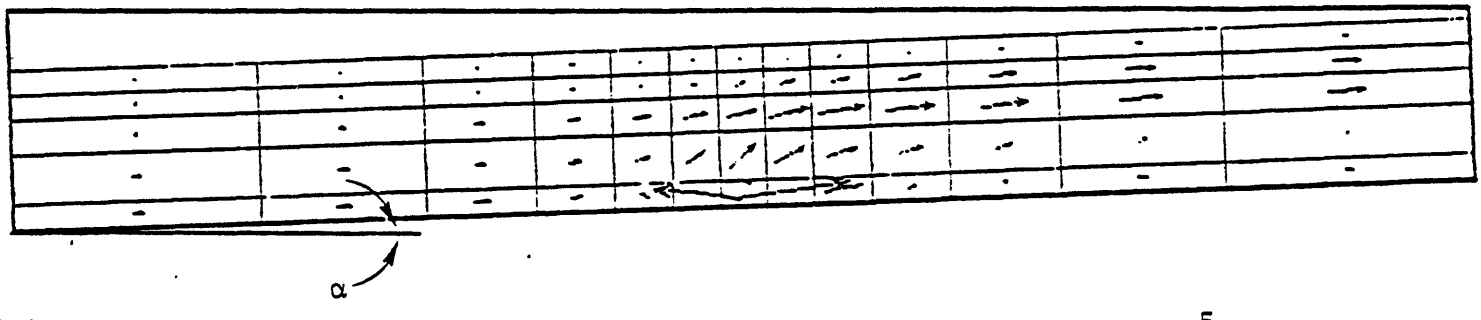

(c) Velocity Field, longest vector corresponds to 1.05×10^{-5} cm/sec

Figure 29. Steady-state conditions for case with axisymmetric source and large structural dip (Run EML-201; tan α = 0.0328).

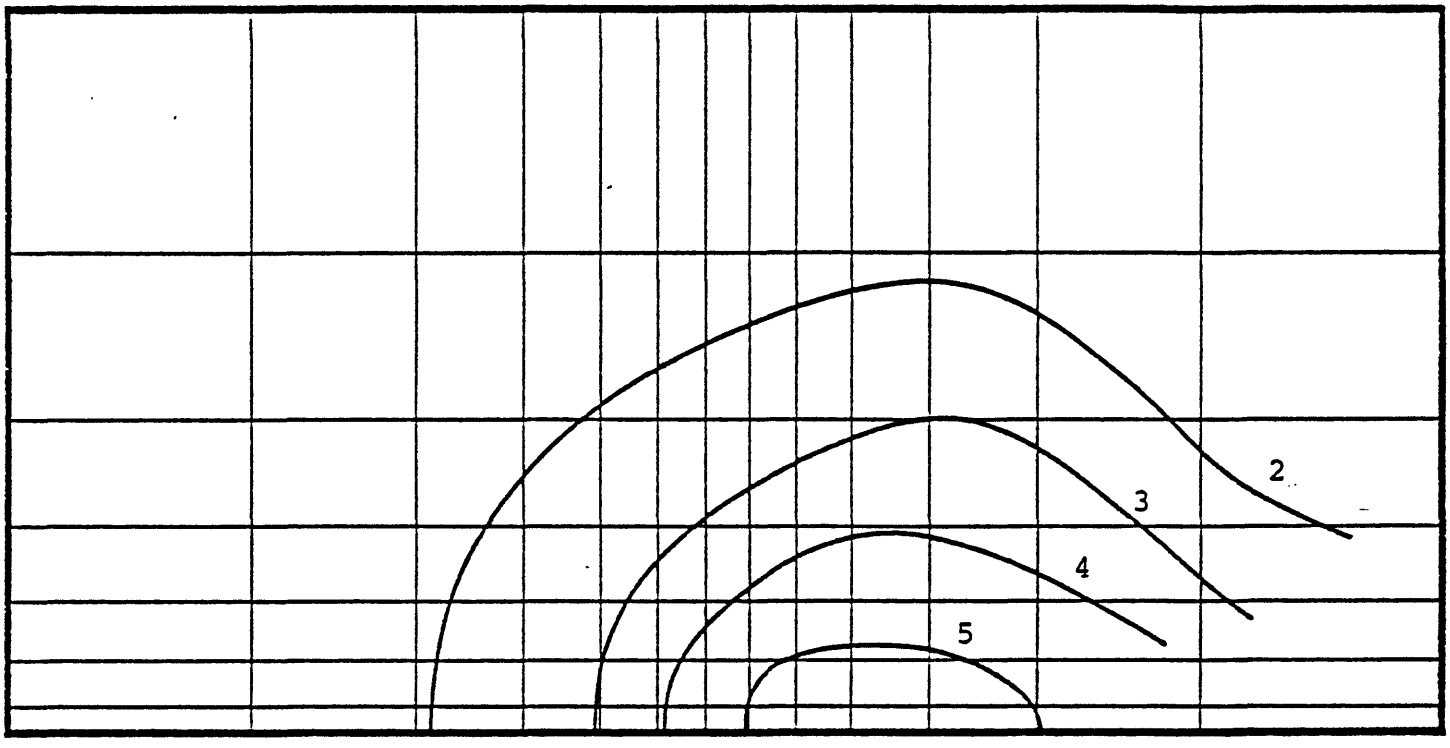

(a) Surface Heat Flow, H.F.U.

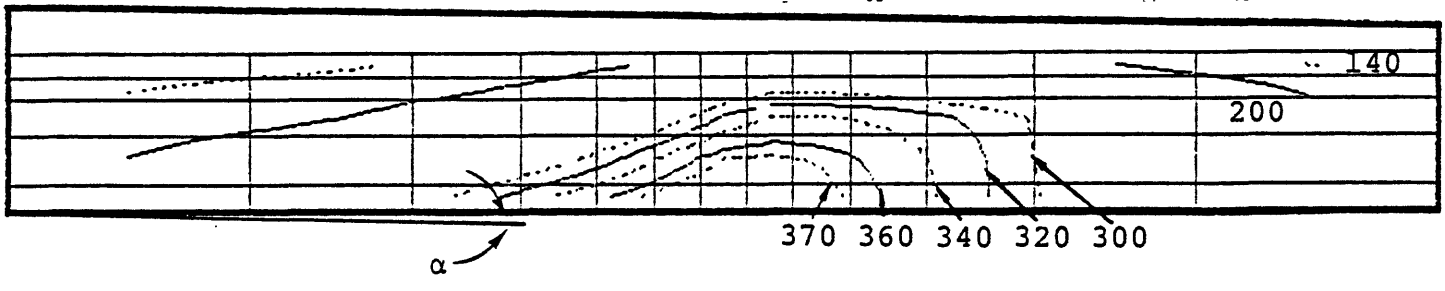

(b) Temperature Field, °F

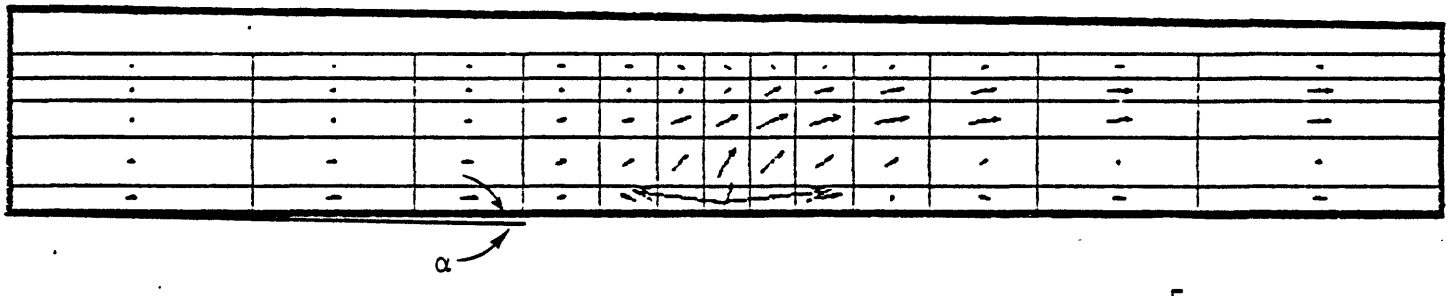

(c) Velocity Field, longest vector corresponds to 1.00×10^{-5} cm/sec.

Figure 30. Steady-state conditions for case with axisymmetric source and intermediate structure dip (Run EML-202; tan α = 0.0164).

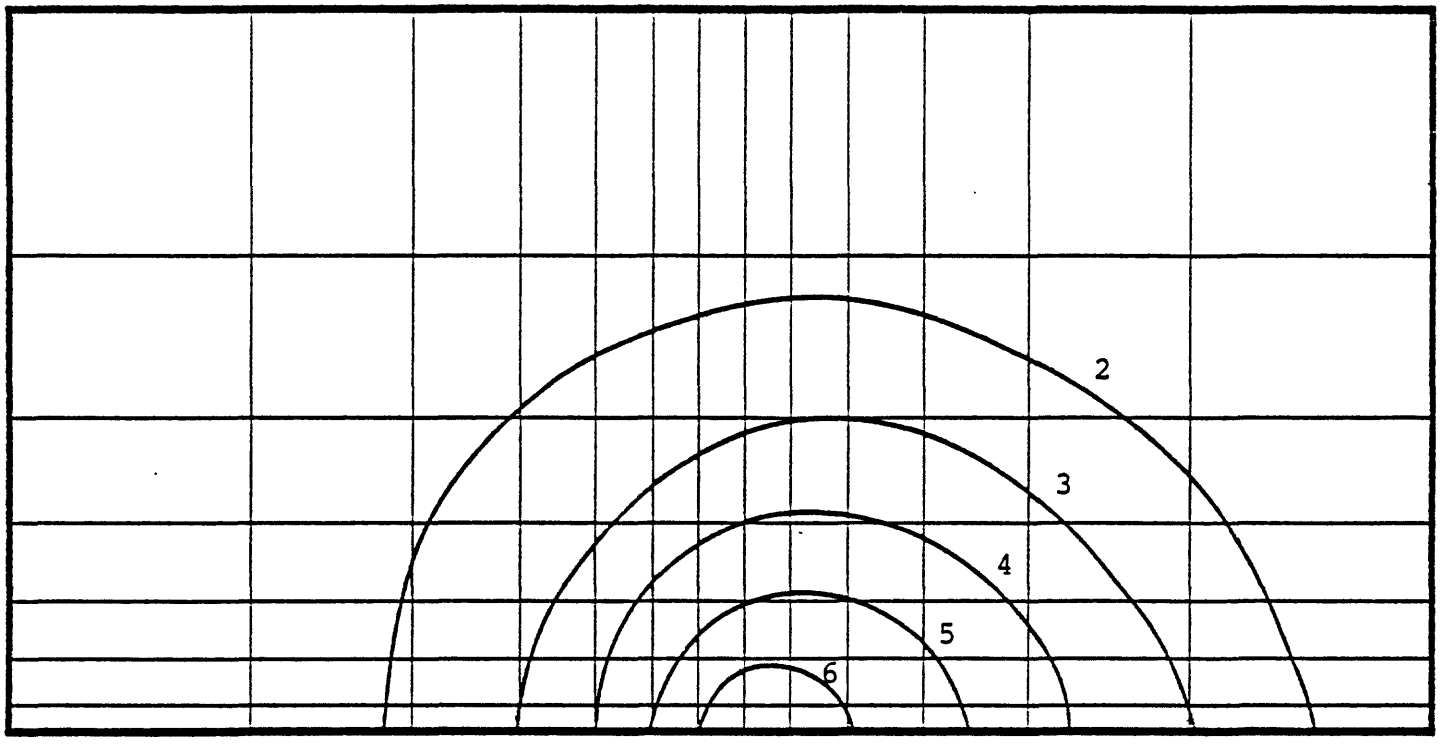

(a) Surface Heat Flow, H.F.U.

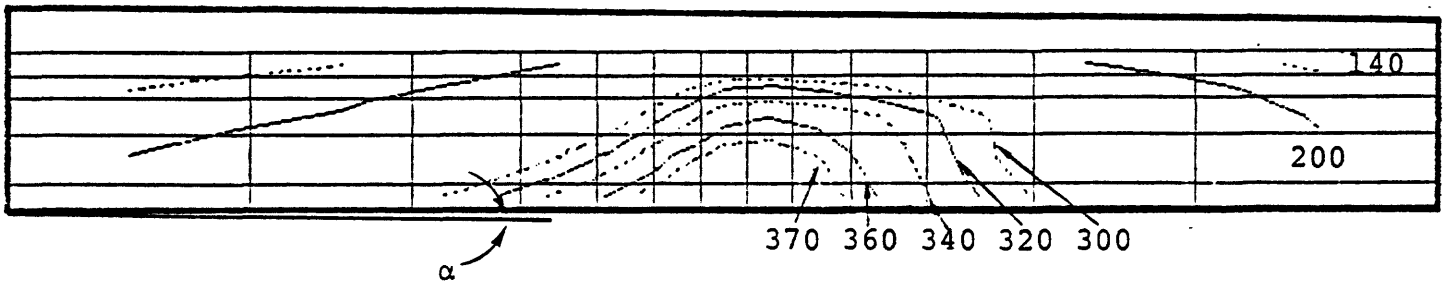

(b) Temperature Field, °F

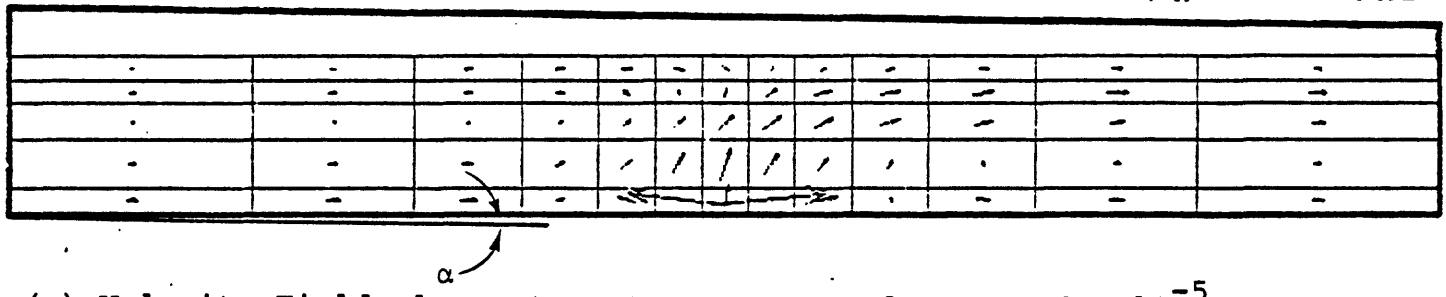

(c) Velocity Field, longest vector corresponds to 0.96×10^{-5} cm/sec.

Figure 31. Steady-state conditions for case with axisymmetric source and small structural dip (Run EML-203; tan α = 0.0082).

updip because of its buoyancy. The fluid leaving the central region is largely replaced by cold fluid originating downdip as shown by the velocity vector plots for each choice of α.

It is instructive to examine the effect of structural dip on the steady-state temperature-depth profiles at equal distances from the convective source, updip and downdip. Figure 32 presents plots of profiles at selected distances from the source for the axisymmetric case (Run EML-6) together with profiles at corresponding distances calculated for the three cases in which structural dip was introduced. Downdip the profiles are straightened relative to the axisymmetric case as a consequence of the increased importance of heat transfer by conduction and decreased convective heat transfer. Updip the profiles are much steeper at depth reflecting the fact that heat transfer by convection is dominant even at large distances from the hot convective source. Such plots may be useful as type curves as a guide to locating the source of the hot fluid in structurally complex single-phase geothermal reservoirs. Their use would implicitly assume that the steady-state temperature-depth measurements made in exploratory wells approximate the true temperature-depth relation in the formation.

The effect of structural dip is qualitatively very similar to that of the imposition of a lateral pressure gradient as is apparent from comparison of Figures 29 through 31 with Figures 27 and 28. The orientation of the dip of the geothermal cap at East Mesa at the center of anomaly is generally to the northeast, corresponding to one of the lobes in the surface heat flow contours.

6.3 LEAKY FAULTS

So far, the hot fluid which drives the system has been assumed to emanate from a point-source located at the bottom surface of the

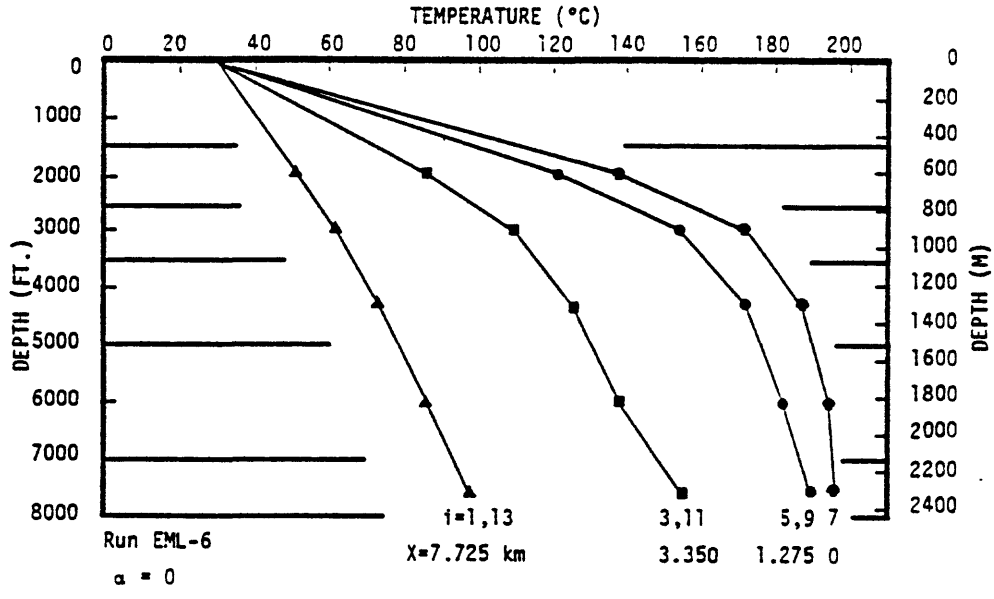

(a) Run EML-6; tan α = 0

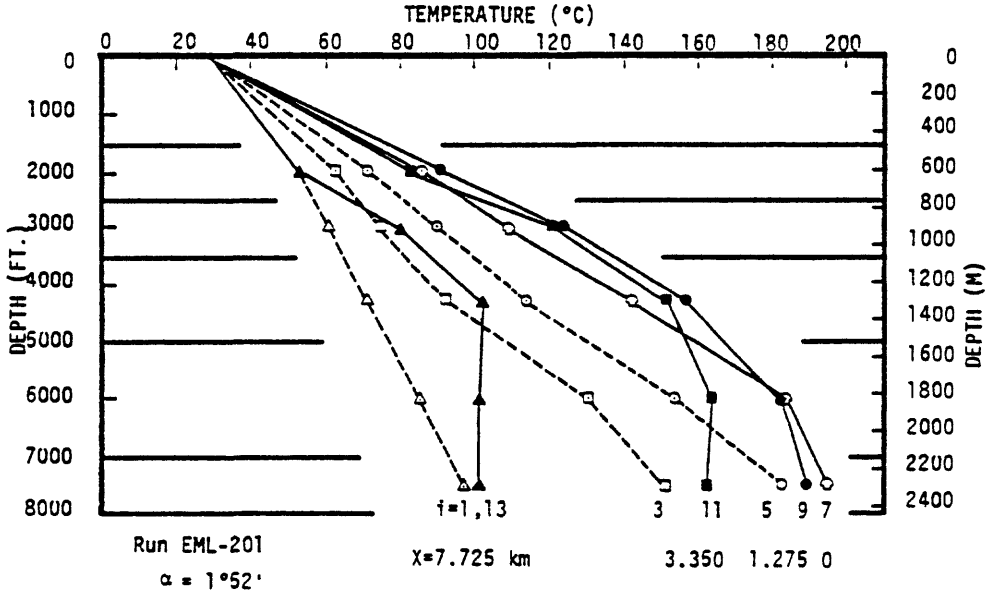

(b) Run EML-201; tan α = 0.0328

Figure 32. Steady-state temperature-depth profiles at indicated distance from axisymmetric convective source (section along xz-plane in each of four cases). Locations denoted by i=1, 3, 5 are downdip, i=7 is over the source, and i=9, 11, 13 are updip.

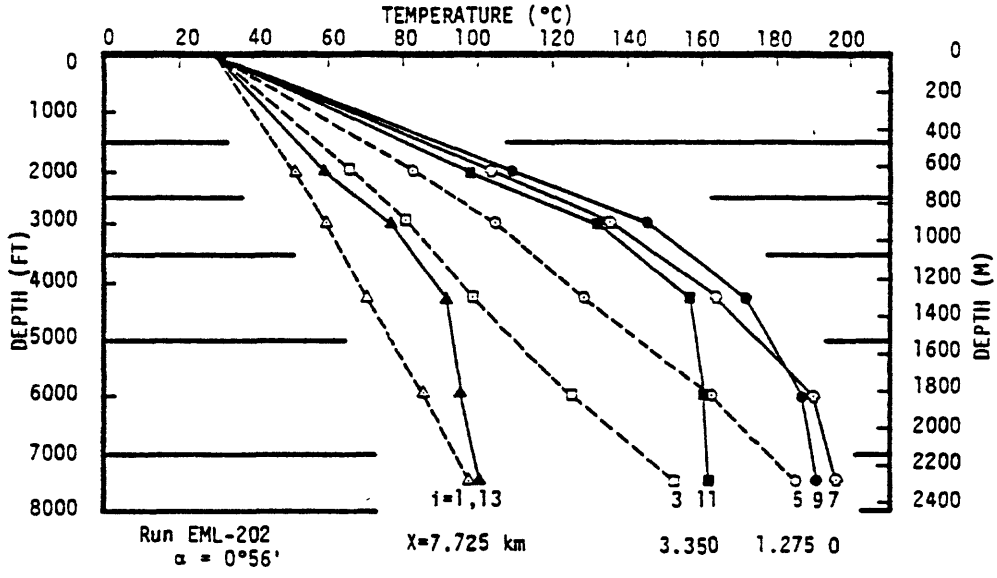

(c) Run EML-202; tan α = 0.0164

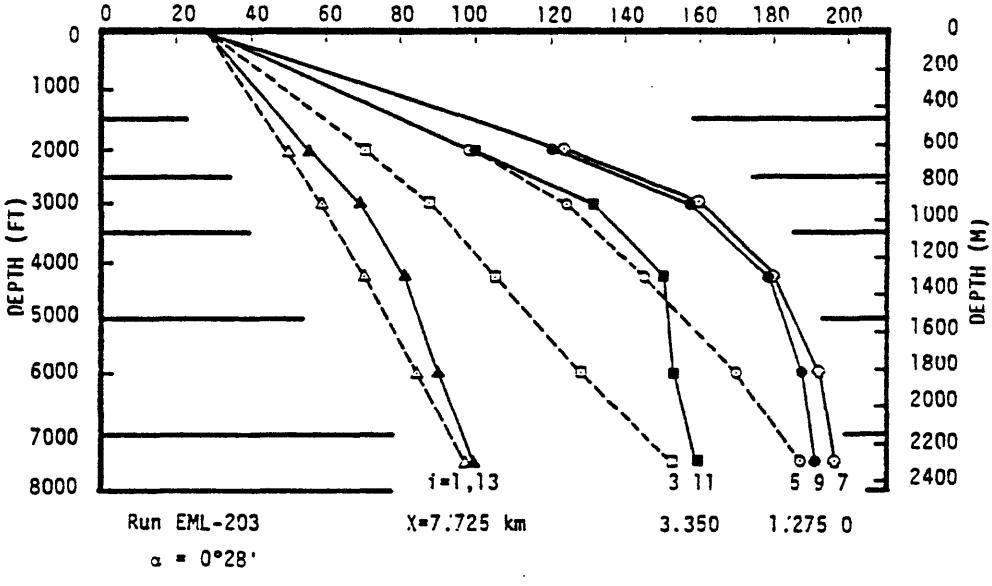

(d) Run EML-203; tan α = 0.0082

Figure 32.

computational grid which is associated with an axisymmetric region of relatively high vertical permeability presumably arising from the presence of intersecting faults (see Figure 23). In this section, a series of LIGHTS calculations are presented which examine the effects of hot fluid convecting into the reservoir along an extended vertical fault which intersects the cylindrical region. The fault is considered to result in enhanced vertical permeability along a radial plane passing through the center of the hot spot; the vertical permeability is considered to be k_v = 0.5 md in the plane of the fault (xz-plane of symmetry) and to decrease laterally to k_v = 0.25 md in a manner analogous to the variation depicted in Figure 23 (see Figure 33a). LIGHTS has been used to examine the effect of varying the distribution and temperature of the convective source issuing from such a vertical fault.

6.3.1 Source Distributions Along Fault

A series of LIGHTS calculations was made to investigate the effect of varying the distribution of the convective fluid source entering the reservoir along the fault. The vertical permeability and the choices for the distributed convective source which were used to model the fault in the LIGHTS calculations are depicted in Figure 33. The total convective mass rate in the fault model is taken to be

$$\dot{M}_C = 20 \text{ kg/sec } (T_C = 196.11^\circ C)$$

That is, the total mass of the convective source was taken to be twice what it was for the axisymmetric source. All other input data for these LIGHTS calculations were the same as in axisymmetric LIGHTS Run EML-6.

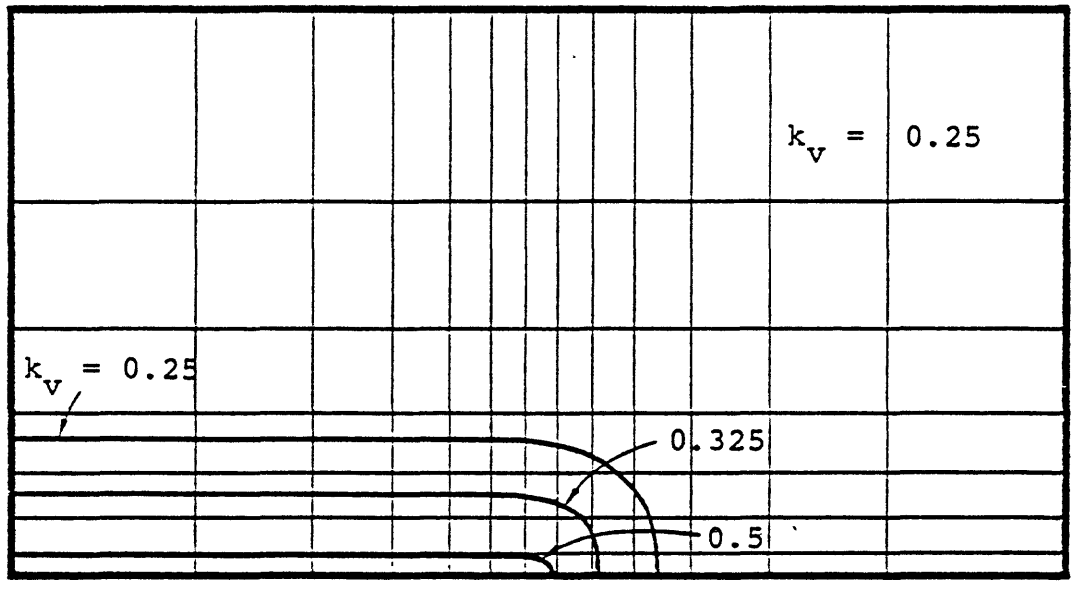

(a) Vertical Permeability (k=1, ...,5)

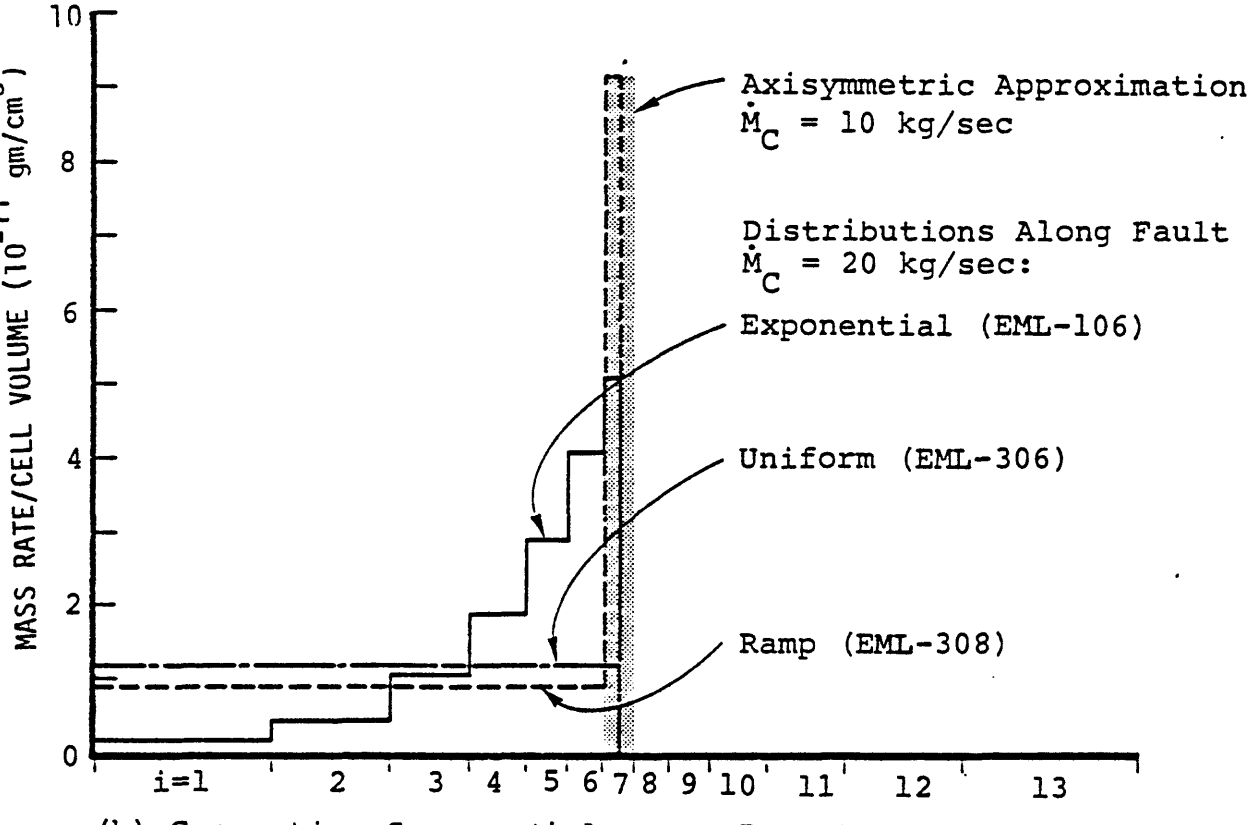

(b) Convective Source (i=1, ..., 7; j=1, k=1)

Figure 33. Distributions of (a) vertical permeability and (b) convective hot fluid source assumed in the various fault models.

Figure 34 illustrates the steady-state LIGHTS solution obtained when the hot-water input flow rate along the fault decreases exponentially with distance from the center of the hot spot (Run EML-106). Comparison of the temperature contours in Figure 34(b) with those in Figure 26(b) illustrates that this distribution of the convective mass source along the fault does increase the distance between the "upfault" isotherms, bringing the contours in closer qualitative agreement with the extrapolated data in Figure 17 (corresponding to the direction of the predominant fault set at East Mesa). The comparison indicates, however, that the assumed exponential source distribution in the fault model does not alone provide the skewness in the isotherms that the data apparently require.

Figure 35 illustrates the steady-state solution obtained when the convective source is assumed to be uniformly distributed along the fault (Run EML-306). This distribution greatly increases the skewness of the isotherms in the "upfault" direction. The computed temperature contours in Figure 35(b) are in good qualitative and reasonable quantitative agreement with the extrapolated data in Figure 17, provided the fault is assumed to be aligned to the north from the hot spot corresponding to the direction of the predominant East Mesa fault set. The calculated surface heat flow contours in Figure 35(a) are elongated to the north along one of the temperature lobes in Figure 12, but the peak value of 6 HFU the center of near the hot spot is lower than measured data.

In an attempt to increase the peak surface heat flow, a third LIGHTS calculation was made using the ramp source distribution shown in Figure 33(b). The results for this calculation (Run EML-308) are illustrated in Figure 36. The peak surface heat flow increased but remained less than the desired value (~ 7 HFU). There was a decrease in the skewness of the isotherms so that the overall

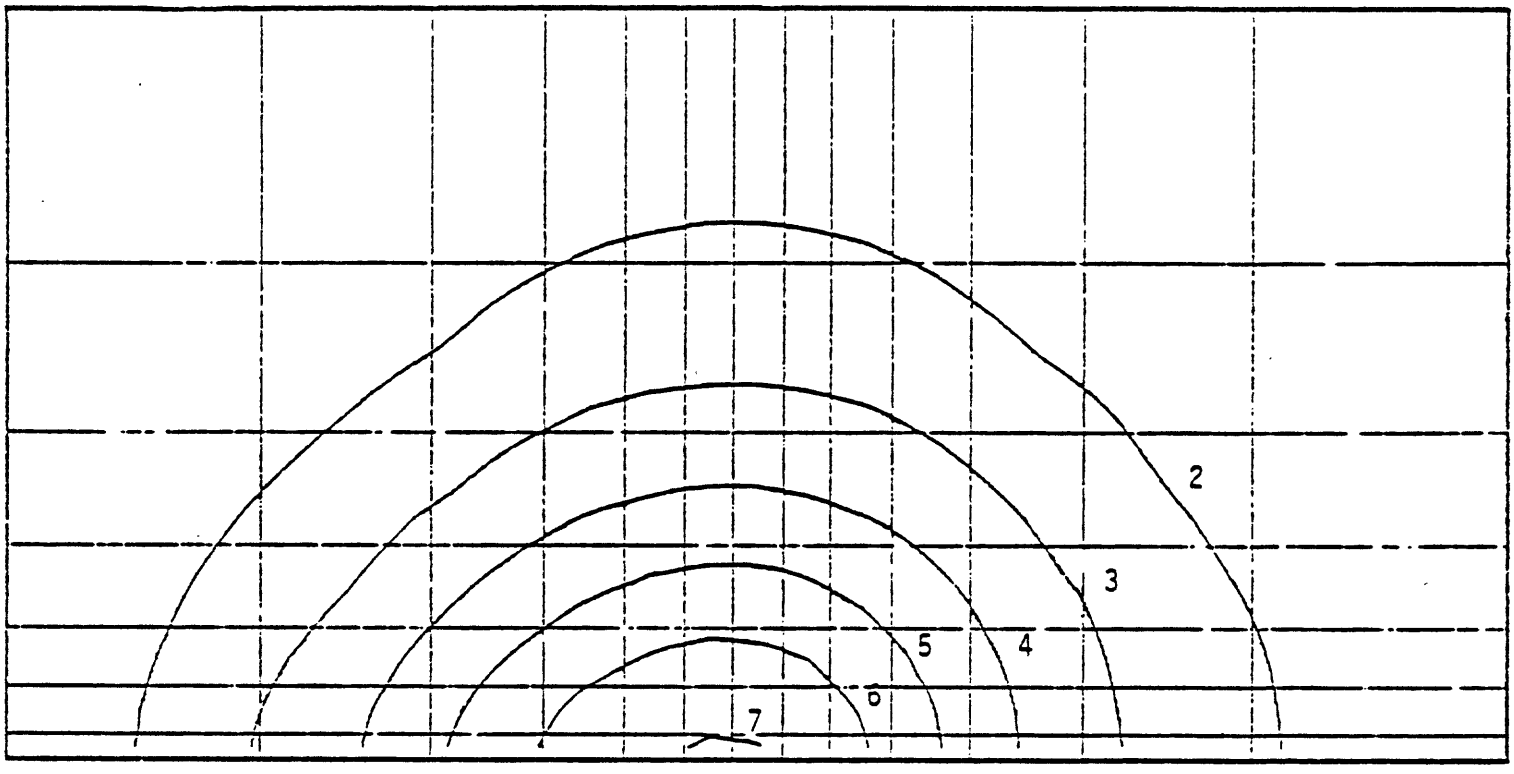

(a) Surface Heat Flow, H.F.U.

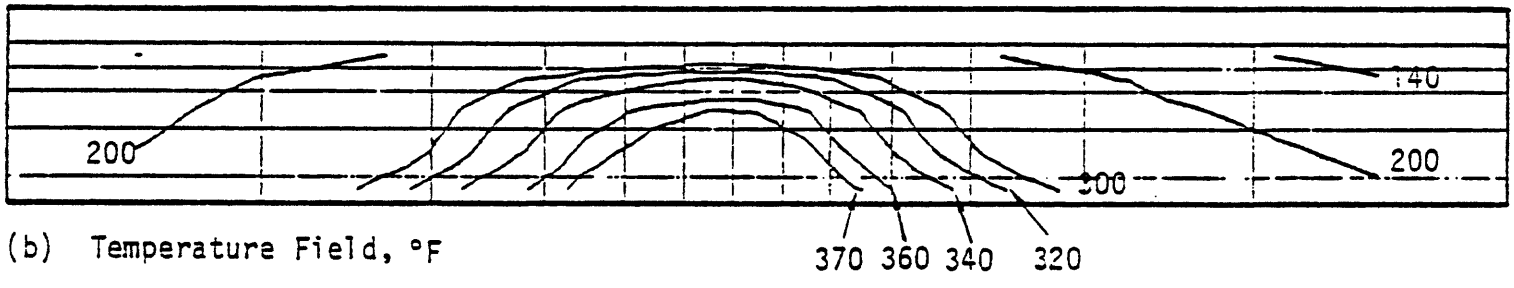

(b) Temperature Field, °F

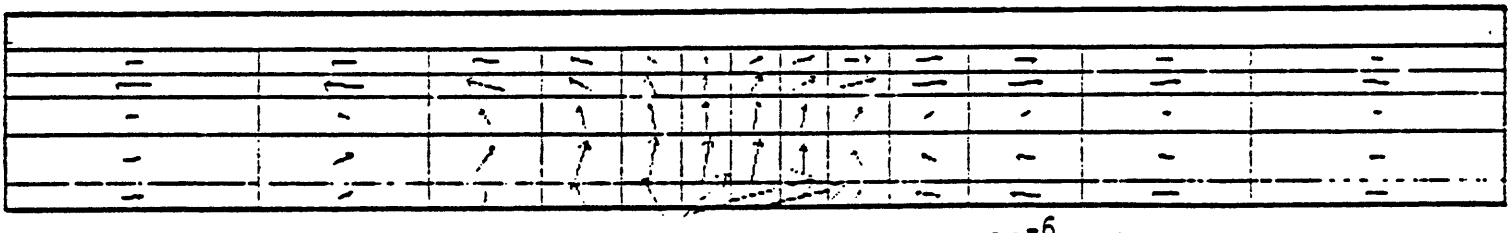

(c) Velocity Field, longest vector corresponds to 5.93×10^{-6} cm/sec.

Figure 34. Steady-state conditions for case in which fault model with exponential source distribution is included (Run EML-106; $\dot{M}_C$ = 20 kg/sec distributed along fault.

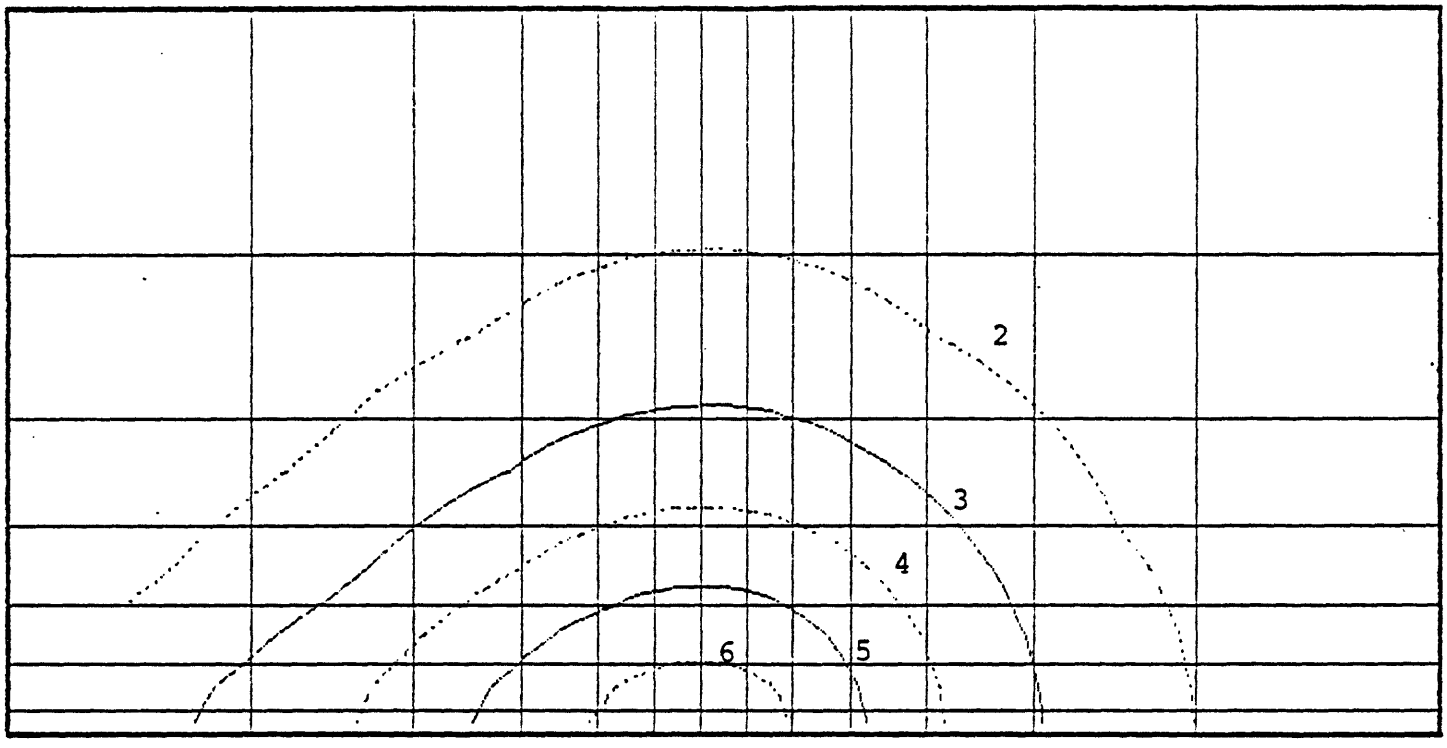

(a) Surface Heat Flow, H.F.U.

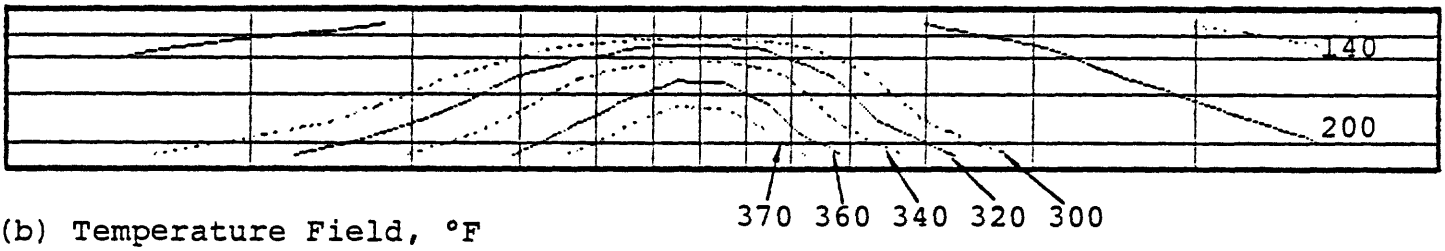

(b) Temperature Field, °F

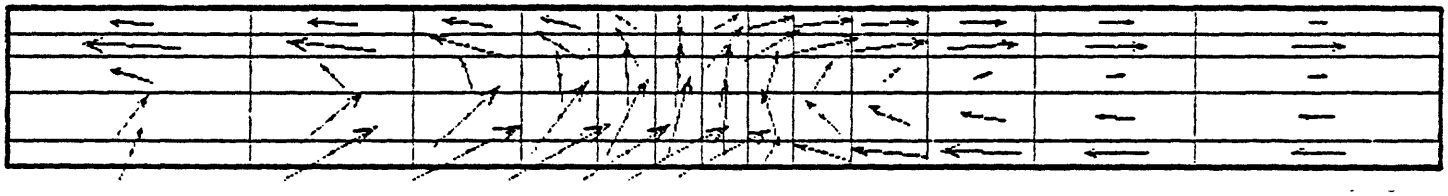

(c) Velocity Field, longest vector corresponds to 2.25×10^{-6} cm/sec.

Figure 35. Steady-state conditions for fault model with uniform distribution of convective source along fault (Run EML-306; $\dot{M}_C$ = 20 kg/sec).

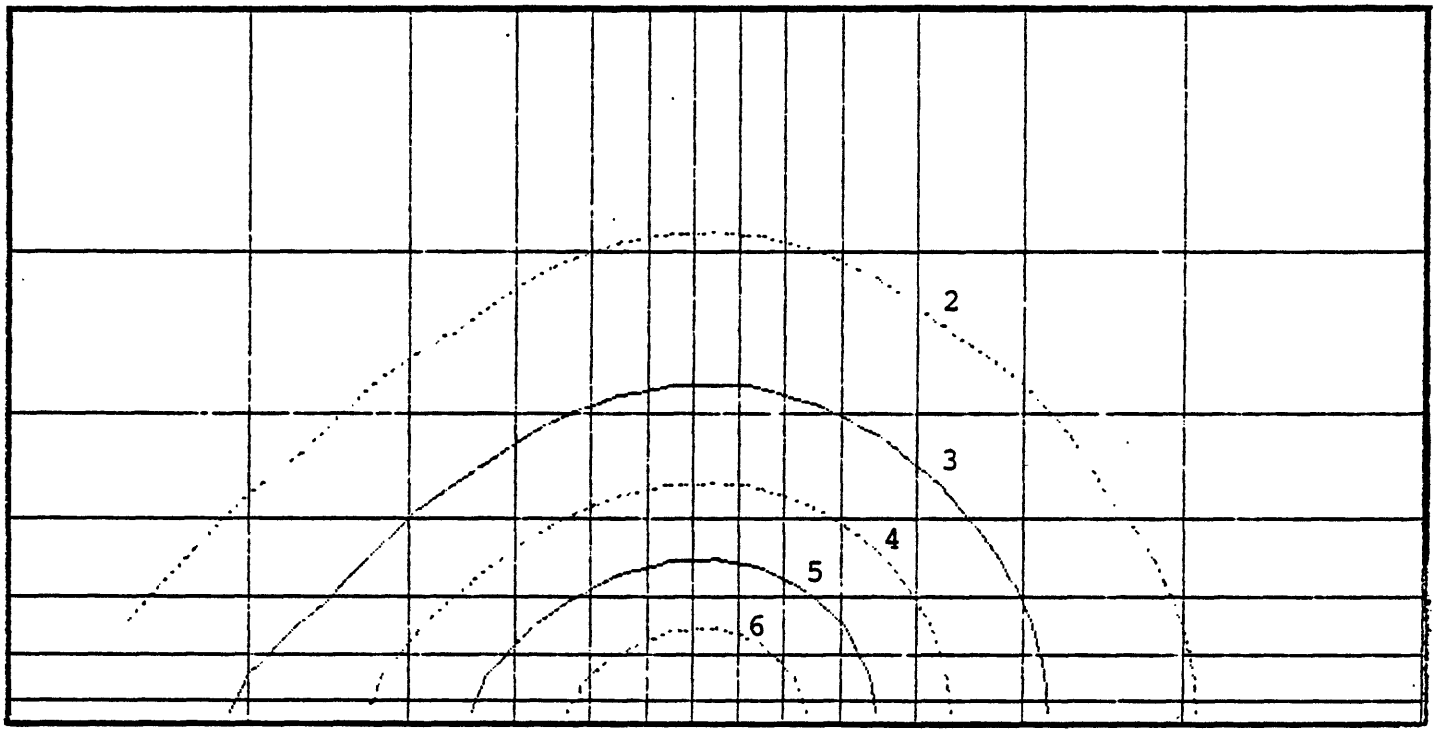

(a) Surface Heat Flow, H.F.U.

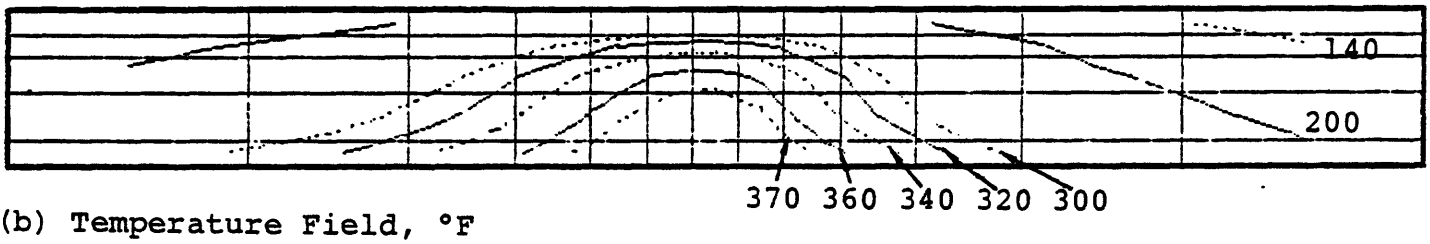

(b) Temperature Field, °F

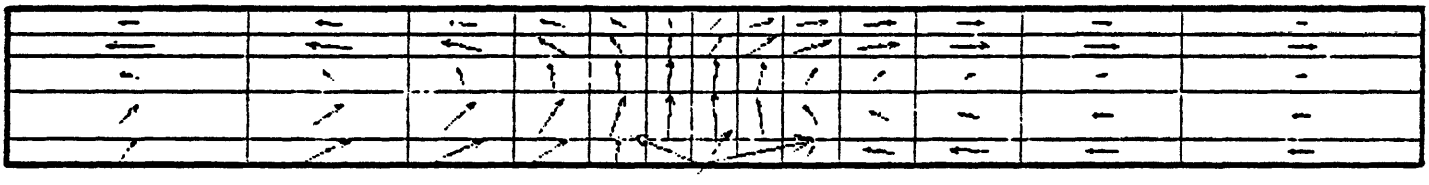

(c) Velocity Field, longest vector corresponds to 4.46×10^{-6} cm/sec.

Figure 36. Steady-state conditions for fault model with ramp distribution of convective source along fault (Run EML-308; $\dot{M}_C$ = 20 kg/sec).

match with the extrapolated data in Figure 17 was not improved from that achieved with the uniform source distribution.

6.3.2 Thermal Input Variations

Two LIGHTS calculations were made in which the fault model with the uniformly distributed source was employed with different thermal input data than those used in Run EML-306. The sensitivity of the results to the input temperature of the convective source (T_C) and the assumed bottom boundary temperature (T_B) were examined in separate calculations. All other input data were the same as in Run EML-306.

The value T_C = 196.11°C = 385°F was initially selected to approximate the temperature along the vertical axis in the axisymmetric distribution (Figure 20) at a depth corresponding to the center of the bottom layer in the finite difference grid (i.e., a depth of 7,500 feet). At the bottom of this layer (depth of 8,000 feet), however, a peak temperature that exceeds that value by 8°C has been measured in the Mesa 6-2 well. Therefore, the calculation with the source uniformly distributed along a leaky fault was rerun with T_C = 204°C (Run EML-310) and the results are illustrated in Figure 37. The results are very similar to those obtained in Run EML-306 as comparison of Figures 35 and 37 shows. The maximum temperature in the reservoir increased only by about ~ 2°C. This result indicates that the steady-state temperature field at East Mesa is strongly influenced by conductive heat transfer since increasing the convective contribution made so little difference.

An additional LIGHTS calculation was made using the same uniformly distributed convective source as Run EML-306 (T_C = 196.11), but the conductive heat flow at the bottom boundary was

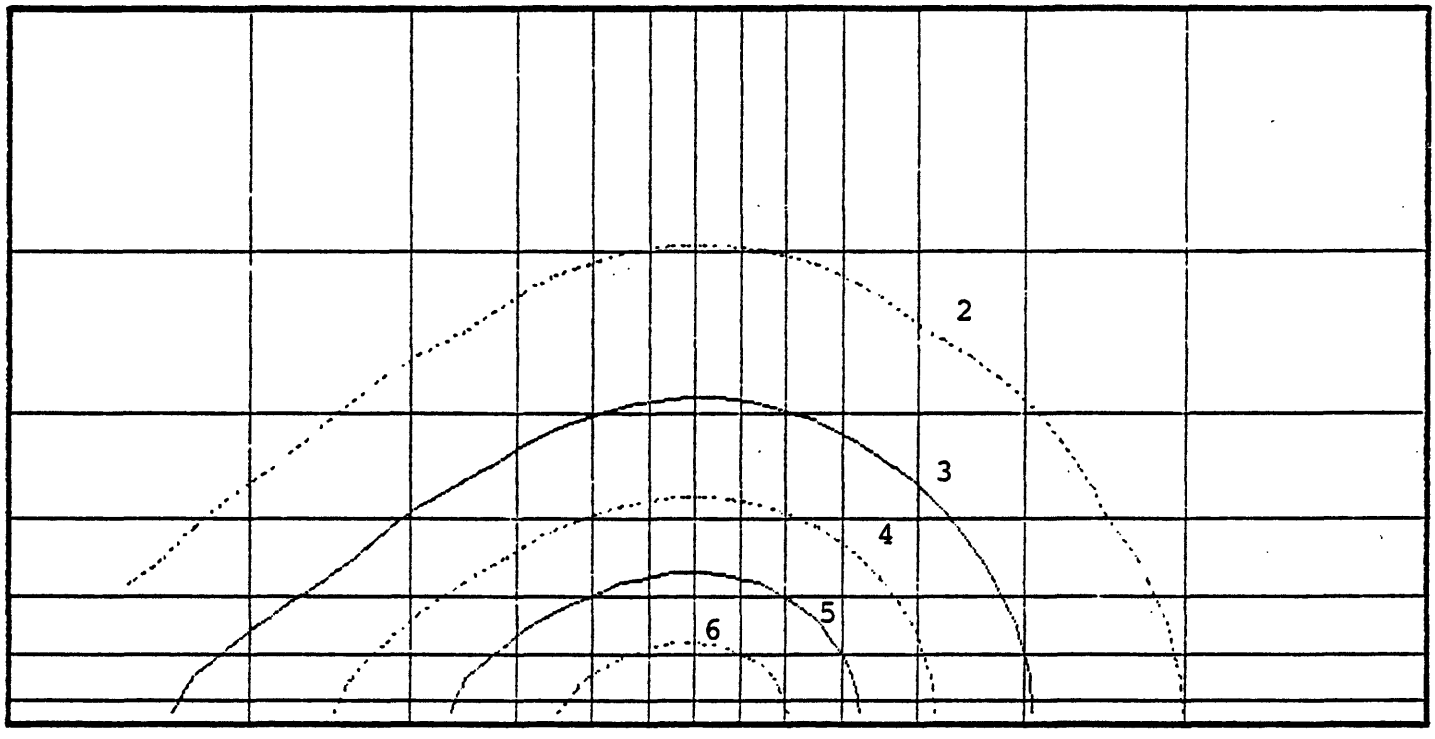

(a) Surface Heat Flow, H.F.U.

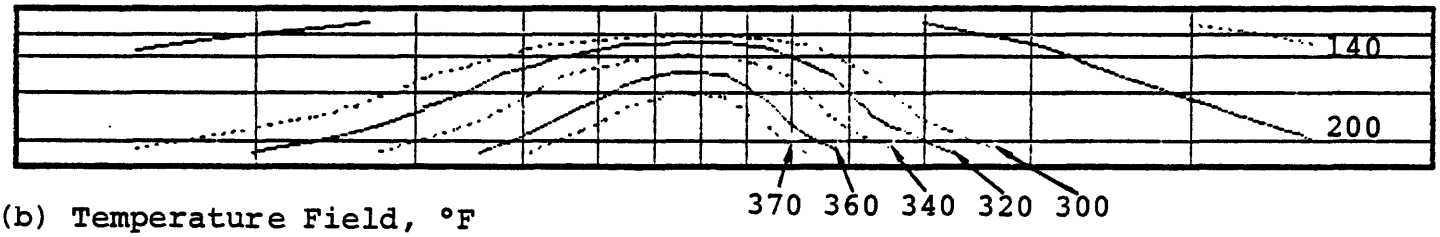

(b) Temperature Field, °F

(c) Velocity Field, longest vector corresponds to 2.31×10^{-6} cm/sec.

Figure 37. Steady-state conditions for fault model with uniformly distributed convective source at elevated temperature (Run EML-310; $\dot{M}_C$ = 20 kg/sec; T_C = 204°C).

increased. In Run EML-311, the temperature distribution (T_B) imposed at the bottom of the LIGHTS grid was chosen to better represent the data at a depth of 8,000 feet than had been used previously. As shown in Figure 22 by the broken line, the imposed T_B distribution peaks at 204°C as indicated by the Mesa 6-2 well data. The steady-state LIGHTS solution obtained is illustrated in Figure 38. The reservoir temperatures in the vicinity of the axis are increased by ~ 6.8°C and the peak surface heat flow is increased to 7 HFU; these results are in good agreement with the data shown in Figure 17 if the fault is considered to radiate north from the hot spot center.

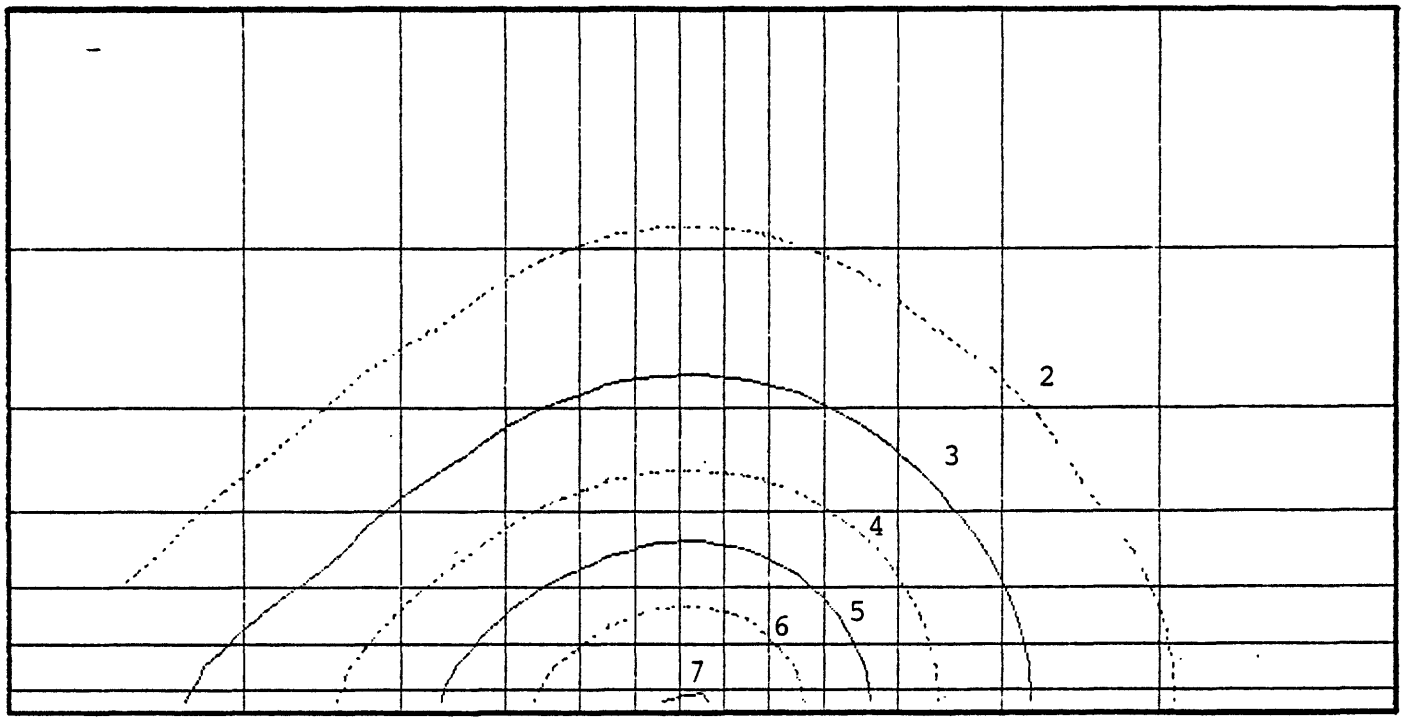

(a) Surface Heat Flow, H.F.U.

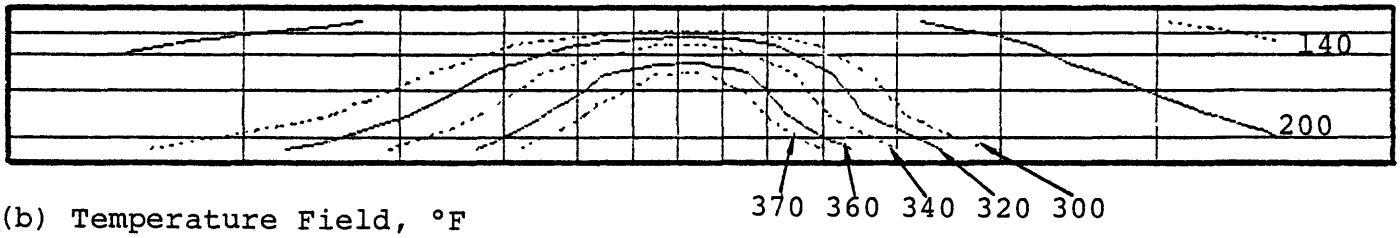

(b) Temperature Field, °F

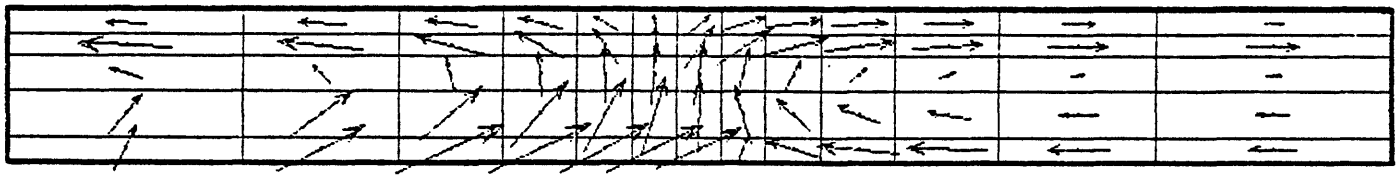

(c) Velocity Field, longest vector corresponds to 2.46×10^{-6} cm/sec

Figure 38. Steady state conditions for fault model with uniformly distributed convective source with bottom boundary at elevated temperature (Run EML-311; M_C = 20 kg/sec; T_C = 196°C; T_B increased).

VII. FULLY ASYMMETRIC SIMULATIONS

In this section lateral variations of ϕ and k_h approximating the estimated true distributions of these formation properties are introduced into the LIGHTS calculations. The non-axisymmetric variation of the temperature distribution (T_B) imposed at the bottom of the LIGHTS grid to better represent the data at a depth of 8,000 feet is also included in the calculations. The information developed in Subsection 3.3 and presented in Figures 16 through 19 are the basis for the lateral distributions of ϕ, k_H and T_B assumed in these studies.

7.1 LATERAL VARIATIONS WITH AN AXISYMMETRIC SOURCE

Realistic treatment of the lateral variations requires that the full LIGHTS grid be employed -- there is no bilateral plane of symmetry. Figure 39 shows the horizontal grid (Z = constant; k = 1, ..., 5) employed along with the East Mesa temperature contours prepared by TRW for a depth of Z = 6,000 feet (see Figure 14). The wells used in the TRW study are also shown for reference purposes. The approximate lateral distributions of the formation porosity (ϕ) and formation horizontal permeability (k_h) in each of the five horizontal layers are depicted in Figures 40(a) through 40(d). In these figures, the locations of the wells used in the TRW study are again shown for orientation purposes. Figure 41 shows the temperature distribution imposed at the bottom surface (8,000 feet depth) of the LIGHTS grid. The peak temperature is imposed at the bottom surface of the center zone (1=7, j=7, k=1) where T_B = 204°C (399°F).

In Run EML-403 the only asymmetries introduced are the lateral variations in ϕ, k_h and T_B discussed above; there are no vertical faults, regional pressure gradients, or explicit treatment of structural dip by tilting the horizontal layers (except as reflected in variations in the formation properties). The total

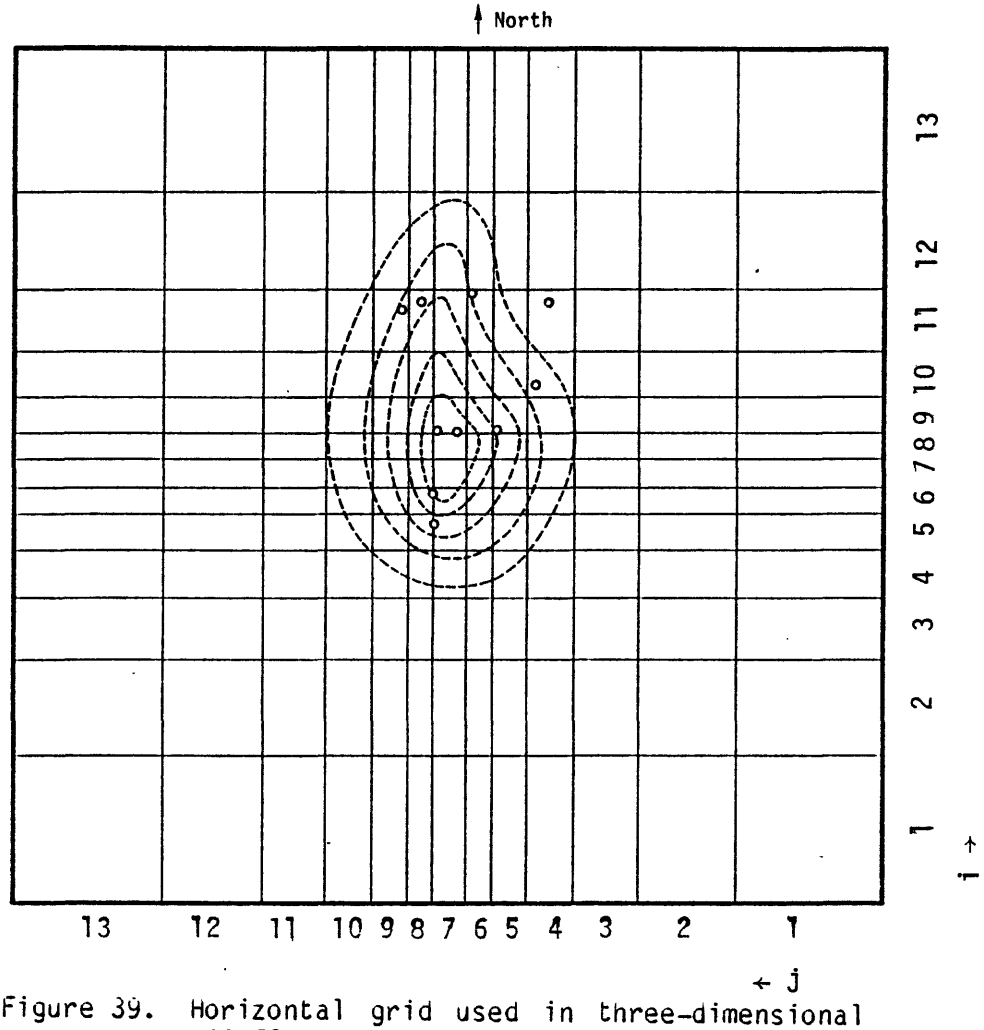

Figure 39. Horizontal grid used in three-dimensional LIGHTS simulations with temperature contours (prepared by TRW for the Z=6,000 feet) and well locations superposed for reference purposes.

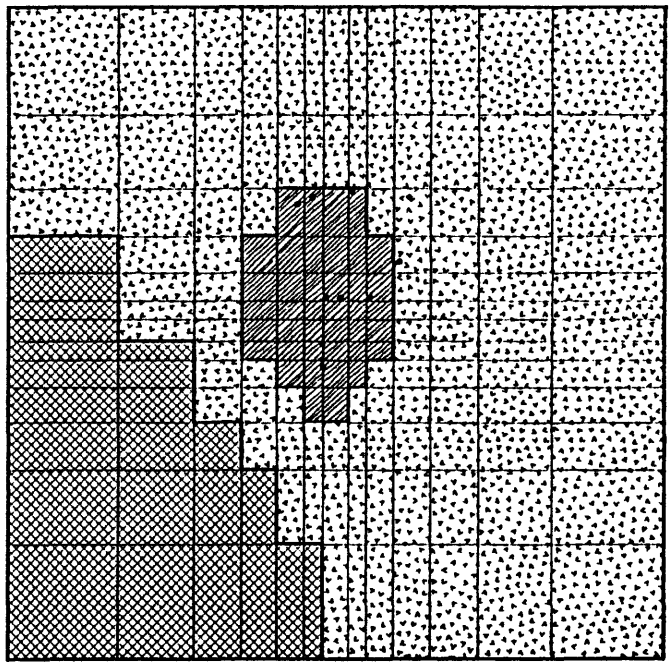

(a) Layer k=1 (7,000' - 8,000').

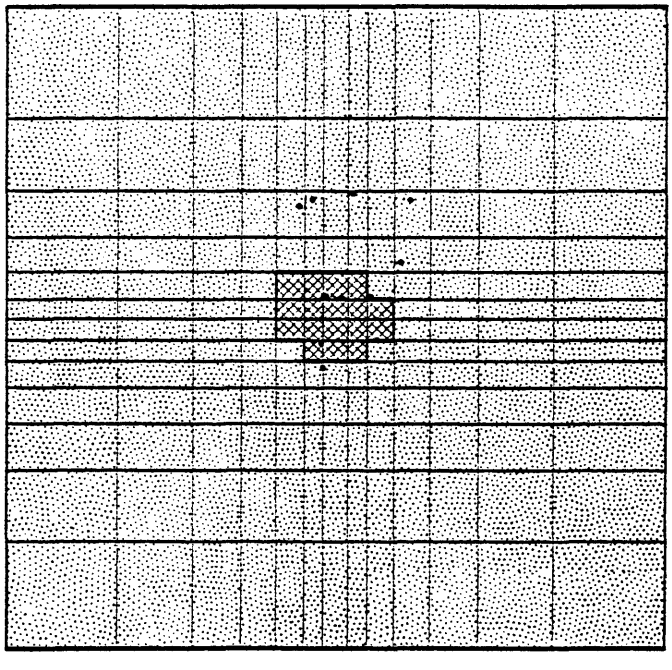

(b) Layer k=2 (5,000' - 7,000').

LEGEND

ϕ	k_h(md)
0.075	4
0.100	9
0.125	20
0.175	90
0.225	320
0.275	850

Figure 40. Distribution of formation porosity (ϕ) and horizontal formation permeability (k_h) used in LIGHTS calculations treating lateral variations of these properties.

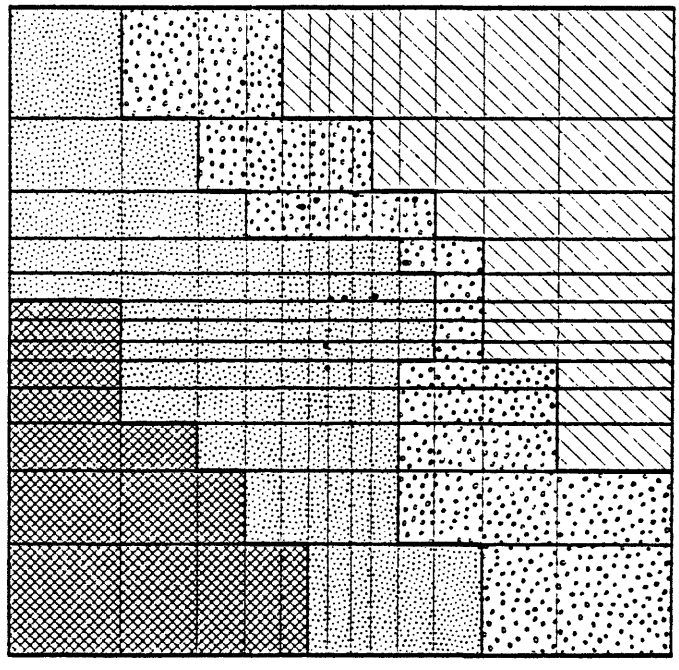

(c) Layer 3 and 4 (2,500' - 5,000')

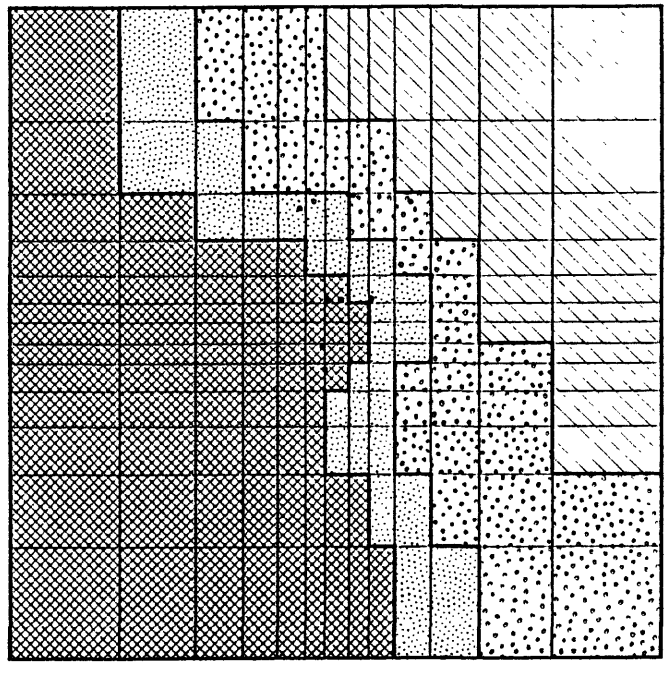

(d) Layer 5 (1,500' - 2,500').

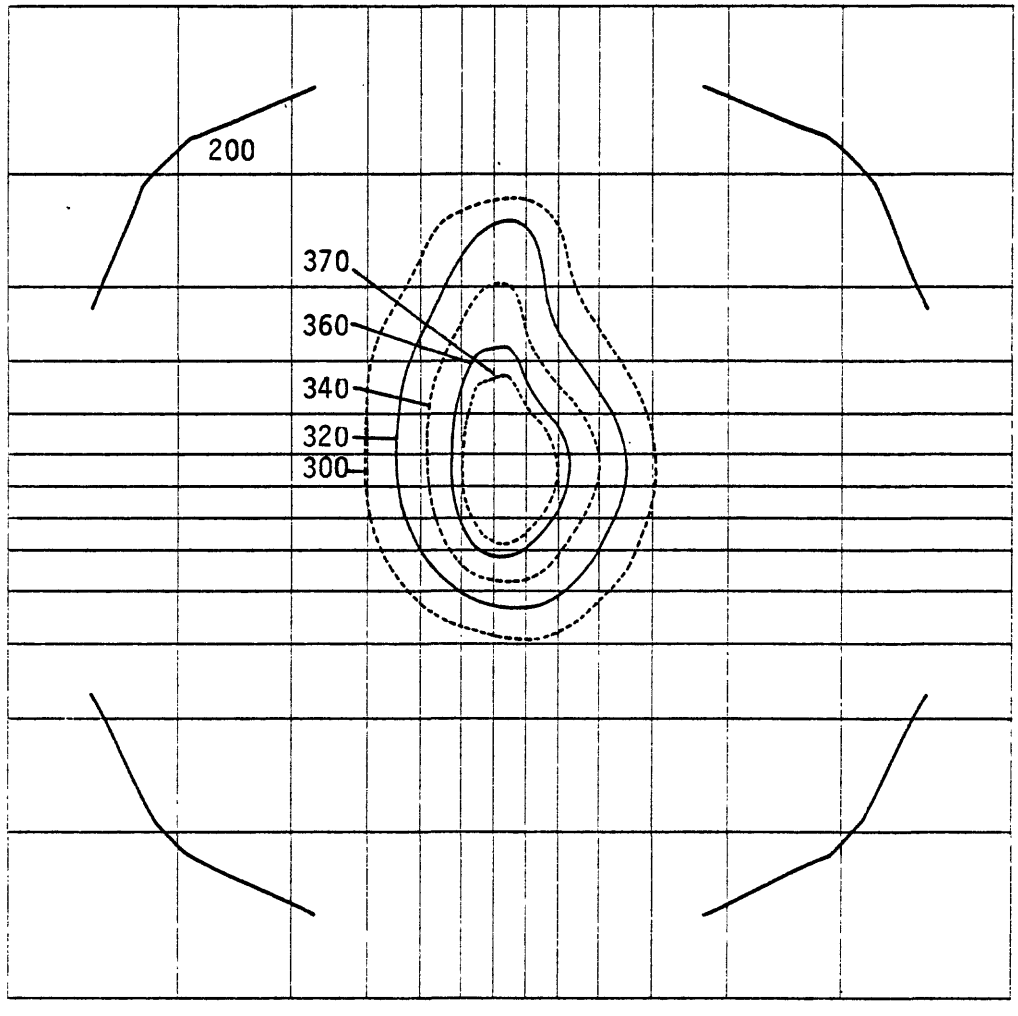

Figure 41. Temperature (T_B in °F) imposed at bottom boundary (8,000 feet depth) of computational mesh in fully asymmetric LIGHTS simulations.

mass flow across the bottom surface of the grid, as in several prior calculations, amounts to a point source entering the center zone (i=7, j=7, k=1); the total convective mass rate is taken to be

$$\dot{M}_C = 10 \text{ kg/sec } (T_C = 204^\circ C)$$

That is, the convective source is the same as that used in the axisymmetric approximation (Run EML-6) with the temperature raised to 204°C.

All other input data duplicate those used in the axisymmetric approximation as described in Subsection 5.2. The surface heat loss is mimiced by a distributed heat sink according to Equation (27). The four vertical boundaries of the modeled region are considered to be in hydrostatic equilibrium with the surrounding formation waters. The vertical permeability (k_m) varies from 0.5 md at the axis of the convective source to 0.25 md according to the distribution shown in Figure 23, and all other formation and fluid properties remain the same.

Computer-generated plots created by LIGHTS are presented in Figures 42 through 45 to demonstrate the effect of lateral variations of the formation properties on the steady-state conditions (75,520 years) obtained in Run EML-403. Figure 42 shows the surface heat flow predicted by this model. The calculated values are in fairly good agreement with the data shown in Figure 12 except for the higher values measured along the northern lobe. Figures 43 and 44 depict the temperature and fluid velocity distributions along, respectively, south-north (SN) and west-east (WE) vertical sections passing through the center of the axisymmetric convective source. Examination of the south-to-north (compare Figure 43(a) with Figure 17) and west-to-east (compare Figure 44(a) with Figure 18) distributions of the subsurface temperature show that the calculations are in good qualitative and

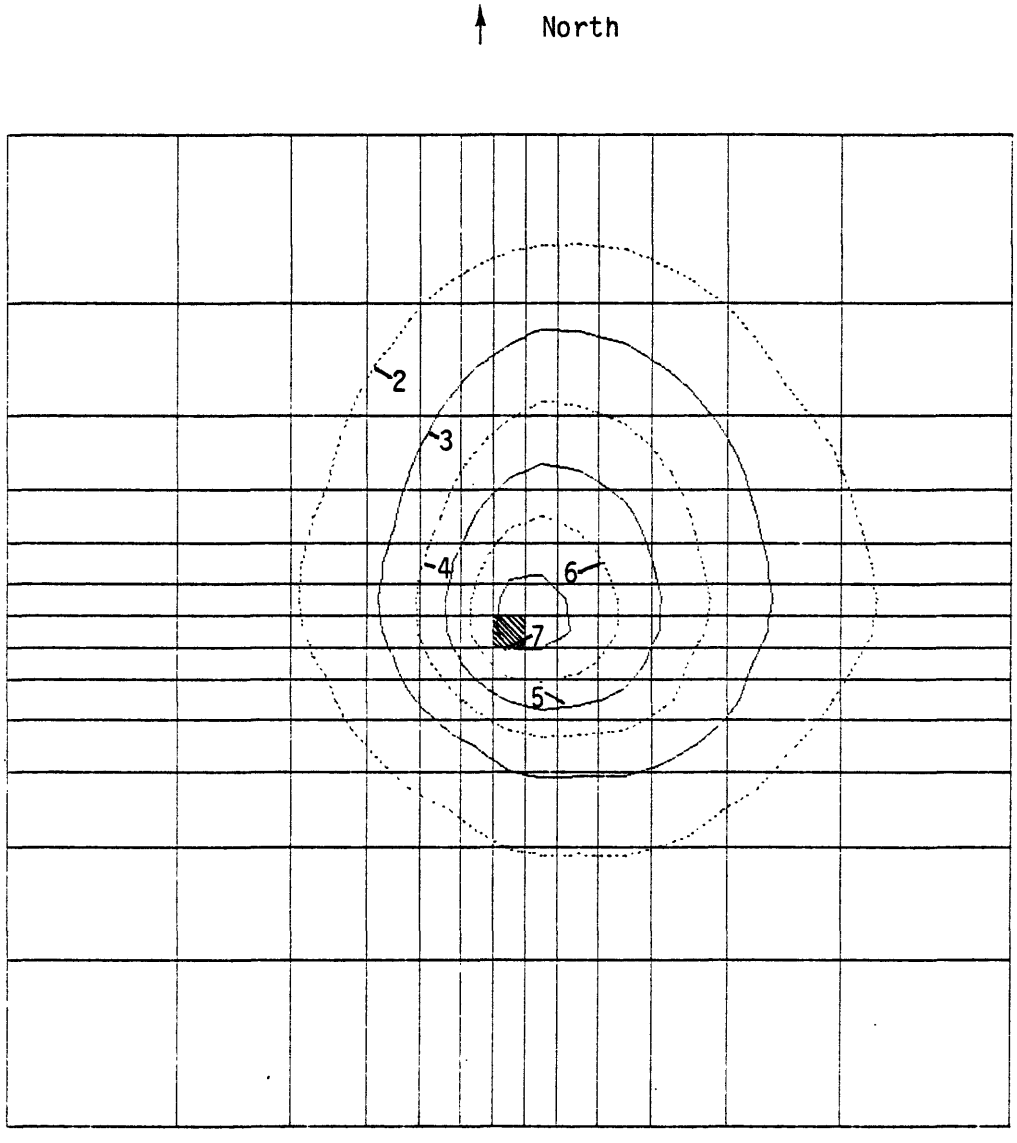

Figure 42. Steady-state surface heat flow (H.F.U.) for case in which lateral variations in ϕ, k_h and T_B are treated with an axisymmetric source (Run EML-403; M_C = 10 kg/sec; T_C = 204°C). Shaded area covered by axisymmetric source distribution in Layer 1.

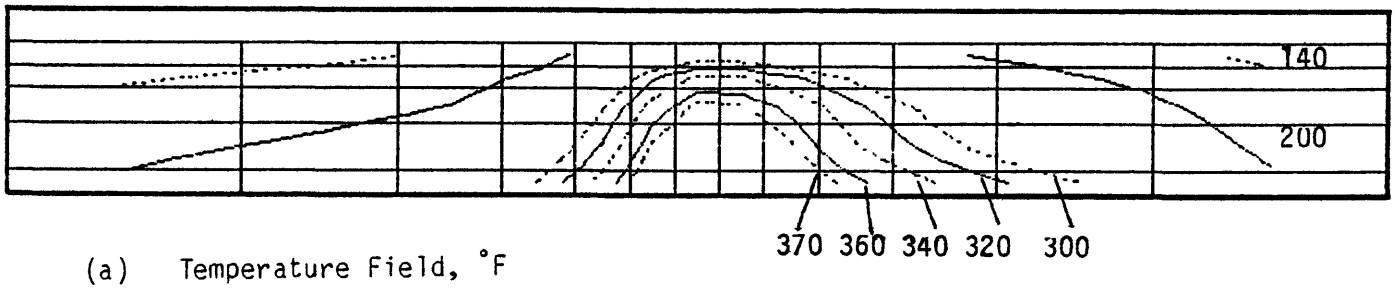

(a) Temperature Field, °F

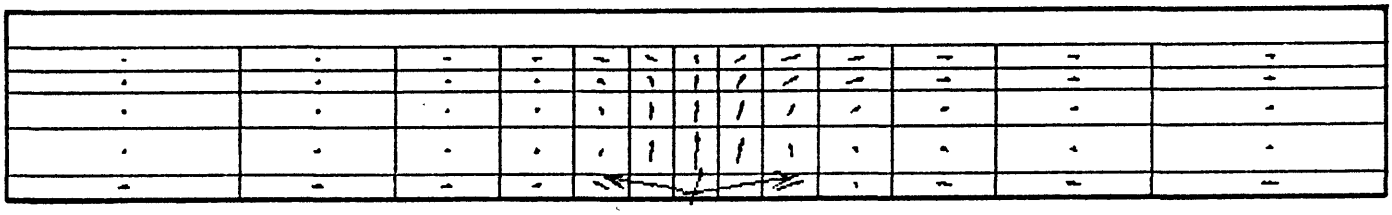

(b) Velocity Field, longest vector corresponds to 1.04×10^{-5} cm/sec.

Figure 43. Vertical section SN through center of axisymmetric source (xz plane at y=9.3 km; j=7).

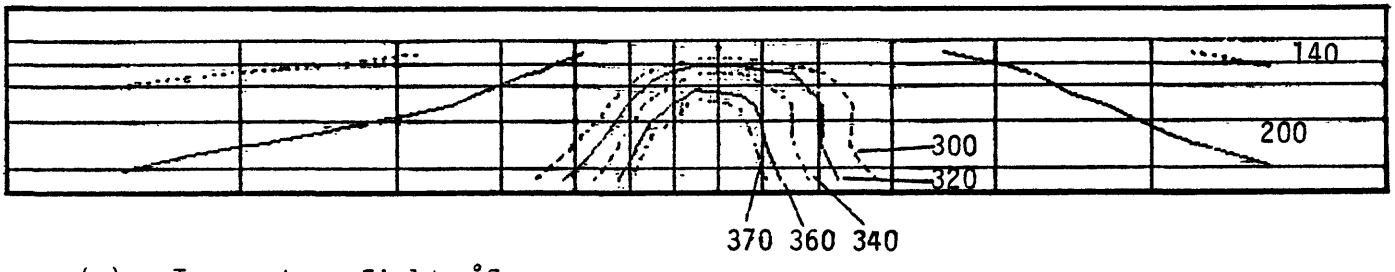

(a) Temperature Field, °F

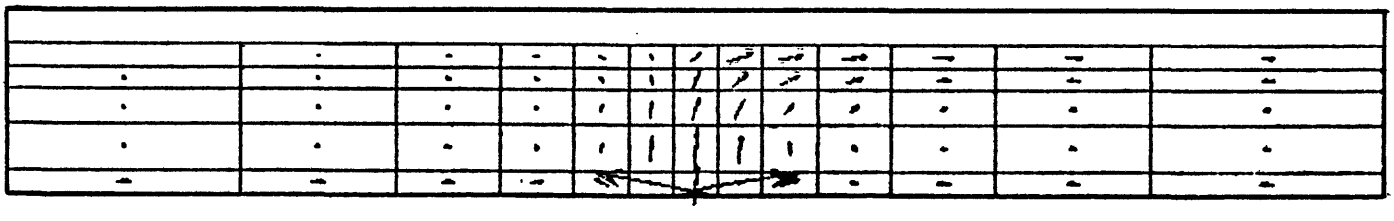

(b) Velocity Field, longest vector corresponds to 9.17×10^{-6} cm/sec.

Figure 44. Vertical section WE through center of calculational grid (yz plane at x=9.3 km; i=7).

Steady-state conditions for case in which lateral variations in ϕ, k_h and T_B are treated with an axisymmetric source (Run EML-403; M_C = 10 kg/sec; T_C = 204°C).

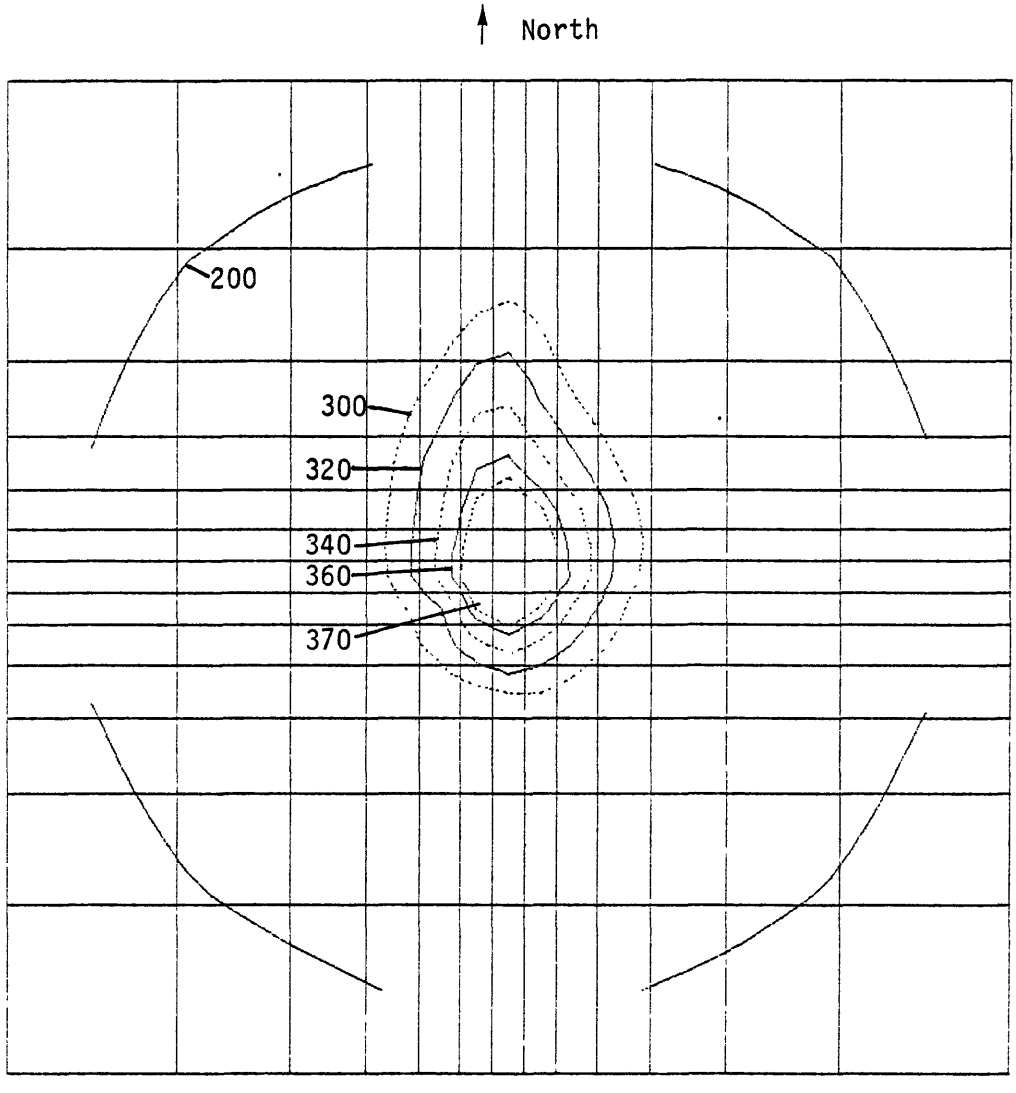

(a) Layer k = 1 (7,000'-8,000'); Temperature Field, °F.

Figure 45. Horizontal sections showing steady-state conditions for case in which lateral variations in ϕ, k_h and T_B are treated with an axisymmetric source (Run EML-403; $\dot{M}_C$ = 10 kg/sec; T_C = 204°C).

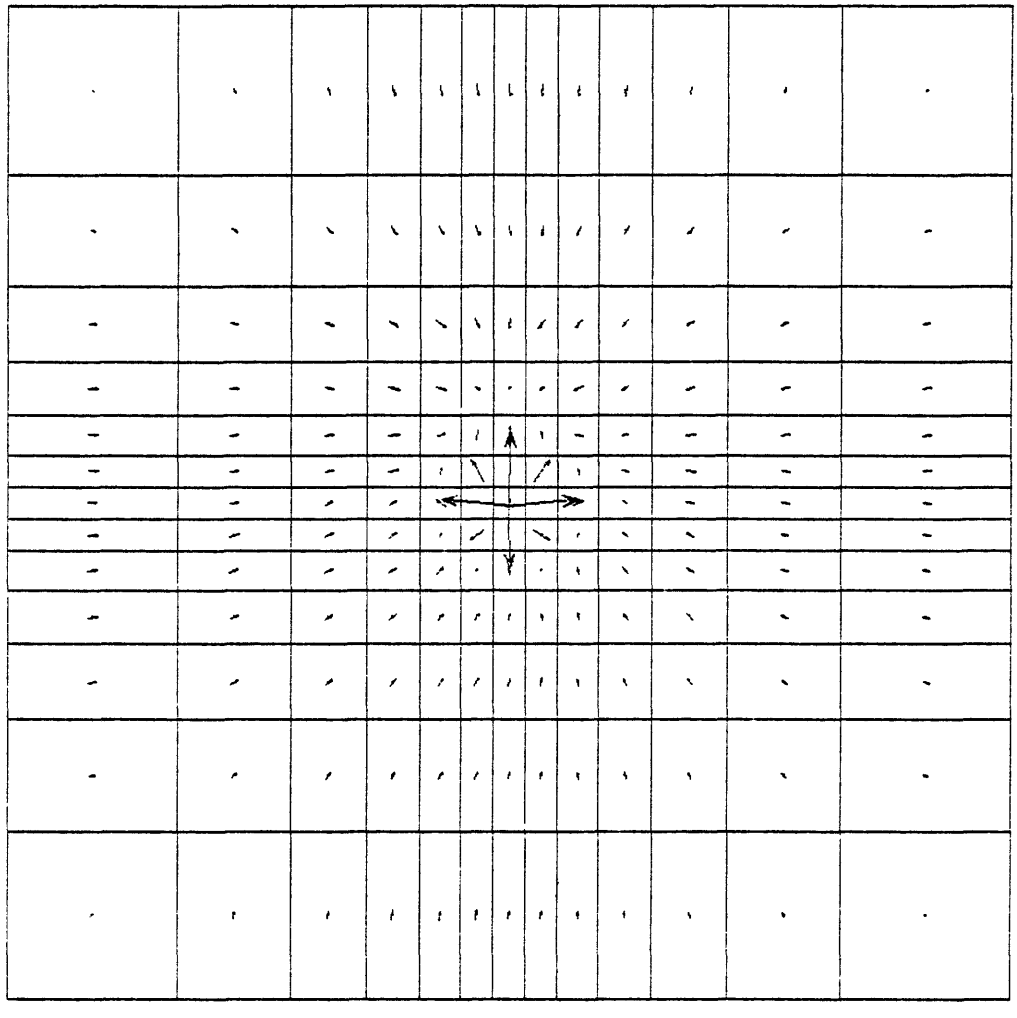

(b) Layer k = 1 (7,000'-8,000'); Velocity Field, longest vector corresponds to 1.03×10^{-5} cm/sec.

Figure 45.

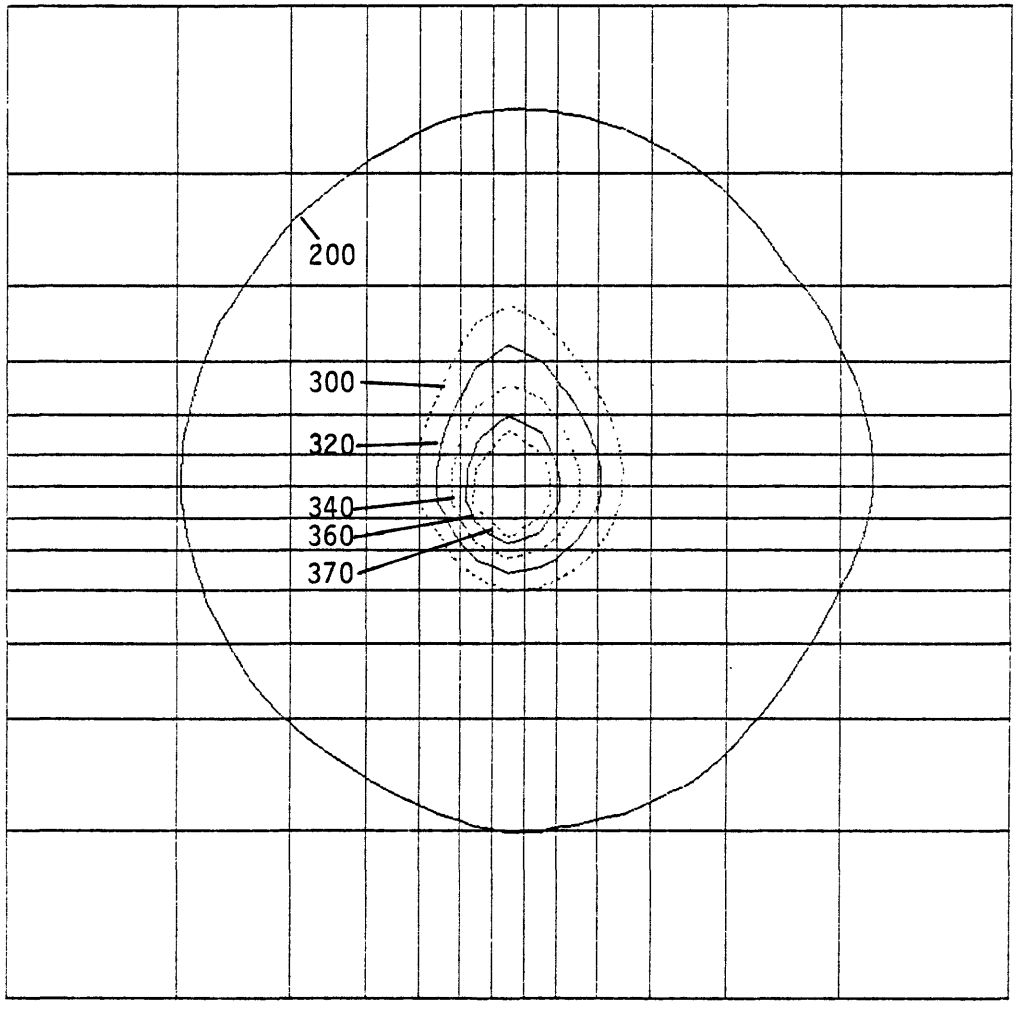

(c) Layer k = 2 (5,000'-7,000'); Temperature Field, °F.

Figure 45.

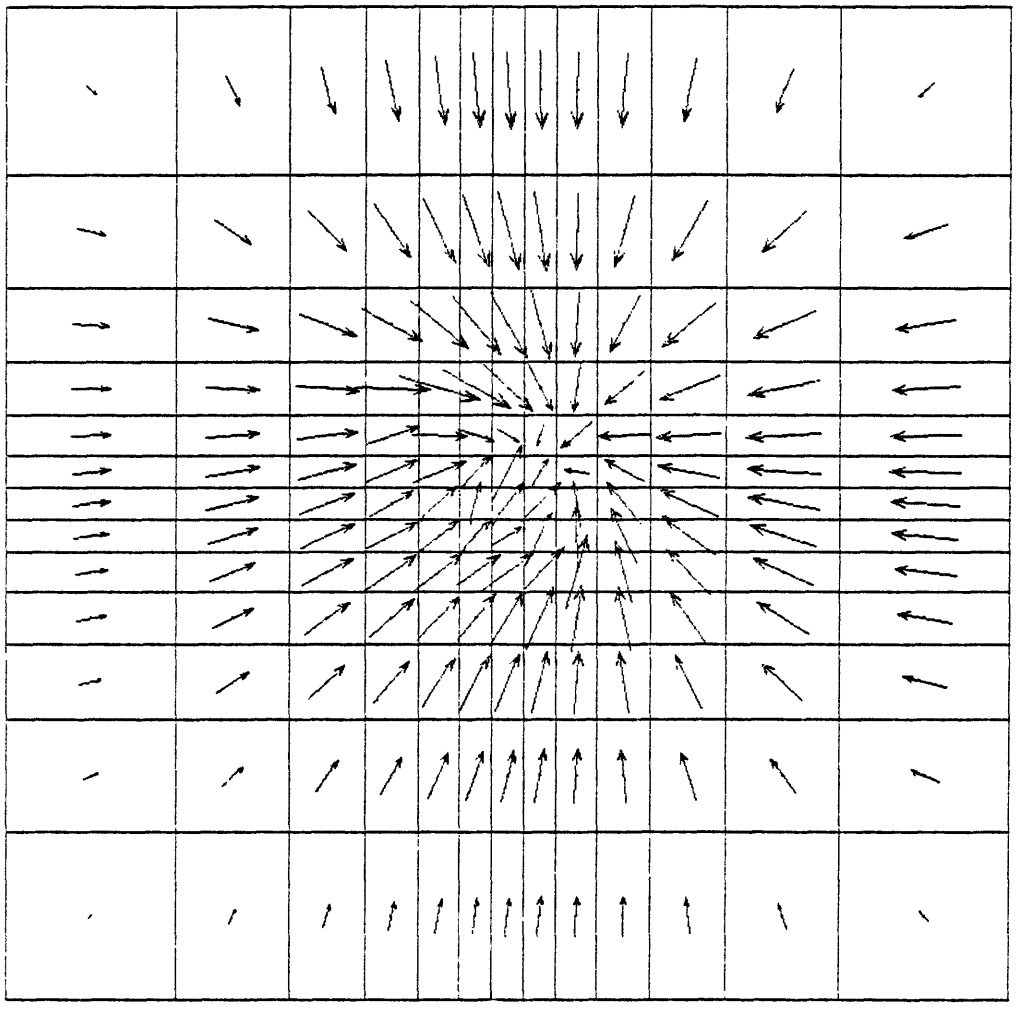

(d) Layer k = 2 (5,000'-7,000'); Velocity Field, longest vector corresponds to 0.58×10^{-6} cm/sec.

Figure 45.

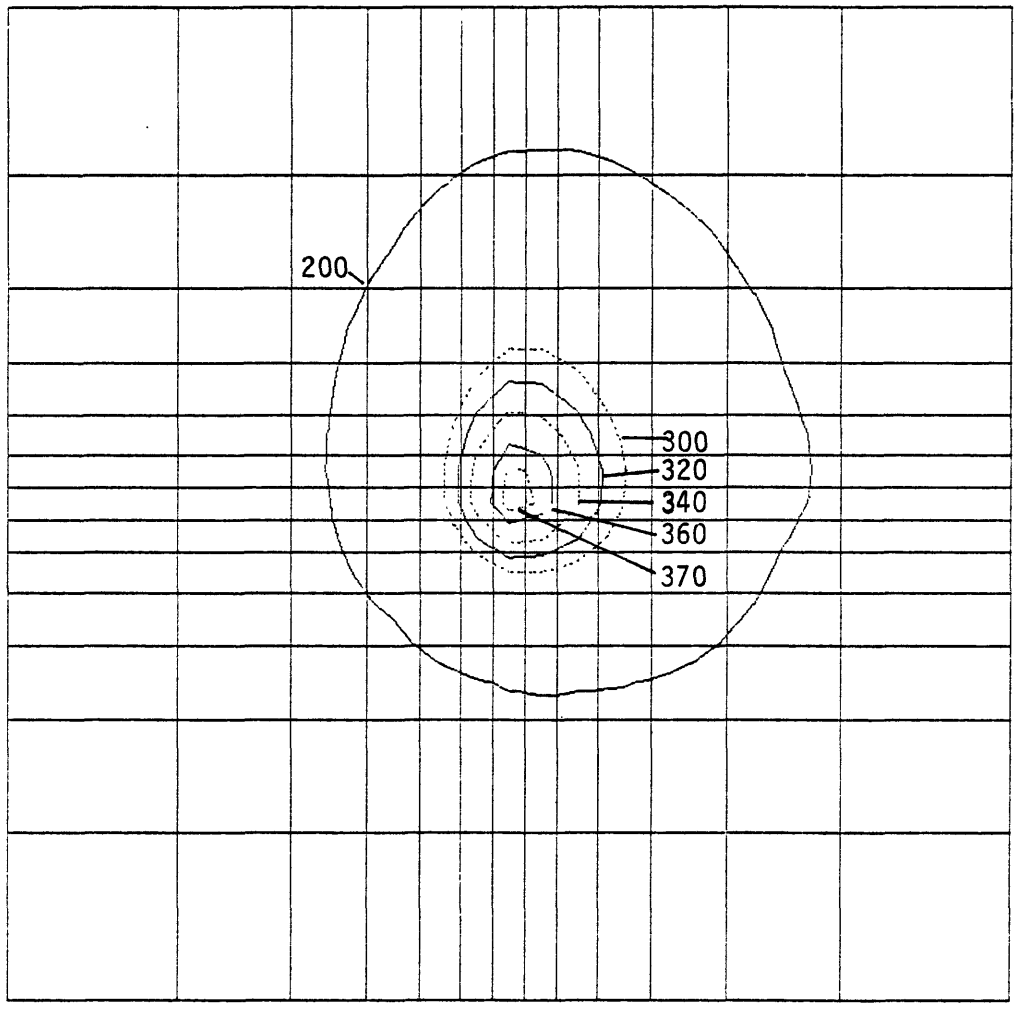

(e) Layer k = 3 (3,500'-5,000'); Temperature Field, °F.
Figure 45.

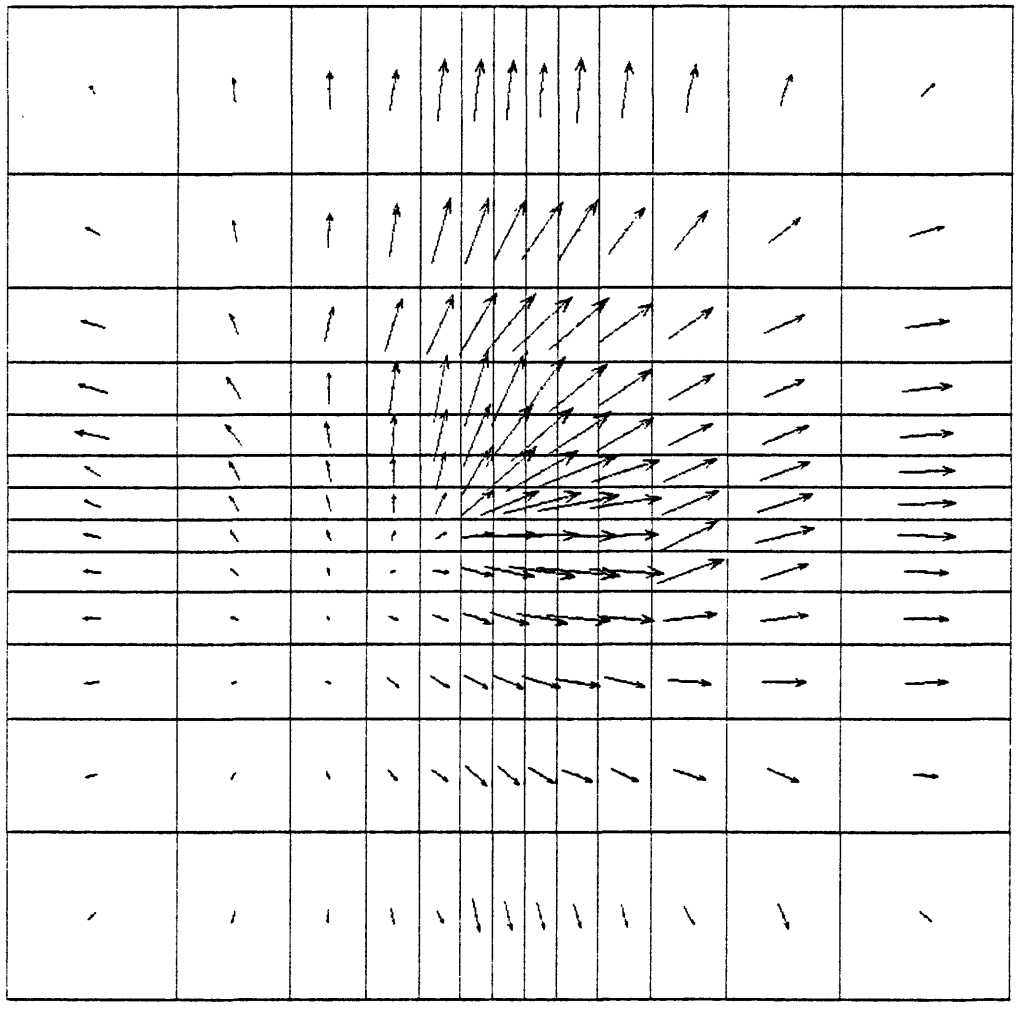

(f) Layer k = 3 (3,500'-5,000'); Velocity Field, longest vector corresponds to 0.72 x 10^{-6} cm/sec.

Figure 45.

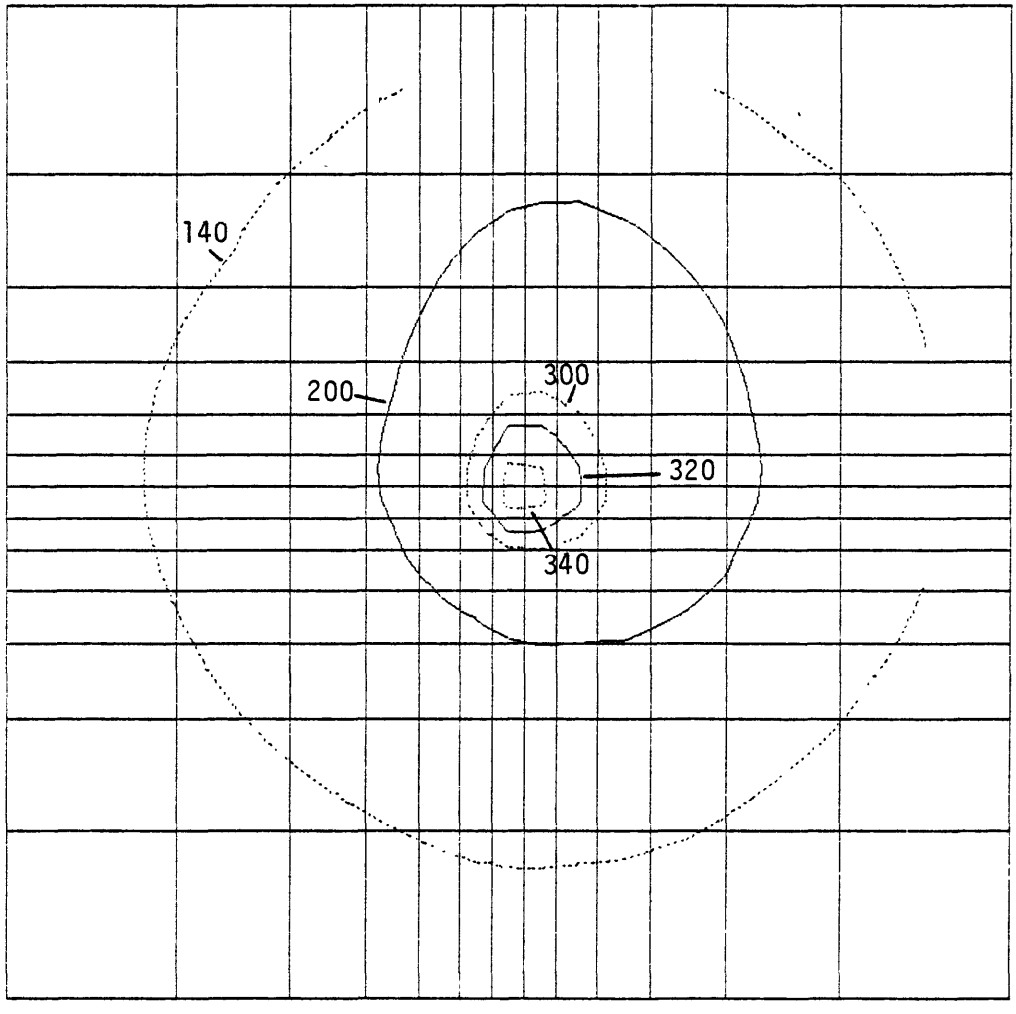

(g) Layer k = 4 (2,500'-3,500'); Temperature Field, °F.

Figure 45.

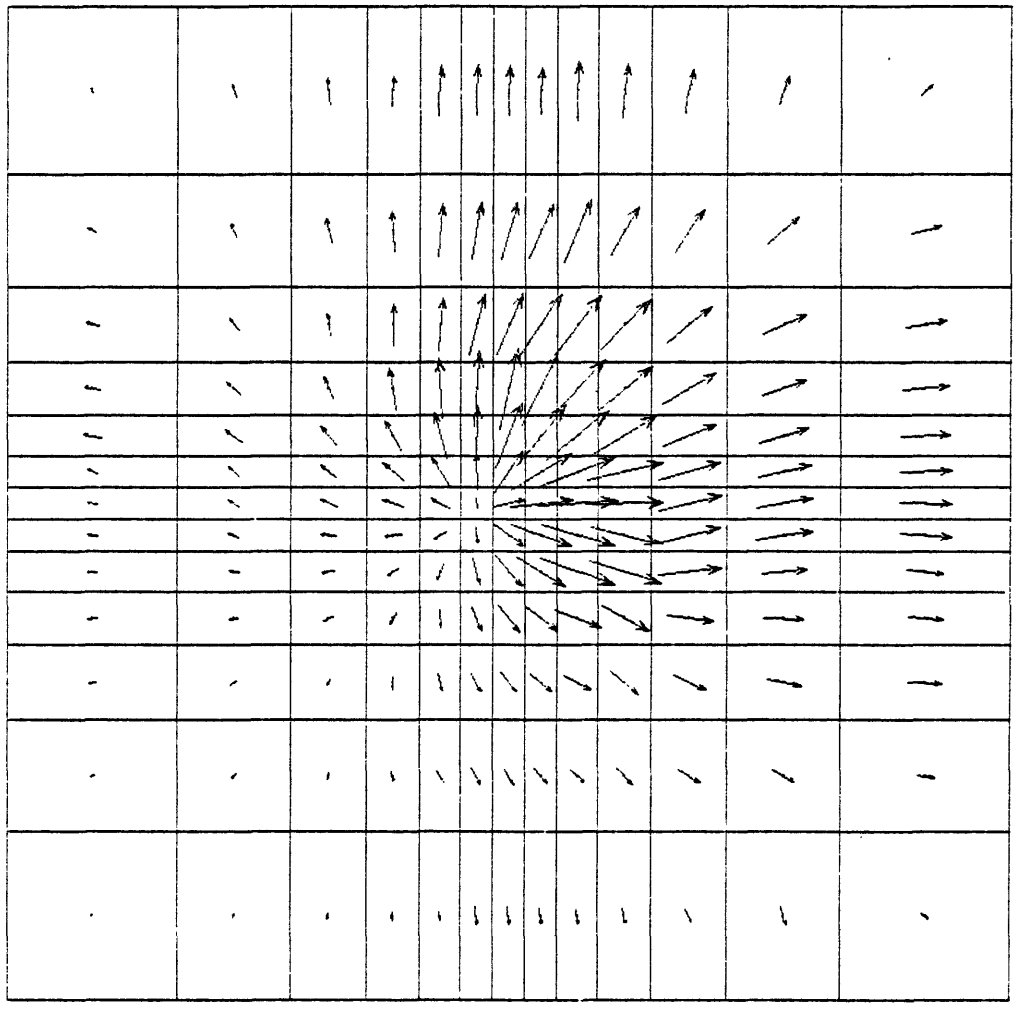

(h) Layer k = 4 (2,500'-3,500'); Velocity Field, longest vector corresponds to 1.38×10^{-6} cm/sec.

Figure 45.

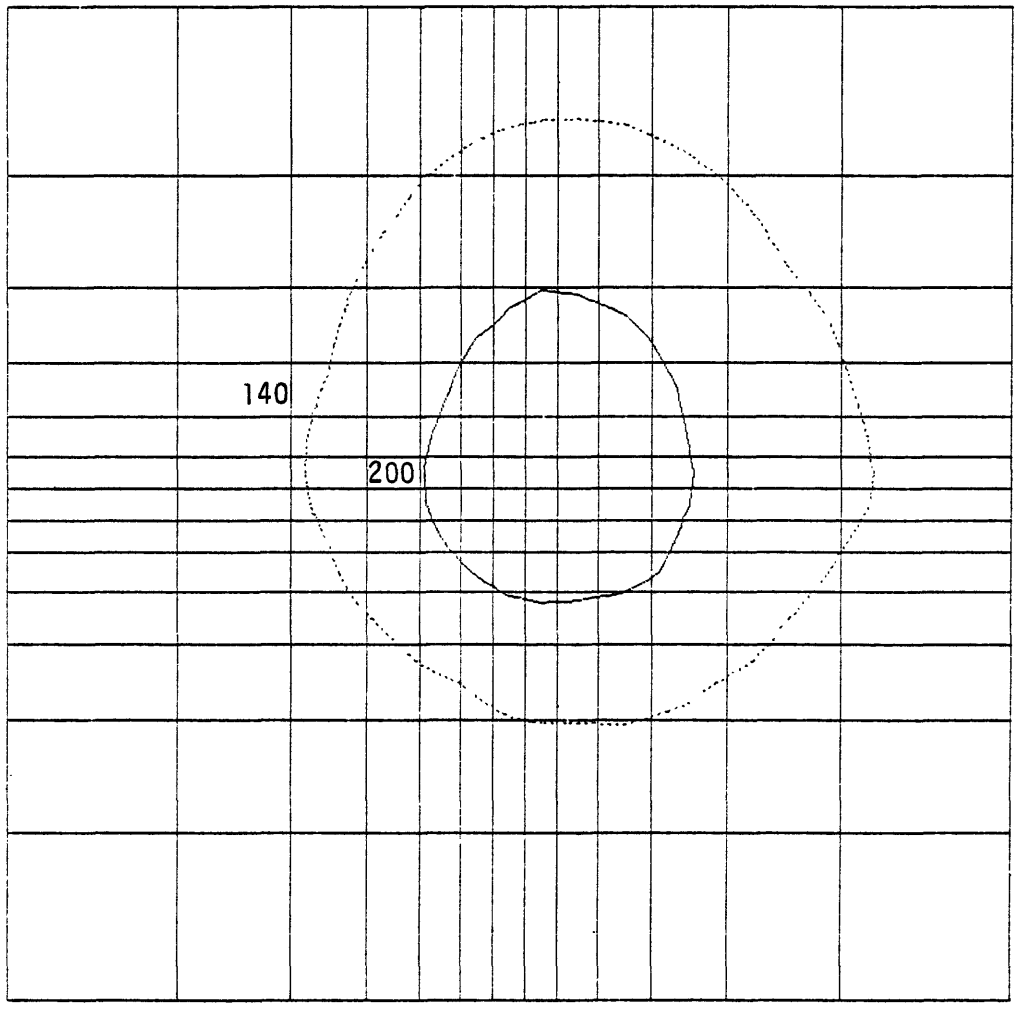

(i) Layer k = 5 (1,500'-2,500'); Temperature Field, °F.

Figure 45.

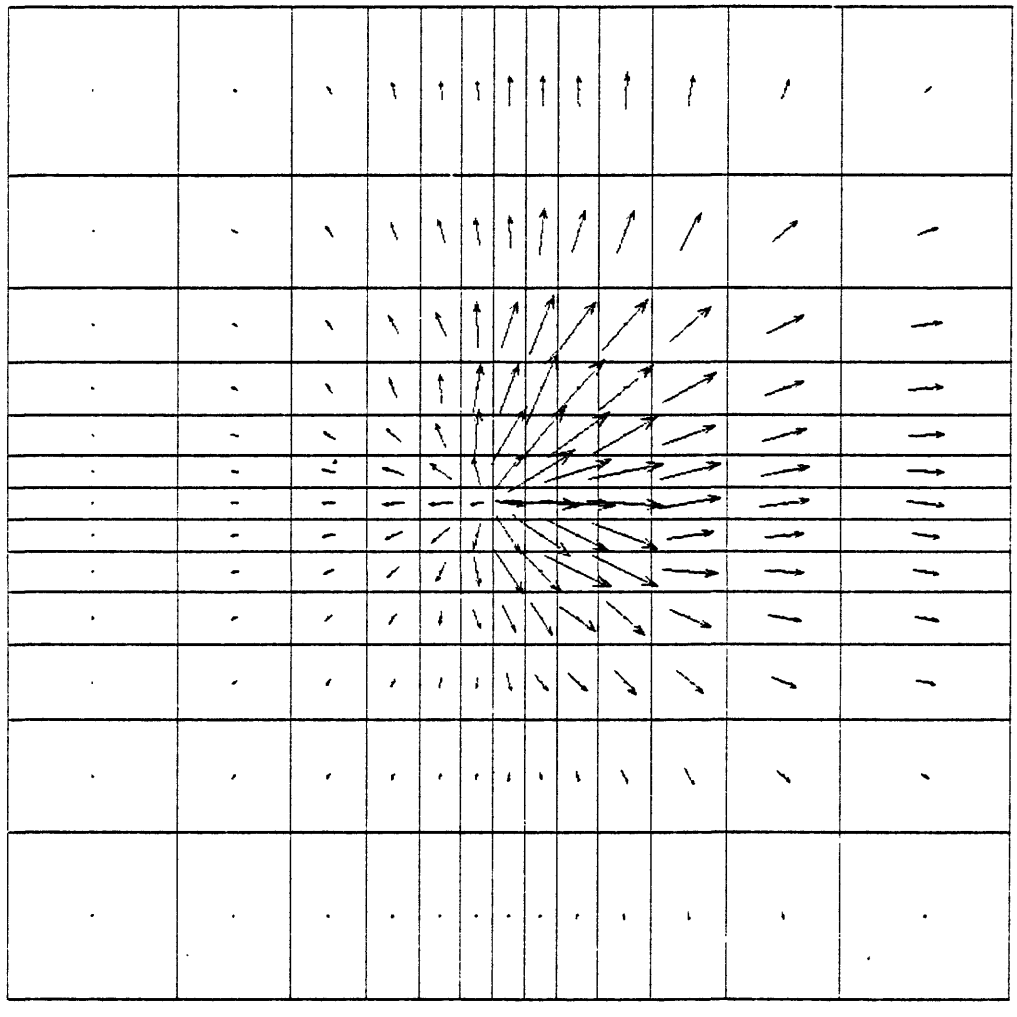

(j) Layer k = 5 (1,500'-2,500'); Velocity Field, longest vector corresponds to 2.08 x 10^{-6} cm/sec.

Figure 45.

fair quantitative agreement with the data extrapolations. The data suggest that the computed temperatures to the north are slightly low. The data extrapolations for the west-east contours are broader than the calculated contours. The fluid velocity plots (Figures 43(b) and 44(b)) indicate that the upwelling fluid flows preferentially to the north and east and the flow of this hot fluid to the northeast along the base of the cap results in the higher surface heat flow calculated in that direction (Figure 41).

Figures 45(a) through (j) depict the temperature and horizontal fluid velocity distributions in each of the five horizontal layers of the computational mesh. At depth, the upwelling convective flow and the influx of cold fluid from the periphery of the system are seen in Figures 45(b) and (d) to be very nearly axisymmetric. As the rising hot fluid nears the base of the geothermal cap, however, the higher horizontal formation permeabilities to the northeast (see Figures 40(c) and (d)) result in preferential movement of the hot fluid in that direction. The lateral (and vertical) variations in the horizontal permeabilities have the same effect as structural dip to the northeast would have on the fluid flow. The calculated temperature contours are in fair agreement with the approximations presented by TRW for corresponding depths (e.g., compare Figure 45(c) with Figure 14). The agreement at great depths is best (due to the imposition of T_B) and the agreement becomes less satisfactory as the surface is approached.

7.2 LATERAL VARIATIONS WITH LEAKY FAULT

The results of LIGHTS Run EML-403 (presented above) suggest that the simple point-source of hot fluid should be replaced by an appropriate spatial distribution that will raise the subsurface temperature and surface heat flow to the north of the hot spot. A number of calculations were made in which the point-source was replaced by a leaky fault radiating northward from the center of the

grid. The exploratory results presented in Subsection 6.3 formed the basis of our selections for the distribution of the convective fluid source that was assumed to enter the reservoir along the fault. The vertical permeability (k_v) in the vicinity of the fault is assumed to vary from 0.5 md near the fault plane to 0.25 md according to the distribution depicted in Figure 33(a).

Three LIGHTS calculations were made in which the only change from Run EML-403 was the replacement of the axisymmetric (point) source with a leaky fault model. The distribution of the convective mass sources along the length of the fault, together with the axisymmetric source, is illustrated in Figure 46. The ramp distribution (Run EML-404) produced a steady-state solution in better agreement with the subsurface temperature and surface heat flow data than the two calculations which employed uniform distributions (Runs 401 and 402). Only the results for Run EML-404 will, therefore, be presented here.

Figures 47 through 50 illustrate the steady-state solution (101,760 years) obtained in Run EML-404. The surface heat flow (Figure 47) predicted by the model exhibits the desired asymmetries and is in reasonably good agreement with the data throughout the area in which there are measurements (compare Figure 47 with Figure 12). Figures 48 and 49 show the surface temperature and fluid velocity distributions along, respectively, south-north (SN) and west-east (WE) sections passing through the center of the computational grid. The SN section includes the fault plane and the calculated subsurface temperatures along this section are in good agreement with the data extrapolations (compare Figure 48(a) with Figure 17). The calculated temperatures on the WE section are also in reasonably good agreement with the data (compare Figures 49(a) with Figure 18). The velocity vector plots along these vertical sections together with those in the horizontal layers (Figure 50) vividly illustrate the movement of the upwelling convective fluid

to the northeast as it nears the base of the geothermal cap. The calculated temperature contours in the horizontal layers are in reasonably good agreement with the approximations presented by TRW for all five depths.

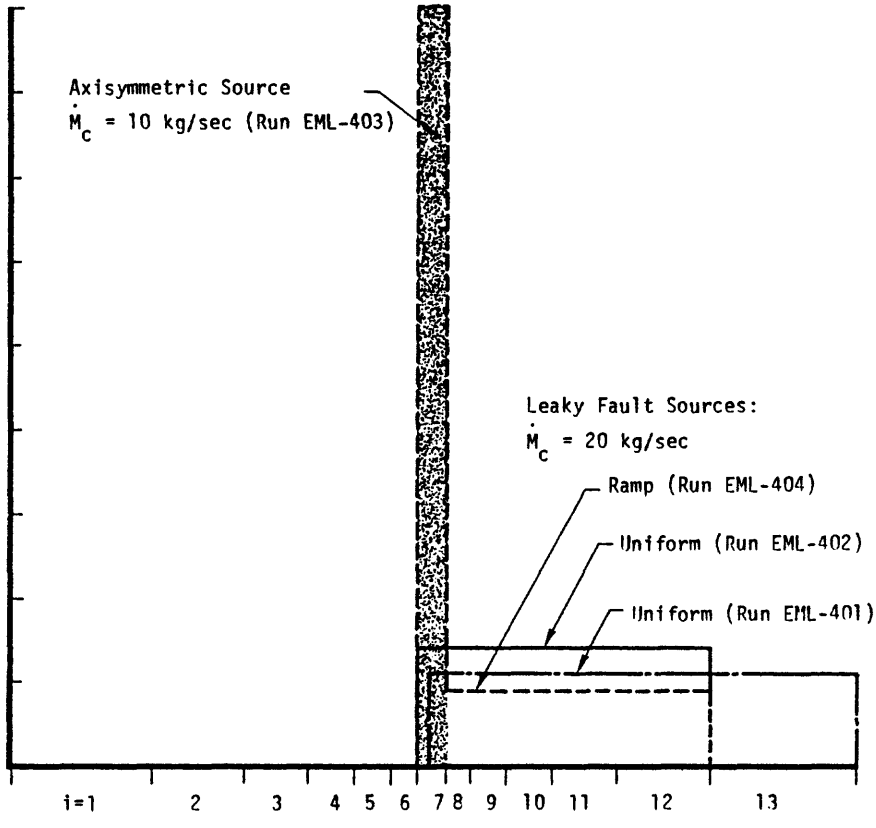

Figure 46. Distribution of convective hot fluid source in fault models used in indicated LIGHTS calculation.

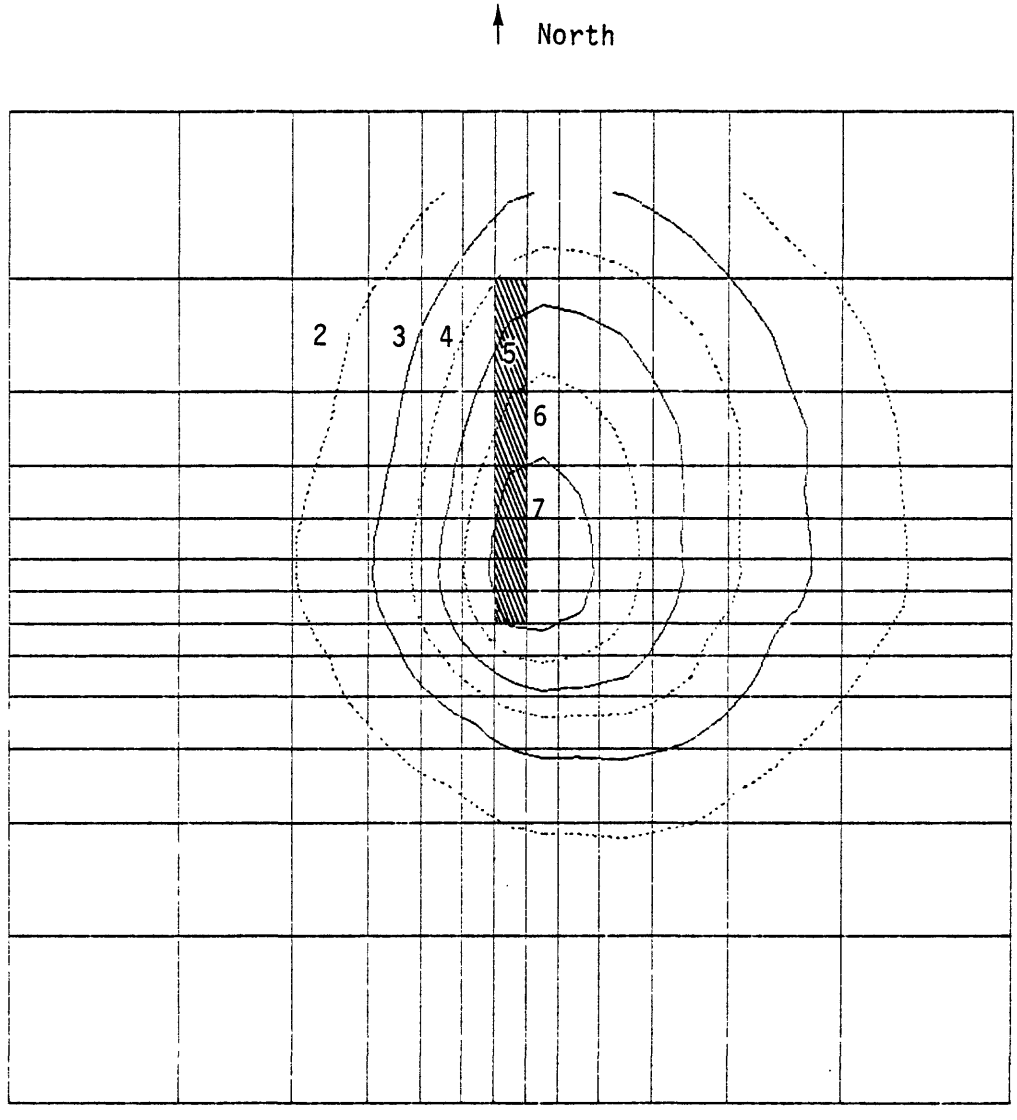

Figure 47. Steady-state surface heat flow (H.F.U.) for case in which lateral variations in ϕ, k_h and T_B are treated in conjunction with a leaky fault to the north with a ramp distributed source (Run EML-404; M_C = 20 kg/sec; T_C = 204°C). Shaded area covered by ramp distribution in Layer 1.

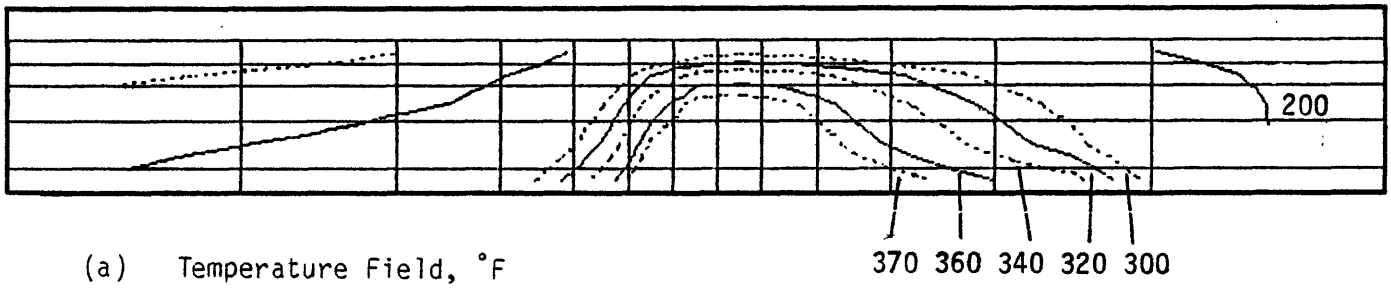

(a) Temperature Field, °F

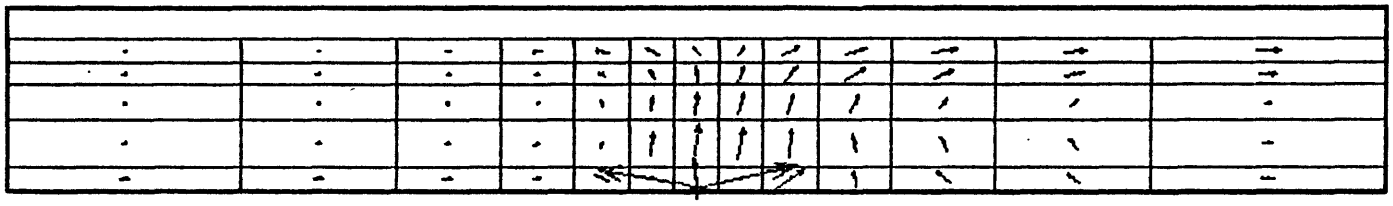

(b) Velocity Field, longest vector corresponds to 9.57×10^{-6} cm/sec.

Figure 48. Vertical section SN which runs south to north through plane of leaky fault (xz plane at y=9.3 km; j=7).

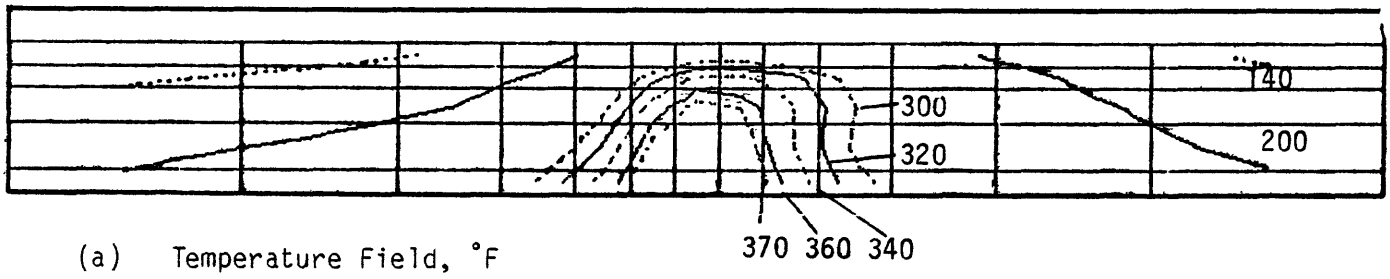

(a) Temperature Field, °F

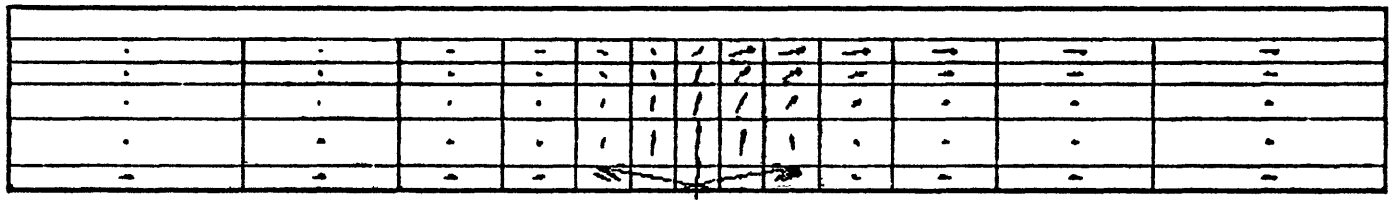

(b) Velocity Field, longest vector corresponds to 9.59×10^{-6} cm/sec.

Figure 49. Vertical section WE which runs west to east through center of calculational grid normal to the plane of the fault (yz plane at x=9.3 km, i=7).

Steady-state conditions for case in which lateral variations in ϕ, k_h and T_B are treated in conjunction with a leaky fault to the north with a ramp distributed source (Run EML-404; M_C = 20 kg/sec; T_C = 204*C).

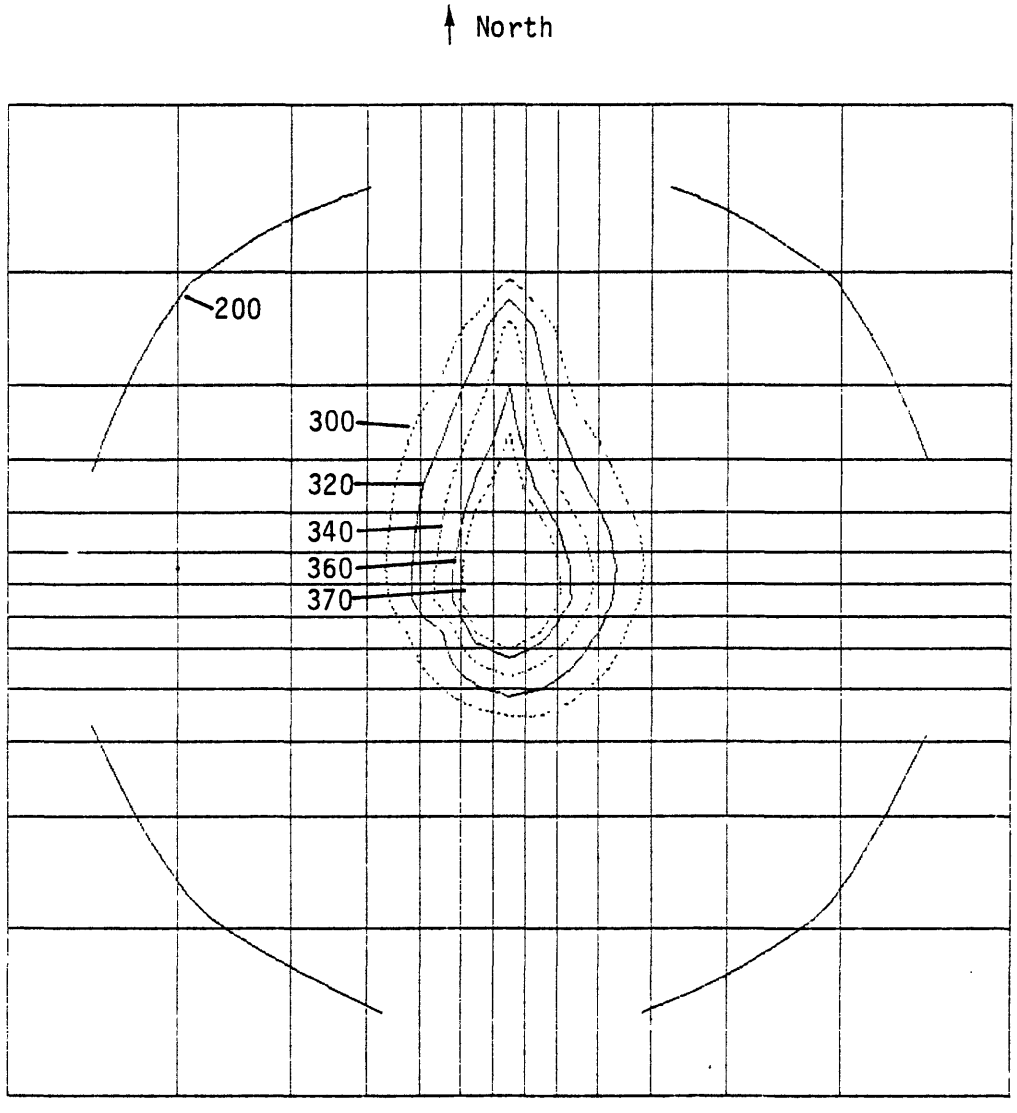

(a) Layer k = 1 (7,000'-8,000'); Temperature Field, °F.

Figure 50. Horizontal sections showing steady-state conditions for case in which lateral variations in ϕ, k_h and T_B are treated in conjunction with a leaky fault to the north with a ramp distribution source (Run EML-404; $\dot{M}_C$ = 20 kg/sec; T_C = 204°C).

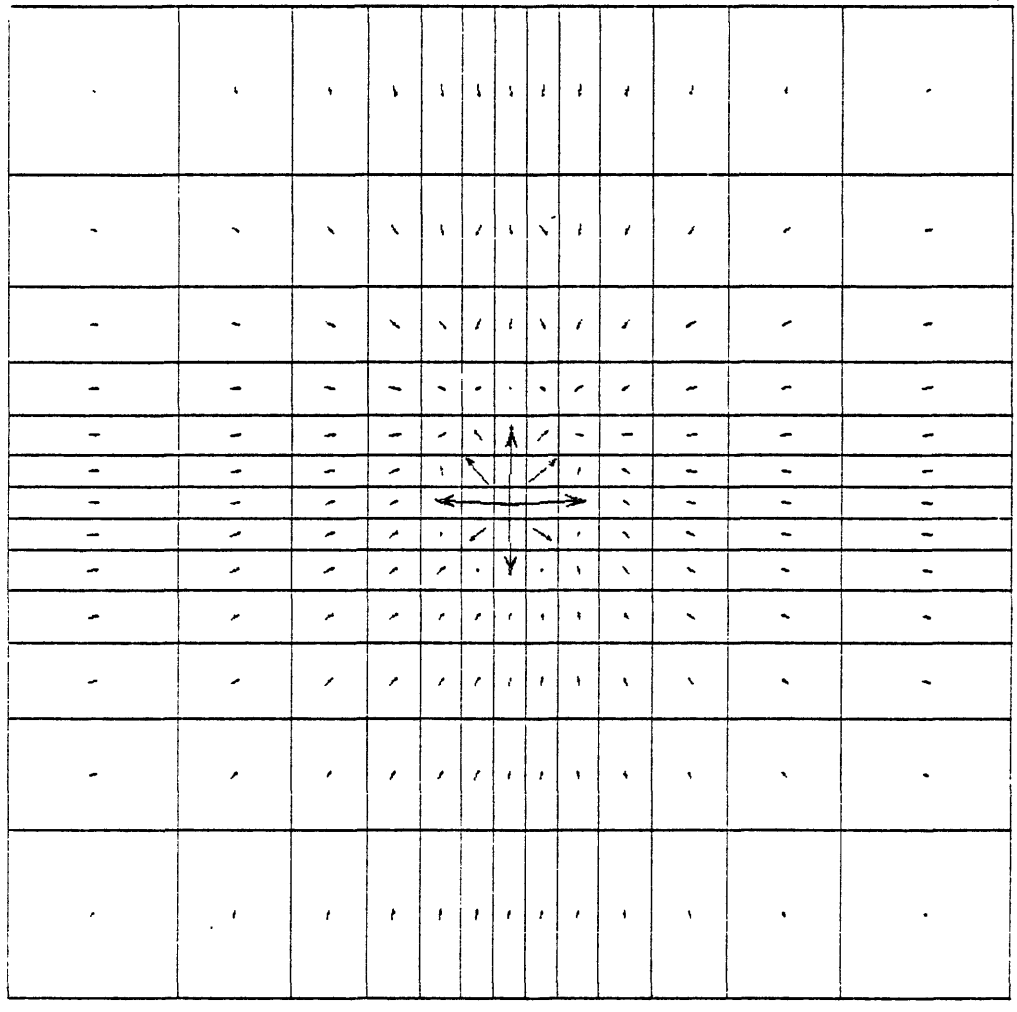

(b) Layer k = 1 (7,000'-8,000'); Velocity Field, longest vector corresponds to 9.45×10^{-6} cm/sec.

Figure 50.

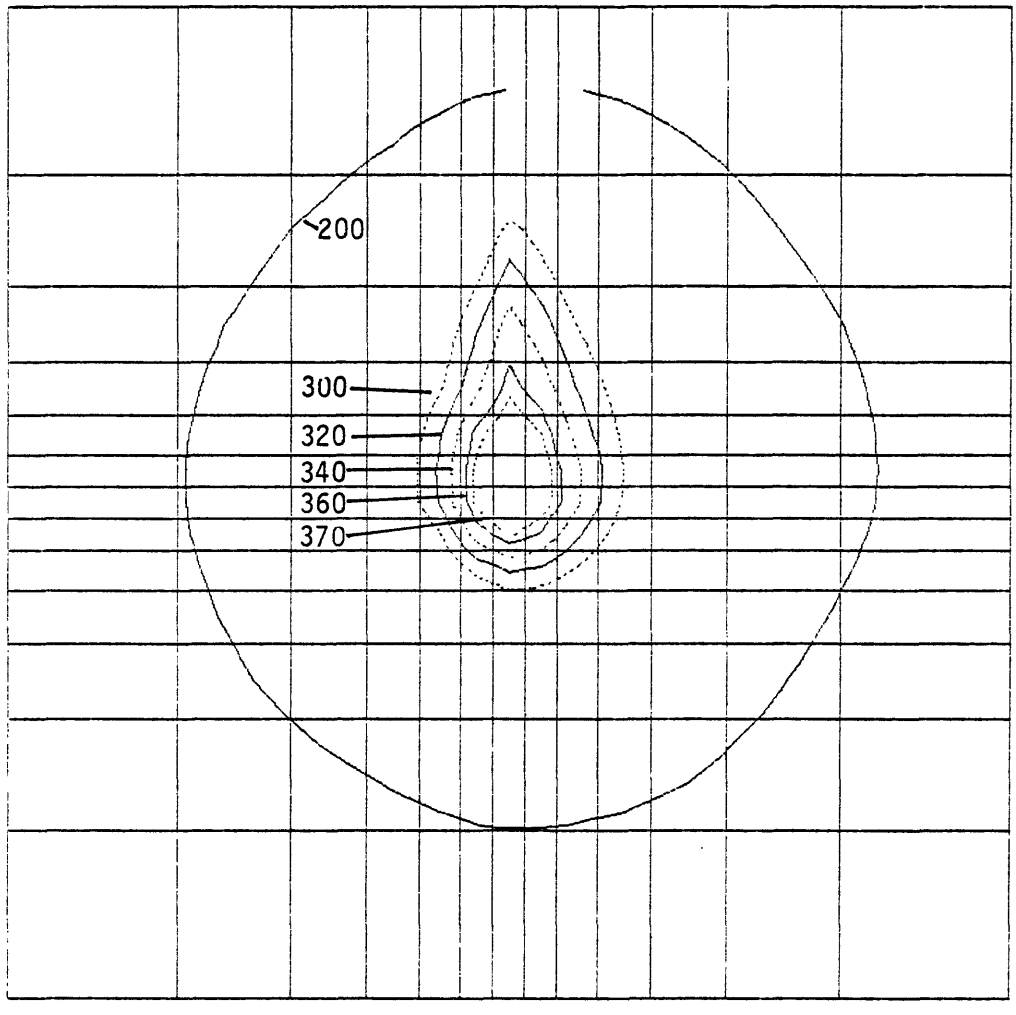

(c) Layer k = 2 (5,000'-7,000'); Temperature Field, °F.
Figure 50.

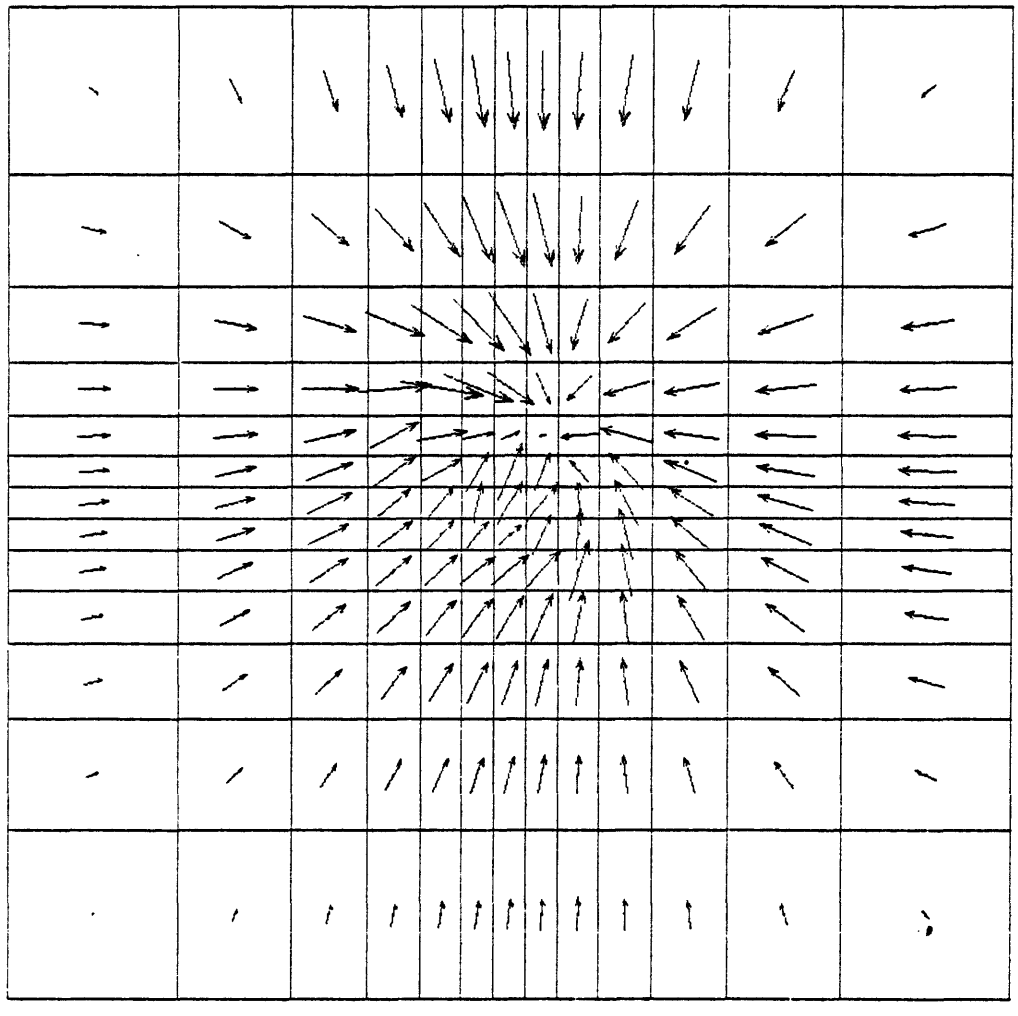

(d) Layer k = 2 (5,000'-7,000'); Velocity Field, longest vector corresponds to 0.85 x 10^{-6} cm/sec.

Figure 50.

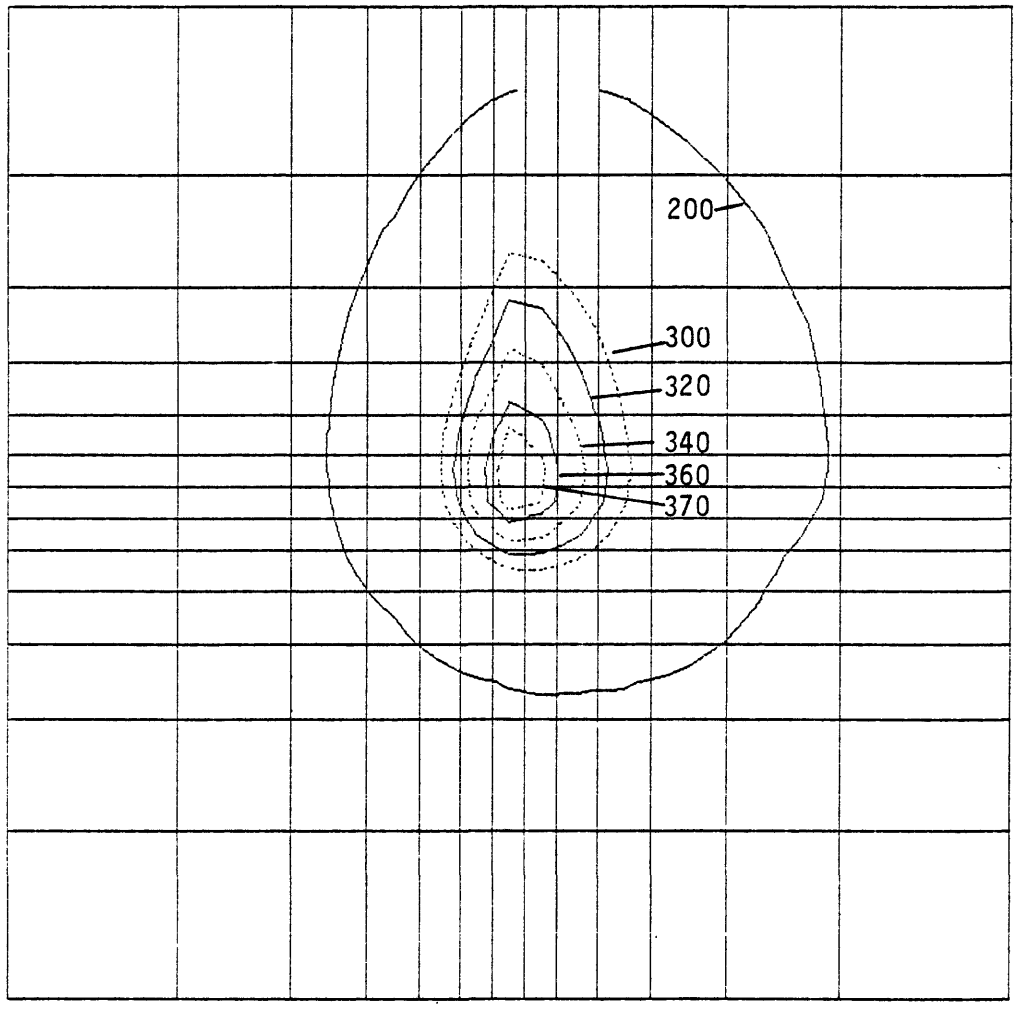

(e) Layer k = 3 (3,500'-5,000'); Temperature Field, °F.
Figure 50.

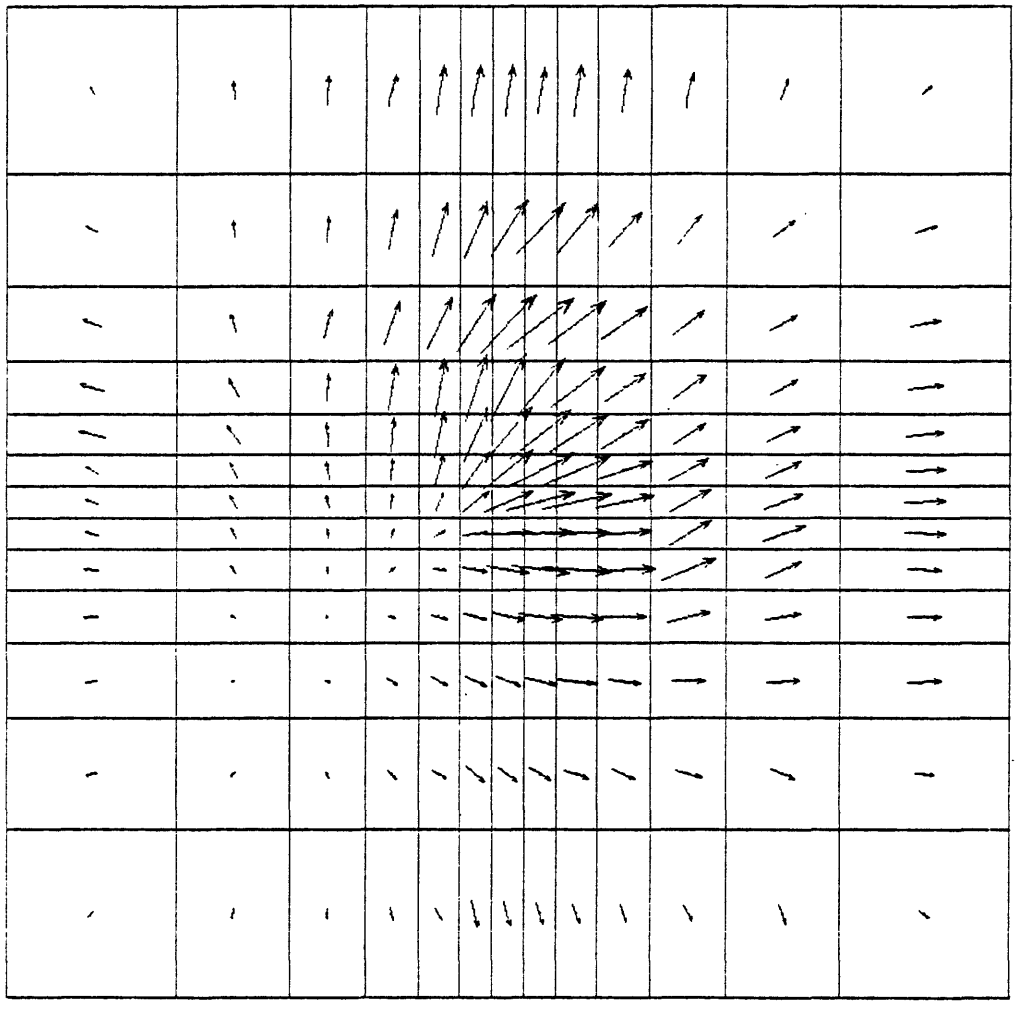

(f) Layer k = 3 (3,500'-5,000'); Velocity Field, longest vector corresponds to 0.86×10^{-6} cm/sec.

Figure 50.

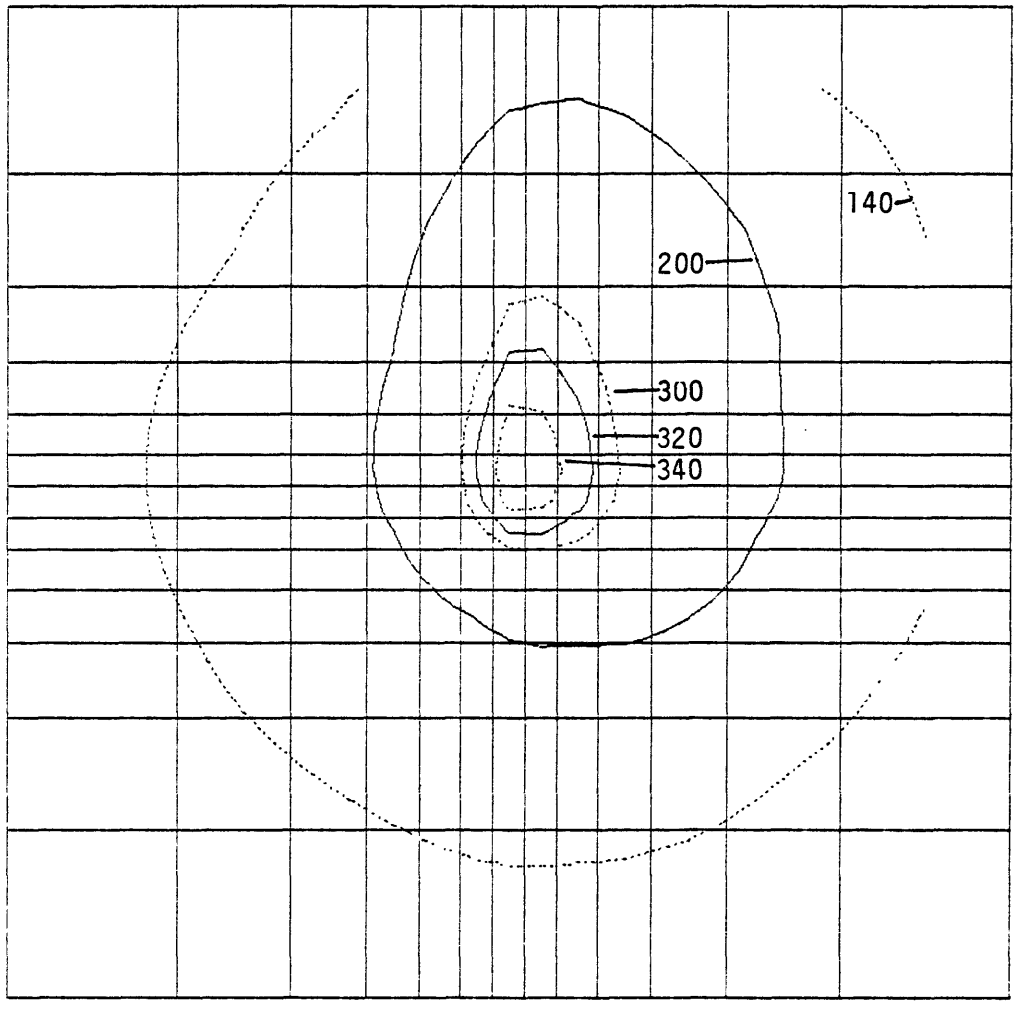

(g) Layer k = 4 (2,500'-3,500'); Temperature Field, °F.
Figure 50.

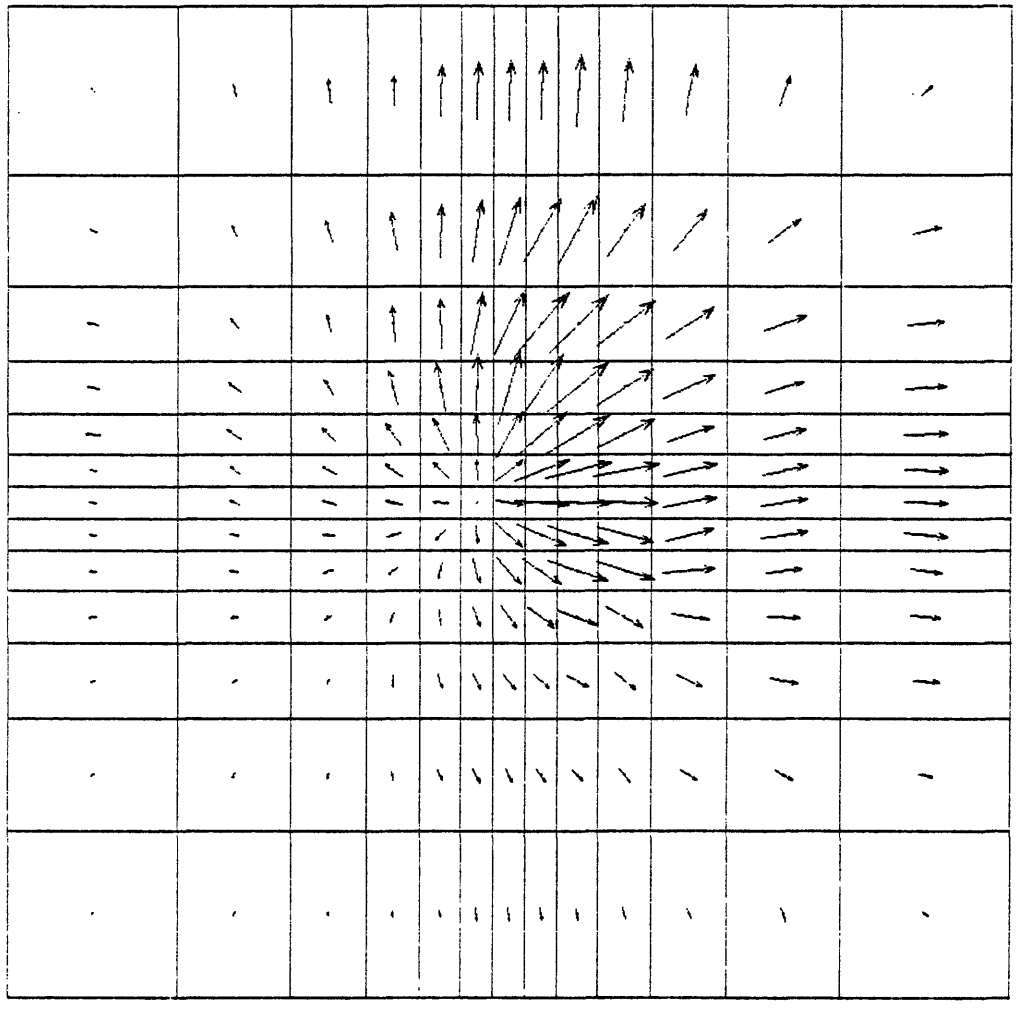

(h) Layer k = 4 (2,500'-3,500'); Velocity Field, longest vector corresponds to 1.90×10^{-6} cm/sec.

Figure 50.

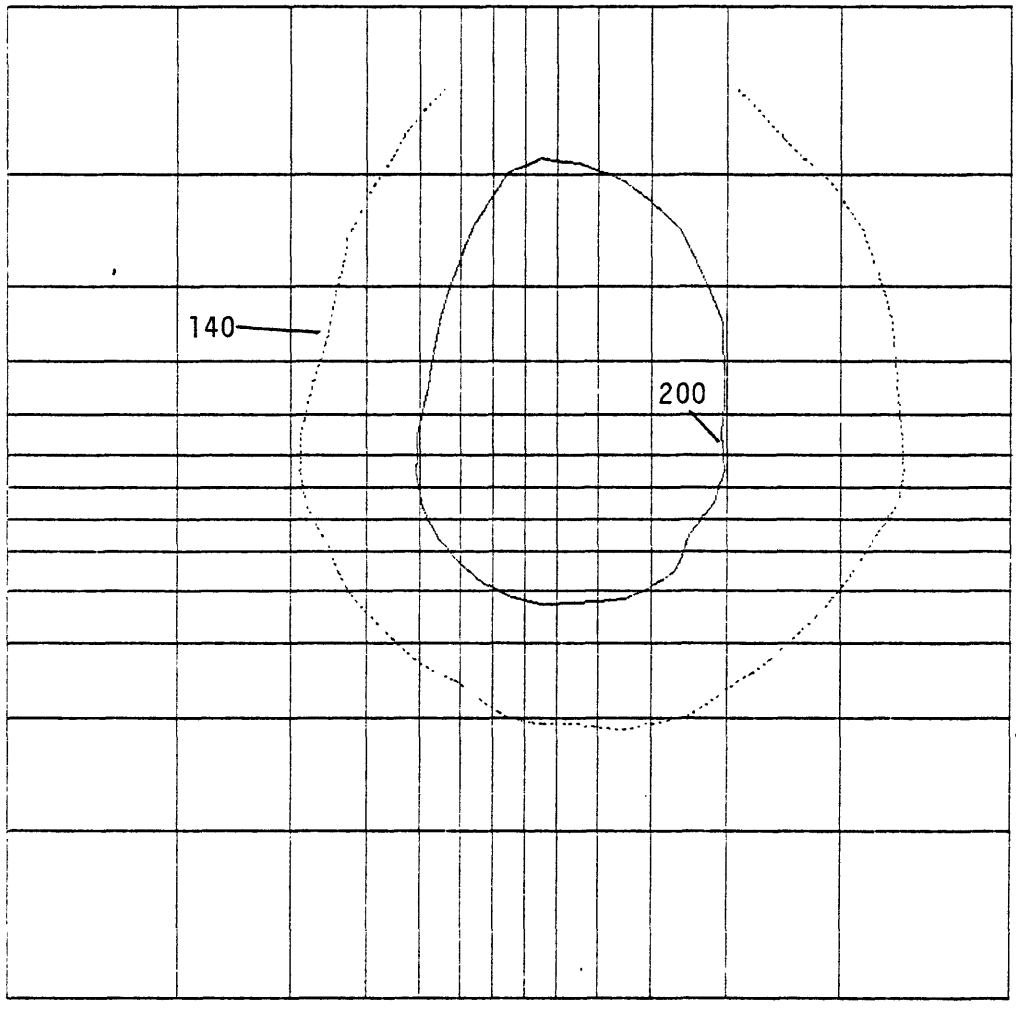

(i) Layer k = 5 (1,500'-2,500'); Temperature Field, °F.
Figure 50.

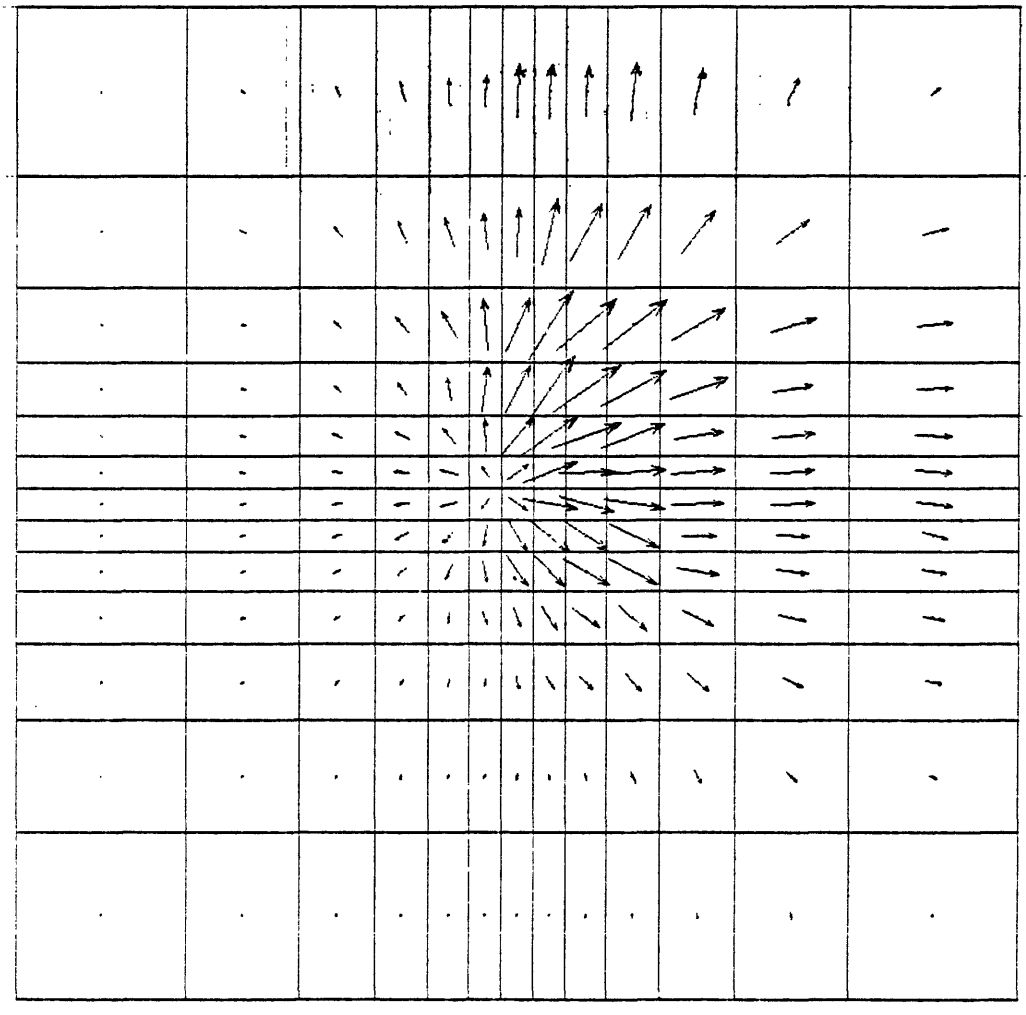

(j) Layer k = 5 (1,500'-2,500'); Velocity Field, longest vector corresponds to 3.19×10^{-6} cm/sec.

Figure 50.

VIII. DISCUSSION AND FUTURE PLANS

The calculations for the various models of the East Mesa hydrothermal system presented in this report show how a reservoir simulator can be used to synthesize a quantitative hydrothermal model that is consistent with known geological, geophysical, thermal, petrophysical and hydrological data. The methodology of evolving a model consistent with a diverse mix of data relies on performing numerical experiments within the framework of an overall conceptual model of the system. These results further demonstrate that the final model thereby developed is likely to be non-unique. In the present case, however, there is sufficient information available that the range of relevant parameters that yield an adequate match to data is reasonably limited.

The subsurface temperature and reservoir properties used in this study are based primarily on data from the first fourteen geothermal wells drilled at East Mesa through 1977. Through 1979, however, some twenty-four geothermal wells had been drilled within the area, including ten by Republic Geothermal, Inc. in the northern portion, five by the U. S. Bureau of Reclamation in the central area, and eight by Magma Power Co. to the south. The newer development wells drilled by Republic and Magma have filled in areas covered by the earlier exploration wells and have apparently yielded similar data. A recent paper (Morris and Campbell [1979]) evaluates the amount of energy that may be recovered from the Republic portion of the East Mesa field by geothermal fluid production. They use a more complete set of well-test data to estimate reservoir formation properties for the northern portion of the East Mesa reservoir; their estimates for that region that are generally in close agreement with those independently developed and used here. The principal difference is in the choice made for the vertical formation permeability (k_v), for which no direct information is available. Based upon our calculations of the natural mass and heat

flow in the system, we believe our conclusion that the effective regional vertical permeability must be quite low to be on firm ground. If the vertical permeability is raised only to a few millidarcies (compared to the 0.25-0.5 md range used here), the entire subsurface temperature distribution is dramatically altered; the isotherms become mushroom-shaped, and temperature-depth profiles show pronounced inversions. Such large-scale inversions have never been observed at East Mesa to our knowledge. As mentioned previously, the University of Colorado researchers (see Kassoy and Zebib [1978]) have neglected vertical permeability altogether in their analytical studies of the reservoir. Of course, the present calculations are regional in scope. It is entirely possible (even likely) that locally the vertical permeability may fluctuate significantly around a regional low average, so that at particular locations within the field the vertical permeability may be substantially in excess of 0.5 md.

Although we have collected the available data for the project study area, we have at this time completed the model development only for the smaller region containing the geothermal reservoir shown in Figure 6. This is the heart of the hydrothermal system, however, and consequently the extension of the model (as represented by Run EML-404) to the full project study area should be relatively straightforward. Once this is accomplished, the procedures described in our conceptual model (Section II) can be applied to assess the effect on the integrated hydrothermal system to large scale flow of geothermal fluid. We propose to complete this aspect of the work in a future project.

REFERENCES

Bailey, T. P. [1977], "A Hydrogeological and Subsurface Study of Imperial Valley Geothermal Anomalies, Imperial Valley, California," Geological Sciences, University of Colorado Report.

Black, H. T. [1975], "A Subsurface Study of the Mesa Geothermal Anomaly, Imperial Valley, California," Geological Sciences, University of Colorado Report.

Combs, J. and D. Hadley [1977], "Microearthquake Investigation of the Mesa Geothermal Anomaly, Imperial Valley, California," Geophysics, Vol. 42, No. 1, pp. 17-33.

Dutcher, L. C., W. F. Hardt and W. R. Moyle, Jr. [1972] "Preliminary Appaisal of Ground Water in Storage with Reference to Geothermal Resources in the Imperial Valley Area, California," U. S. Geological Survey Circular 649, 57 p.

Elders, W. A., R. W. Rex, T. Meidev, P. T. Robinson and S. Biehler [1972], "Crustal Spreading in Southern California," Science, Vol. 178, No. 4056, pp. 15-24.

Garg, S. K., J. W. Pritchett, M. H. Rice, and T. D. Riney [1977],"U.S. Gulf Coast Geopressured Geothermal Reservoir Simulation," Systems, Science and Software Report SSS-R-77-3147, February.

Goyal, K. P. [1978], "Heat and Mass Transfer in a Saturated Porous Medium with Application to Geothermal Reservoir," Ph. D. Thesis, Department of Mechanical Engineering, University of Colorado.

Hardt, W. F. and J. J. French [1976], "Selected Data on Water Wells, Geothermal Wells and Oil Tests in Imperial Valley, California," U. S. Geological Survey Open-File Report [no number], 251 p.

Hoagland, J. R. and W. A. Elders [1977], "The Evolution of the East Mesa Hydrothermal System, California, U.S.A.," Proceedings, Second International Symposium on Water-Rock Interaction, Vol. III, pp. 127-136.

Howard, J., J. A. Apps, S. Benson, N. E. Goldstein, A. N. Graf, J. Haney, D. Jackson, S. Juprasert, E. Major, D. McEdwards, T. V. McEvilly, T. N. Narashirnhan, B. Schechter, R. Schroeder, R. Taylor, P. van de Kamp and T. Wolery [1978], "Geothermal Resource and Reservoir Investigations of U. S. Bureau of Reclamation Leaseholds at East Mesa, Imperial Valley, California," Lawrence Berkeley Laboratory Report LBL-7094, October.

Kassoy, D. R. and A. Zebib [1978], "Convection Fluid Dynamics in a Model of a Fault Zone in the Earth's Crust," Journal of Fluid Mechanics, Vol. 88, pp. 769-792.

Loeltz, O. J., B. Irelan, J. H. Robinson and F. H. Olmsted [1975], "Geohydrologic Reconnaissance of the Imperial Valley, California," U. S. Geological Survey Professional Paper 486-K, 54 p.

Miller, R. E. [1977], "A Galerkin, Finite-Element Analysis of Steady-State Flow and Heat Transport in Shallow Hydrothermal System in the East Mesa Area, Imperial Valley, California," Journal Research, U. S. Geological Survey Vol. 5, No. 4, pp. 497-508.

Morris, C. W. and D. A. Campbell [1979], "Geothermal Reservoi Energy Recovery: A Three-Dimensional Simulation Study of the East Mesa Field," SPE Paper 8229, presented at annual meeting of Society of Petroleum Engineers, Las Vegas, Nevada, September.

Narasimhan, T. N., R. C. Schroeder, C. B. Goranson and S. M. Benson [1977], "Results of Reservoir Engineering Tests, 1977, East Mesa, California," Paper No. 7482, SPE, AIME, Houston, Texas, October 1-3.

Pearson, R. O. [1976], "Planning and Design of Additional East Mesa Geothermal Test Facilities (Phase IB)," Vol. 1 of TRW Final Report of Work Performed Under ERDA Contract No. E(04-3)-1140, October.

Pritchett, J. W. [1979], "The LIGHTS Code: A Three-Dimensional Single-Phase Liquid Boussinesq Geothermal Reservoir Simulator," Systems, Science and Software Proprietary Internal Document.

Ramey, H. J., W. E. Brigham, H. K. Chen, P. G. Atkinson and H. Arihara [1974], "Thermodynamic and Hydrodynamic Properties of Hydrothermal Systems," Stanford Geothermal Program Report SGP-TR6.

Rex, Robert W., E. A. Babcock, S. Bishler, J. Combs, T. B. Coplen, W. A. Elders, R. B. Furgerson, Z. Garfunkel, T. Meider and P. T. Robinson [1971], "Cooperative Geological Geophysical - Geochemical Investigations of Geothermal Resources in the Imperial Valley area of California," University of California Riverside Report, July.

Riney, T. D., J. W. Pritchett, L. F. Rice and S. K. Garg [1979], "A Preliminary Model of the East Mesa Hydrothermal System," Proceedings Fifth Stanford Geothermal Resrvoir Engineering Workshop, Stanford Report No. SGP-TR-40, pp. 211-214, December 12-14.

TRW Staff [1976], "Study of the Geothermal Reservoir Underlying the East Mesa Area, Imperial Valley, California," Final Report for U. S. Department of Interior, Contract No. 28859-6001-RU-00, December.

U.S. Bureau of Reclamation [1974], "Geothermal Resource Investigations, East Mesa Test Site, Imperial Valley, California,: Status Report, November.

U.S. Bureau of Reclamation [1973], "Geothermal Resource Investigations, Test Well Mesa 6-1, Imperial Valley, California," Special Report, February.

Urban, T. C., W. H. Diment and M. Nathenson [1978], "East Mesa Geothermal Anomaly, Imperial County, California: Significance of Temperatures in a Deep Drill Hole Near Thermal Equilibrium," Geothermal Resources Council, Transactions, Vol. 2, pp. 667-670, July.

White, D. E. [1968], "Environments of Generation of Some Base-Metal Ore Deposits," Economic Geology, Vol. 63, No. 4, pp. 301-335.

Witherspoon, P. A. , T. N. Narasimhana and D. G. McEdwards [1978], "Results of Interference Tests from Two Geothermal Reservoirs," Journal Petroleum Technology, Vol. 30, pp. 10-16.